

Improving Uncertainty Estimation in Geophysical Inversion Modelling

A dissertation presented
by
Sebastian Schnaidt

In fulfilment of the requirements
for the degree of
Doctor of Philosophy
in the subject of
Geophysics



**THE UNIVERSITY
of ADELAIDE**

Submitted to the
Department of Earth Sciences,
School of Physical Sciences, Faculty of Sciences

Adelaide, May 2015



THE UNIVERSITY
of ADELAIDE

© 2015
Sebastian Schnaidt
All Rights Reserved



I can live with doubt, and uncertainty, and not knowing. I think it's much more interesting to live not knowing than to have answers which might be wrong. I have approximate answers, and possible beliefs, and different degrees of certainty about different things, but I'm not absolutely sure of anything.

– Richard P. Feynman

CONTENTS

List of Tables	ix
List of Figures	xi
Abstract	xvii
Statement of Originality	xix
Acknowledgements	xxi
1 Introduction	1
1.1 Aims and Objectives	1
1.2 Introductory Background and Literature Review	2
1.2.1 Direct search methods	3
1.2.2 Joint inversion	5
1.3 Model Errors and Uncertainty	6
1.3.1 Data noise and solution non-uniqueness	6
1.3.2 User introduced model errors	8
1.4 Overview	9

2 Bootstrap Resampling as a Tool for Uncertainty Analysis in 2-D Magnetotelluric Inversion Modelling	13
Summary	15
2.1 Introduction	16
2.2 Method	20
2.2.1 Bootstrap resampling	20
2.2.2 Occam's inversion	24
2.3 Ensemble Appraisal	25
2.3.1 Variability in absolute value	25
2.3.2 Variability in cell gradient	26
2.4 Results	28
2.4.1 Synthetic test case	28
2.4.2 Delamerian MT Transect	35
2.5 Discussion	42
2.6 Conclusion	46
Acknowledgments	47
3 A Novel Approach to Pareto-optimal Joint Inversion Modelling and Data Set Compatibility Analysis of Geophysical Data	49
Summary	51
3.1 Introduction	52
3.2 Theory	54
3.2.1 Definition of multi-dimensional Pareto-optimality . .	54
3.2.2 The Multi-objective Joint Optimisation Algorithm .	55
3.2.3 Solution ensemble appraisal	61

3.2.4	Data set compatibility	62
3.3	Feasibility Study: Example Data	65
3.3.1	Data set properties	66
3.3.2	Resulting model distribution	68
3.4	Feasibility Study: Analysis	69
3.4.1	Two objectives - compatible data sets	70
3.4.2	Two objectives - incompatible data sets	78
3.4.3	Multiple objectives	82
3.4.4	Influence of the numbers of objectives on the stability of the compatibility measure	86
3.5	Discussion	88
3.6	Conclusion	93
	Acknowledgments	94
4	Parameter Studies of Geophysical Joint Inversion Modelling - Using Multi-objective Optimisation	95
	Summary	97
4.1	Introduction	98
4.2	Parameter Analysis	100
4.2.1	Redefinition of the misfit δ	100
4.2.2	The box size parameter ϵ	100
4.2.3	Model distribution analysis	107
4.3	Application to Real Data	110
4.3.1	Cooper Basin, South Australia	111
4.3.2	Isa Extension MT survey	119
4.4	Discussion	124

CONTENTS

4.4.1	Case studies	126
4.5	Conclusion	128
	Acknowledgments	128
5	Summary and Conclusion	129
5.1	Bootstrap Resampling	129
5.2	Multi-objective Joint Optimisation	131
5.3	Concluding Comments	133
A	Appendix	137
A.1	Supporting Material for Chapter 4	137
A.1.1	Figures	137
A.1.2	Tables	139
	Bibliography	141

LIST OF TABLES

3.1	Analysis of the deviation from the ideal line and median distance from the ideal point (1,1) for the noise-free compatible 2-objective case.	73
3.2	Analysis of the deviation from the ideal line and median distance from the ideal point (1,1) for the compatible 2-objective case (with 3 % noise).	75
3.3	Analysis of the deviation from the ideal line and median distance from the ideal point (1,1) for the 5/5-case and the 10/5-case.	77
3.4	Analysis of the deviation from the ideal line and median distance from the ideal point (1,1) for the noise-free incompatible 2-objective case	80
3.5	Analysis of the deviation from the ideal line and median distance from the ideal point (1,1) for the incompatible data 2-objective case with 3 % white noise on the data.	82
3.6	Analysis of the deviation from the ideal line and median distance from the ideal point (1,1,1) for the multi-objective case inversion runs.	84
3.7	Analysis of the deviation from the ideal line and median distance from the ideal point (1,1) for the 2-objective case without regularisation.	87

LIST OF TABLES

4.1	Analysis of the deviation from the ideal line for MOJO runs with varying ε -values for the 10/5-case.	105
4.2	Analysis of the deviation from the ideal line for the objective combinations MN102-MN103, MN102-LLS, and MN103-LLS. .	114
4.3	Analysis of the deviation from the ideal line for the objective combinations MN102-MN103, MN102-LLD, and MN103-LLD. .	114
4.4	Analysis of the deviation from the ideal line and for the Isa Extension case study.	120
A.1	Analysis of the deviation from the ideal line for the MN102-MN103 MOJO run.	139

LIST OF FIGURES

2.1	Workflow of the bootstrap resampling approach.	22
2.2	Definition of nearest neighbours for cell gradient calculation.	27
2.3	True synthetic model and the inversion result based on the data forward calculated from the true model.	30
2.4	Monte Carlo bootstrap results for the synthetic test data.	32
2.5	Relative residuals of the low-noise comparison run minus the master-result.	35
2.6	Map of the station locations of the Delamerian MT transect.	36
2.7	Master-inversion (original data set) of Delamerian MT Transect data set.	37
2.8	Monte Carlo bootstrap results for the Delamerian MT transect data.	39
2.9	Reinterpretation of the master-model for the Delamerian MT transect data, taking into consideration the bootstrap results.	41
2.10	Differences between the residuals of the bootstrap average and the true model and the residuals of the master-model with the true model.	42
3.1	Illustration of Pareto-dominance using the example of a two objective minimisation problem.	55
3.2	Flowchart of the MOJO algorithms functionality.	58

3.3	Illustration of ε -dominance and ε -progress for a hypothetical two objective case.	60
3.4	Conceptual misfit visualisation of two objectives for a hypothetical archive of two compatible data sets.	63
3.5	Conceptual misfit visualisations for two hypothetical pairs of data sets: one pair of compatible data sets and one pair of incompatible data sets.	64
3.6	The synthetic 9-layer model Model I and the synthetic 7-layer model Model II.	67
3.7	Model results from the noise-free 2-objective case.	71
3.8	Pareto-front for the AMT-objective and the BB-objective, and the corresponding Theil-Sen regression, for the compatible noise-free 2-objective case.	72
3.9	Model results from the 2-objective case with 3% noise.	74
3.10	Pareto-front for the AMT-objective and the BB-objective, and the corresponding Theil-Sen regression, for the compatible 2-objective case with 3% noise.	75
3.11	Pareto-front for the AMT-objective and the BB-objective and the corresponding Theil-Sen regression, for the compatible 2-objective case with 3% noise and assigned errors for the BB data set and 5% noise and 5% assigned errors for the AMT data set.	76
3.12	Pareto-front for the AMT-objective and the BB-objective, and the corresponding Theil-Sen regression, for the compatible 2-objective case with 3% noise and assigned errors for the BB data set and 10% noise and 5% assigned errors for the AMT data set.	77
3.13	Model results from the incompatible noise-free 2-objective case.	79

3.14 Pareto-front for the AMT-objective and the BB-objective, and the corresponding Theil-Sen regression, for the incompatible noise-free 2-objective case.	80
3.15 Pareto-front for the AMT-objective and the BB-objective, and the corresponding Theil-Sen regression, for the incompatible 2-objective case with 3% noise.	81
3.16 Model results from the multi-objective case.	83
3.17 Pareto-front for the AMT-BB-objectives, AMT-WELL-objectives and BB-WELL-objectives with the corresponding Theil-Sen regressions, for the multi-objective case.	85
3.18 Pareto-front for the AMT-objective and the BB-objective, and the corresponding Theil-Sen regression, for the 2-objective case without regularisation.	87
 4.1 Illustration of the effects of the ε -values on the solution distributions in objective space.	101
4.2 The true synthetic model for the 10/5-case.	103
4.3 Comparison of the solution distributions and corresponding Theil-Sen regressions for inversion runs of the 10/5-case for ε -values of $\varepsilon = 10^{-1}$, $\varepsilon = 10^{-2}$, $\varepsilon = 10^{-3}$, $\varepsilon = 10^{-4}$, and $\varepsilon = 10^{-5}$	104
4.4 Model distributions of the archive solutions for inversion runs of the 10/5 case for ε -values of $\varepsilon = 10^{-1}$, $\varepsilon = 10^{-3}$, and $\varepsilon = 10^{-5}$, expressed as resistivity value probabilities and interface probabilities.	106
4.5 Model distributions of different subsets of the final archive of the $\varepsilon = 10^{-5}$ run of the 10/5-case, expressed as resistivity value probabilities and interface probabilities.	108
4.6 The synthetic 3-layer models Model- α and Model- ω used to simulate incompatible data.	109

4.7	Model distributions of different subsets of the final archive of the $\varepsilon = 10^{-5}$ run of the synthetic incompatible test case, expressed as resistivity value probabilities and interface probabilities.	109
4.8	Locations of the GEL 185 MT survey lines, including the sites MN102 and MN103 used in this study, and the Moomba-73 well.	111
4.9	Solution distributions for the MN102-MN103-objective, MN102-LLS-objective, and MN103-LLS-objective and the corresponding Theil-Sen regressions.	113
4.10	Model distributions of different subsets of the final archive generated from the joint inversion of the data sets MN102, MN103, and LLS, expressed as resistivity value probabilities and interface probabilities.	115
4.11	Model distributions for the complete archive and the top 10% solution with respect to the best solution generated from the joint inversion of the data sets MN102, MN103, and LLD, expressed as resistivity value probabilities and interface probabilities.	116
4.12	Model responses for the optimal solution generated from the joint inversion of the data sets MN102, MN103, and LLS; MN102, MN103, and LLD; and MN102 and MN103 compared to the measured responses.	117
4.13	Model distributions for the complete archive and the top 10% solution with respect to the best solution generated from the joint inversion of the data sets MN102 and MN103, expressed as resistivity value probabilities and interface probabilities.	118
4.14	Location of the Isa Extension MT survey and the sites IEA00184 and IEB0046 used in this study.	119

4.15 Model distributions of different subsets of the final archive generated from the joint inversion of the IEA00184 and IEB0046, expressed as resistivity value probabilities and interface probabilities.	121
4.16 The modelled responses of the Queensland data sets compared to the measured responses.	123
4.17 Illustration of the different stages of the MOJO workflow . .	125
A.1 Solution distributions for the MN102-MN103-objective, MN102-LLD-objective, and MN103-LLD-objective and the corresponding Theil-Sen regressions.	137
A.2 Solution distribution for the MN102-MN103 MOJO run and the corresponding Theil-Sen regression.	138
A.3 Solution distribution for the Isa Extension Survey data and the corresponding Theil-Sen regression.	138

ABSTRACT

Improving Uncertainty Estimation in Geophysical Inversion Modelling

by Sebastian Schnaitt

Numerical inversion modelling is an integral part of geophysical data interpretation. Growing computational resources are used to invert ever-growing data sets and higher dimensional data. However, models without meaningful uncertainty estimates are difficult to interpret reliably and limited attention has been paid to the advancement of model quality estimation techniques to keep up with the more sophisticated inversion schemes. The employment of meaningful uncertainty estimation methods is often hindered by the complicated implementation of those methods, and inadequate model quality estimators are frequently used. This project was aimed at the advancement of model uncertainty estimation, to enable a more common use.

Two different approaches were developed, approaching the problem from different directions:

Firstly, a bootstrap resampling approach for the qualitative estimation of model uncertainties is presented. The algorithm is characterised by an easy implementation and the fact that it can provide model quality estimation capabilities to existing inversion algorithms without requiring access to the inversion algorithm's source code. A given data set is repeatedly resampled to create multiple realisations of the data set. Each realisation is individually inverted and the variations between the generated models are analysed and visualised to generate interpretable uncertainty maps. The capabilities

ABSTRACT

of the approach are demonstrated using the example of synthetic and real 2-D magnetotellurics data.

Secondly, the multi-objective joint optimisation algorithm MOJO is presented, which aims to remedy the common shortcomings of classical joint inversion approaches. Joint inversion modelling is a powerful tool to improve model results and reduce the effects of data noise and solution non-uniqueness. Nevertheless, the classic joint inversion approaches have a variety of shortcomings, such as a dependency on the choice of data weights, optimising only a single solution resulting in inadequate uncertainty estimates, and the risk of model artefacts being introduced by the accidental joint inversion of incompatible data. MOJO is based on the concept of Pareto-optimality and treats each data set as a separate objective, avoiding data-weighting. The algorithm generates solution ensembles, which are statistically analysed to provide model uncertainty estimates. The shapes and evolutions of the solutions ensemble's distribution in objective space is dependent on the level of compatibility between the data set. The solution distributions are compared against a theoretical solution distribution corresponding to perfectly compatible data to estimate the compatibility state of any given objective-pair, allowing to distinguish between compatible and incompatible data, as well as identify data sets that are neither mutually exclusive nor sensitive to common features. MOJO's effectiveness was demonstrated in extensive feasibility studies on synthetic data as well as real data. The algorithm is adaptive and can be expanded to incorporate a variety of different data types.

Additionally, ways were explored to make the communication of the modelling results and the model quality estimates as clear and concise as possible, to allow the user to make an informed decision and avoid misinterpretations.

Thesis Supervisors: Prof. Dr. Graham Heinson, Dr. Stephan Thiel

STATEMENT OF ORIGINALITY

I certify that this work contains no material which has been accepted for the award of any other degree or diploma in my name in any university or other tertiary institution and, to the best of my knowledge and belief, contains no material previously published or written by another person, except where due reference has been made in the text. In addition, I certify that no part of this work will, in the future, be used in a submission in my name for any other degree or diploma in any university or other tertiary institution without the prior approval of the University of Adelaide and where applicable, any partner institution responsible for the joint award of this degree.

I give consent to this copy of my thesis when deposited in the University Library, being made available for loan and photocopying, subject to the provisions of the Copyright Act 1968.

The author acknowledges that copyright of published works contained within this thesis resides with the copyright holder(s) of those works.

I also give permission for the digital version of my thesis to be made available on the web, via the University's digital research repository, the Library Search and also through web search engines, unless permission has been granted by the University to restrict access for a period of time.

Signed

Date

ACKNOWLEDGEMENTS

Thank you to my supervisors Graham Heinson and Stephan Thiel for giving me the opportunity to come to Adelaide and perform research on this interesting topic. Thanks for letting me work freely, be it day or night, and for always providing support if needed.

Also, thank you to Kelly Keats for giving me the chance to gather valuable experience in the industry.

A special thanks to all my colleagues and fellow Ph.D. students in the geophysics group for creating a friendly working atmosphere and taking the time to discuss and talk, sometimes even about science. Thanks to all the people who helped proof read my papers and also this thesis and making it sound a little less German. This goes especially for Lars who provided critical comments and helped to improve my manuscripts, and was always ready to discuss ideas and help wherever he could.

Thanks for the good times I had on fieldwork and other trips, be it setting up instruments in 45 °C heat or spending a 0 °C night in a van. A special thanks goes to Göran, it is always a pleasure working with you.

Finally, thanks to my family and friends, near and far, for supporting me in this great adventure, especially Benedikt and Lisa for always being there despite the bane of being nine time zones apart. Also, thanks you Kate for being a tireless teacher and a friend on far shores.

The work has been supported by the Deep Exploration Technologies Co-operative Research Centre whose activities are funded by the Australian Government's Cooperative Research Centre Programme. This is DET CRC Document 2015/699.

CHAPTER ONE

INTRODUCTION

1.1 Aims and Objectives

The approaches and methods used for numerical (joint) inversion modelling of geophysical data have come a long way since their first introduction. The improvement has been particularly significant in the last few years: the models have grown in size and 3-D inversion modelling has become a standard tool.

However, much less attention has been paid to the next stage of the inversion modelling process, which is the model assessment stage. This thesis project has been designed to develop methods that would improve the model uncertainty assessment of (joint) inversion models.

This project has explored approaches that add uncertainty estimation capabilities to existing inversion algorithms, and developed an algorithm to improve joint inversion modelling. Simple workflows are presented with the goal to enable any non-specialist to understand and employ the uncertainty estimation approaches developed in this project and utilise the results.

The algorithms presented are designed for electromagnetic data, as this is my field of expertise, and more importantly, ample data sets were available for rigorous testing of the developed algorithms. Nevertheless, all

approaches are generally applicable and are not limited to any one type of data.

1.2 Introductory Background and Literature Review

The inference of geophysical subsurface parameters from gathered geophysical data sets is an integral part of geophysical data analysis and is generally referred to as *geophysical inversion* or *inverse modelling* (Parker, 1994; Hansen et al., 2000; Aster et al., 2012; Haber, 2014; Zhdanov, 2015).

Inverse modelling has undergone a huge development since it was introduced. One might say the first inversions are as old as geophysics itself and were performed inside the geophysicist's head, driven by his lifelong experience, but the inversion modelling as we know it had its hour of birth in the 1960s with the emergence of widely available computing power. Early inversion approaches analytically solved linear problems with very few parameters, such as the depth to buried spheres and similarly simple structures (Telford et al., 1990).

The steady increase in computing power and available memory is closely related to the evolution of inversion techniques and algorithms, but the understanding of the process and the underlying theory has also undergone great advances since the beginning of geophysics. In electromagnetics for example, the introduction of inversion algorithms began in the 1980s with 1-D inversion algorithms (Parker, 1980; Fischer et al., 1981; Parker and Whaler, 1981; Fischer and Le Quang, 1982; Constable et al., 1987), extended to 2-D inversion algorithms in the 1990s (deGroot Hedlin and Constable, 1990; Smith and Booker, 1991; Mackie et al., 1997; Pek and Verner, 1997; Siripunvaraporn and Egbert, 2007), and finally have stepped into the realm of 3-D inversions in the late 1990s and early 2000s (Newman and Alumbaugh, 1997, 2000; Zhdanov and Hursan, 2000; Haber et al., 2004; Newman and Boggs, 2014). Nowadays 3-D inversions are performed on a regular basis (Avdeev and Avdeeva, 2009; Siripunvaraporn and Egbert, 2009; Kelbert et al., 2014). More comprehensive reviews can be found in Avdeev (2005) and Siripunvaraporn (2012).

The basis for most of these algorithms is linear inverse theory, the foundation for which was laid by Backus and Gilbert (1967, 1968, 1970) (for a more recent overview see e.g. Tarantola (2005) and Aster et al. (2012)). The linearised inverse approach is the most commonly used method despite the fact that most geophysical inverse problems are strongly non-linear (Menke, 2012) as it has the advantage of being computationally more efficient than most other methods. However, this technique is far from perfect since the linearisation is always an approximation and the involved partial derivatives are often non-trivial to calculate, which can make the inversion process impractical and/or unstable. Furthermore, these linear local search approaches are prone to stalling at local minima and are usually strongly dependent on the given starting model.

1.2.1 Direct search methods

The shortcomings of conventional inversion methods, as mentioned above, sparked the initial interest in derivative-free direct search methods, which are used to stochastically search the parameter space. Derivative free global direct search methods have several advantages over conventional approaches: they avoid numerical instabilities associated with matrix inversion; they are superior in finding a global extreme; and they are less dependent on the starting model.

One of the first approaches of this kind was the Monte Carlo method (Hammersley and Handscomb, 1964; Halton, 1970), which was introduced to geophysical applications, particularly seismics, as early as the late 1960s (e.g. Keilis-Borok and Yanovskaja, 1967; Press, 1968; Wiggins, 1969; Anderssen, 1970; Anderssen and Seneta, 1971). Their high computational cost, however, made these first attempts impractical without heavily constraining or otherwise reducing the parameter space (e.g. Wiggins, 1969).

The next development in using direct search methods in geophysics was the use of simulated annealing by Rothman (1985, 1986) which was first introduced by Kirkpatrick et al. (1983) and Černý (1985). It is an adapted Monte Carlo method inspired by the annealing technique used in metallurgy to reduce crystal defects (Blundell and Blundell, 2009). Miecznik et al. (2003) for example applied simulated annealing to one-dimensional

magnetotelluric data. More comprehensive summaries can be found in Aarts and Korst (1989) and Sen and Stoffa (2013).

In the 1990s the genetic algorithm (Holland, 1975; Goldberg, 1989; Davis, 1991) made its way into the world of geophysical optimisation problems (Stoffa and Sen, 1991; Sambridge and Drikonigen, 1992; Gallagher and Sambridge, 1994; Nolte and Frazer, 1994; Lomax and Snieder, 1995; Sen and Stoffa, 2013). Genetic algorithms are heuristic search algorithms first developed in the field of artificial intelligence in the computer sciences. These algorithms use techniques emulating natural evolution processes, such as inheritance, mutation, selection, and crossover, to generate new solutions. Everett and Schultz (1993), Pérez-Flores and Schultz (2002) and Wang and Tan (2005) used genetic algorithms to invert two-dimensional magnetotelluric data.

The solution ensembles created with direct search methods can be analysed using classic frequentist statistics (Everitt and Skrondal, 2011) or using Bayesian methods (Gelman et al., 2003; Aster et al., 2012). Bayesian inference is based on Bayes' theorem (Bayes, 1763) and aims to sample the posterior probability density function of each model parameter to estimate model resolution and model uncertainties, while taking into account prior information (Mosegaard and Tarantola, 1995; Tarantola, 2005; Sen and Stoffa, 2013). Bayesian approaches have been applied to a variety of geophysics problems in 1-D inversion modelling (e.g. Tarits et al., 1994; Guo et al., 2011; Ray and Key, 2012), as well as 1-D joint-inversion modelling (Buland and Kolbjørnsen, 2012), and 2-D inversion modelling (Grandis et al., 2002; Chen et al., 2012; Rosas-Carbajal et al., 2014).

Despite all advances made since the introduction of direct search algorithms, these approaches are still hampered by the amount of computing power and memory required. Thus far, the conventional deterministic linear inverse theory methods are still superior with respect to the dimension of the parameter space that can be handled, but the computational power now available has made the new and so far unconventional approaches more feasible and there is no doubt that the future of geophysical inverse modelling will belong to these methods.

1.2.2 Joint inversion

Another problem almost all geophysical methods are afflicted with is solution non-uniqueness (e.g. Anderssen, 1970; Muñoz and Rath, 2006). All sets of data which are not directly measured, but collected remotely, can be explained by an infinite number of different parameter sets of the subsurface parameters under investigation and it is impossible to decide which solution is the true one. Some methods are inherently non-unique, such as all potential field methods (Telford et al., 1990), and others, such as magnetotellurics, are non-unique due to incomplete data (Simpson and Bahr, 2005). The data is usually incomplete because of noise and limited bandwidths. Hence, the electric and magnetic fields measured for magnetotellurics can be explained by an infinite number of totally different subsurface conductivity distributions and the usually necessary linearisation approximations further increase the non-uniqueness.

The inversion can be stabilised by different methods of regularisation (e.g. Parker, 1994; Aster et al., 2012) which introduce additional constraints, such as model smoothness, but this only narrows the solution space and can not solve the problem of non-uniqueness.

One of the most powerful tools for reducing the set of possible solutions is *joint inversion*. Joint inversion and joint interpretation approaches try to find a model that is capable of simultaneously explaining data sets from different geophysical methods. First attempts were made as early as the 1960s for example, by Press and Biehler (1964) who jointly interpreted P-wave delays and gravity anomalies and later by Vozoff and Jupp (1975) who performed joint inversions of DC resistivity and magnetotelluric data.

As Moorkamp et al. (2011) point out, inverting different data sets simultaneously has two major advantages: firstly, different data sets usually have different sources of noise and, therefore, a combined inversion reduces the influence of the noise component. Secondly, different methods have different resolving kernels, which means that each of the methods are sensitive to different petrophysical parameters and thus are capable of resolving different features of a model (e.g. Jegen et al., 2009).

The challenge with every form of joint inversion is to find some sort of relationship between the data under investigation. This is straightforward for data sensitive to the same petrophysical parameter (Yang and Tong, 1988; Julià et al., 2000; Li and Oldenburg, 2000; Commer and Newman, 2009; Abubakar et al., 2011), given that the data are compatible. As soon as one wants to invert data based on different physical parameters the task of finding a relation gets much harder.

There are two major techniques: Direct parameter connection based on an analytical relationship or deduced from an empirical link (e.g. Heincke et al., 2006; Jegen et al., 2009), and/or a structural constraint, such as the cross-gradient (Gallardo and Meju, 2003, 2007), based on the assumption that the structures of the different models resemble each other (Haber and Oldenburg, 1997).

An additional problem is that the links between different methods may vary with the physical conditions in different areas of investigation or even within a survey area. A telling example is the case of electromagnetics and seismics. On the one hand in a sedimentary environment, as is common for hydrocarbon exploration, the porosity of the sediments controls the resistivity as well as the density and elasticity of the medium (Carcione et al., 2007) and thus, a relationship between the two methods exists. However, in a hard rock environment on the other hand, as is the usual case for mineral exploration, such a relationship usually does not exist and structural constraints are only applicable to a limited extend.

To tackle the issue of changing environments and conditions, joint inversion approaches which can handle empirical links as well as structural links have been developed (Moorkamp et al., 2011; De Stefano et al., 2011).

1.3 Model Errors and Uncertainty

1.3.1 Data noise and solution non-uniqueness

Model uncertainty and model errors have a variety of causes, the most obvious one being data noise. In Chapter 2 we give an overview over different methods to estimate the model uncertainty introduced by data noise. The

most common uncertainty estimation techniques usually have some shortcomings, such as complicated implementation or the usually required access to the source code of the inversion algorithm. This leads to the fact that many inversion models are presented with no model uncertainty and quality estimate other than a single scalar value in the form of a misfit value like the RMS deviation (deGroot Hedlin and Constable, 1990; Kelbert et al., 2014). These types of misfit values can be used to compare the relative quality of models based on the same data, but have little significance in judging the quality of a single model.

Another major contributor to model uncertainty is the aforementioned solution non-uniqueness. As previously discussed, jointly inverting multiple data sets can help reduce the number of possible solutions, but can not eliminate solution non-uniqueness altogether. It is not possible to objectively decide which of the solutions is the true one, instead, the choice of ‘best model’ is subjective, based on geological bias. Most current inversion codes search for one best-fit model, although other, possibly very different, models exist that can explain the data equally sufficiently. The found best-fit model might be a local minimum of the model misfit function. Even when a global minimum is found, there is no guarantee that it resembles the ‘true’ Earth. This would not be much of an issue if one could quantify the certainties or likelihood of the model parameters, but as Reading et al. (2011) stress, uncertainty analysis based on a single solution can only account for model uncertainty due to data noise, but will not reflect the inherent solution non-uniqueness. Such approaches, therefore, harbour the risk of missing important model features and thus, potentially missing valuable targets.

Reading et al. (2011), as well as others (e.g. De Stefano et al., 2011) suggest multi-model ensembles as a strategy to deal with this problem, and thus improve the uncertainty analysis of single-domain inversion or joint inversion approaches. The idea is to generate an ensemble of different models that fit the data “sufficiently” well rather than a single best-fit solution. These ensembles then have to be statistically analysed to quantify the solution uncertainty. Direct search methods are a powerful tool to create such ensembles, and have the additional advantage that they do not require linearisation of the problem, which further reduces the non-uniqueness. Indeed,

Monte Carlo methods have originally been introduced to geophysics for the purpose of ensemble creation as used by Press (1968); Wiggins (1969); Anderssen and Seneta (1971); Kennett and Nolet (1978). With the development in the field of direct search methods, more sophisticated approaches have found their way into ensemble creation. Dosso and Oldenburg (1991), for example, used simulated annealing to invert magnetotelluric data, and the use of genetic algorithms can be found in, among many others, Sambridge and Drikonigen (1992); Lomax and Snieder (1995); Moorkamp et al. (2010), whereas, Sambridge (1999a,b) used a neighbourhood algorithm.

Most of these methods were originally developed for optimisation problems and built for rapid convergence to a misfit minimum, rather than for broadly exploring the entire solution space, which is suboptimal for stochastic ensemble generation. Therefore, the algorithms have to be specifically adjusted for the purpose of solution ensemble generation (e.g. Lomax and Snieder, 1995).

Even though multi-model ensemble methods have been used previously, it is only now with the increasing computing power available that they are tractable. There is still a considerable amount of research to be done before these approaches become standard. Especially in the field of joint inversion modelling, the use of multi-model ensembles has to be investigated further. As Reading et al. (2011) discuss, for the time being, these techniques might only be tractable as an aid to the conventional inversion schemes until the available computing power reaches even higher levels and allows for the multi ensemble approaches to be widely used.

1.3.2 User introduced model errors

Data noise and solution non-uniqueness are not the only causes of model uncertainty. Model uncertainty and errors can also be introduced by the user of the inversion algorithm from making incorrect assumptions, such as choosing an inappropriate starting model. Another example is the Bayesian optimisation algorithms (Metropolis and Ulam, 1949; Gamerman, 1997; Rosas-Carbalal et al., 2014), which require parameter priors to be chosen. Any region of the model space that is not included in the prior cannot be

reached by the algorithm, making the choice of priors crucial to the end result.

A further example for crucial assumptions is data weighting. In the classical approaches the misfits of different data sets and the regularisation components are aggregated in a single objective function (Haber and Oldenburg, 1997; Julià et al., 2000; Mota and Monteiro dos Santos, 2006; De Stefano et al., 2011), which requires weighting of the individual data sets (Dobróka et al., 1991; De Nardis et al., 2005). However, a standardised way to find the appropriate weights for different problems does not exist (Treitel and Lines, 1999) and the model results can be negatively influenced by choosing inappropriate weights (De Stefano et al., 2011).

In the case of joint inversion modelling the aggregation of all misfit functionals into one objective function causes an additional problem as it makes it difficult to judge the compatibility of the jointly inverted data sets (Moorkamp et al., 2010). When jointly inverting multiple data sets it has to be ensured that the data are sensitive to common features and that the connection assumed between the data sets is valid. Otherwise, model artefacts will be introduced into the model result as the inversion algorithm attempts to compensate for the incompatibility.

1.4 Overview

This thesis consists of five chapters, including this introduction and a general discussion and summary at the end of the thesis.

Chapters 2 – 4 form the main body of this thesis and consist of articles that have been published in peer-reviewed journals or are intended for publication in peer-reviewed journals.

Following, I will give a short review of the three main chapters:

CHAPTER 2

Bootstrap Resampling as a Tool for Uncertainty Analysis in 2-D Magnetotelluric Inversion Modelling

Schnaidt, S., Heinson G. (2015). *Geophys. J. Int.*, 203(1):92-106. doi: 10.1093/gji/ggv264.

Chapter 2 addresses the problem of uncertainty estimation, and explores a pragmatic approach to bootstrap resampling as a method for the qualitative estimation of model uncertainties in geophysical inversion modelling. The approach can be employed with almost any inversion algorithm without the need for access to the source code, and can supply crucial uncertainty estimates in situations where more sophisticated methods cannot be implemented. The effectiveness of bootstrap resampling is demonstrated with synthetic and real data case studies.

CHAPTER 3

A Novel Approach to Pareto-optimal Joint Inversion Modelling and Data Set Compatibility Analysis of Geophysical Data

Schnaidt, S., Krieger L., Heinson G. (2015).

This chapter introduces MOJO, a multi-objective joint inversion algorithm. MOJO is a solution population based algorithm that solves common problems of the classic joint inversion approach, such as the inherent risk of weighting bias and the question of data set compatibility. It is designed to jointly invert a number of data, while avoiding data weighting by treating each data set as a separate objective. The algorithm assesses the compatibility of jointly inverted data sets prior to a main inversion run to avoid the introduction of model errors and uses statistical analysis of the generated solution ensembles to infer model uncertainties. The algorithm is introduced and its capabilities are demonstrated.

CHAPTER 4

Parameter Studies of Geophysical Joint Inversion Modelling - Using Multi-objective Optimisation

Schnaidt, S., Krieger L., Heinson G. (2015). *Geophys. J. Int.*; submitted

The third article extends the previous chapter to address identified issues. Parameter dependencies of the compatibility analysis and the generated model distributions are investigated to increase the reliability of the compatibility analysis. Furthermore, MOJO's effectiveness under real world conditions is explored in two case studies, to analyse the effects of real data that can not be simulated with synthetic data. These include higher complexity and real world noise.

CHAPTER
TWO

BOOTSTRAP RESAMPLING AS A TOOL FOR
UNCERTAINTY ANALYSIS IN 2-D
MAGNETOTELLURIC INVERSION MODELLING

SEBASTIAN SCHNAIDT^{1,2} AND GRAHAM HEINSON²

¹Deep Exploration Technologies Cooperative Research Centre,
Adelaide Airport SA 5950, Australia

²Electrical Earth Imaging Group, Department of Earth Sciences,
School of Physical Sciences, University of Adelaide, Adelaide SA 5005, Australia

Published on August 7th, 2015 as:

Schnaidt, S. and Heinson, G. (2015). Bootstrap resampling as a tool for uncertainty analysis
in 2-D magnetotelluric inversion modelling. *Geophys. J. Int.*, 203(1):92-106. doi:
10.1093/gji/ggv264.

Statement of Authorship

Title of Paper	Bootstrap Resampling as a Tool for Uncertainty Analysis in 2-D Magnetotelluric Inversion Modelling
Publication Status	<input checked="" type="radio"/> Published, <input type="radio"/> Accepted for Publication, <input type="radio"/> Submitted for Publication, <input type="radio"/> Publication style
Publication Details	Schnaidt, S. and Heinson, G. (2015). Bootstrap resampling as a tool for uncertainty analysis in 2-D magnetotelluric inversion modelling. Geophys J. Int., 203(1): 92-106. doi: 10.1093/gji/ggv264

Author Contributions

By signing the Statement of Authorship, each author certifies that their stated contribution to the publication is accurate and that permission is granted for the publication to be included in the candidate's thesis.

Name of Principal Author (Candidate)	Sebastian Schnaidt
Contribution to the Paper	Developed code and method, designed and performed analysis, wrote and edited manuscript, and acted as corresponding author
Signature	Date 2015-09-11

Name of Co-Author	Graham Heinson
Contribution to the Paper	Provided initial motivation for work, supervised development of work, and provided critical manuscript evaluation
Signature	Date 8 / 9 / 15

Name of Co-Author	N/A
Contribution to the Paper	N/A
Signature	Date

Name of Co-Author	N/A
Contribution to the Paper	N/A
Signature	Date

SUMMARY

Uncertainty estimation is a vital part of geophysical numerical modelling. There exist a variety of methods aimed at uncertainty estimation, which are often complicated and difficult to implement. We present an inversion technique that produces multiple solutions, based on bootstrap resampling, to create a qualitative uncertainty measure for 2-D magnetotelluric inversion models. The approach is easy to implement, can be used with almost any inversion code, and does not require access to the inversion software's source code. It is capable of detecting the effect of data uncertainties on the model result rather than just analysing the effect of model variations on the model response. To obtain uncertainty estimates for an inversion model, the original data set is resampled repeatedly and alternate data set realisations are created and inverted. This ensemble of solutions is then statistically analysed to determine the variability between the different solutions. The process yields interpretable uncertainty maps for the inversion model and we demonstrate its effectiveness to qualitatively quantify uncertainty in synthetic model tests and a case study.

2.1 Introduction

Numerical inversion has become a standard approach in the interpretation of data from electromagnetic (EM) measurements. Models are a widely traded commodity in research as well as in the exploration industry. This requires them to be highly reliable to ensure correct interpretation, which can only be achieved if model shortcomings and the model parameter uncertainties are thoroughly understood.

The model appraisal tool bag contains a variety of different techniques and methods to quantify the influences of data noise, incorrect a priori assumptions, and solution non-uniqueness on model resolution, model sensitivity, and parameter uncertainties of EM models. To put the uncertainty estimation technique presented in this paper into perspective, we will first mention some examples of alternative methods and groups of methods to analyse different aspects of model uncertainty and discuss their advantages and shortcomings. Note that our list is in no way complete. For a general overview of geophysical inversion modelling see, for example, Parker (1994); Hansen et al. (2000); Aster et al. (2012); Haber (2014); Zhdanov (2015).

Parameter uncertainties can, for example, be analysed using the *model covariance matrix* (MCM; Meju, 1994; Tarantola, 2005; Alumbaugh and Newman, 2000; Menke, 2012) or via full probabilistic *Markov chain Monte Carlo* (MCMC) inversion (Rosas-Carbajal et al., 2014), and parameter ranges can be estimated with *most-squares* inversions (Jackson, 1976; Meju and Hutton, 1992; Kalscheuer et al., 2010). The sensitivity of a model can be assessed via the *Jacobian matrix* (sensitivity matrix) and by manual forward and inversion modelling tests of perturbed model results (e.g. Becken et al., 2008; Thiel and Heinson, 2010). Another method to test model features on their reliability is to use the model's *null-space* (Muñoz and Rath, 2006), and model resolution can be estimated by analysing the *model resolution matrix* (MCM; Jackson, 1972; Meju, 1994; Ramirez et al., 1995; Menke, 2012). Below we will discuss these methods in more detail.

Monte Carlo methods (Metropolis and Ulam, 1949) are commonly used in the determination of different kinds of uncertainty. They produce an ensemble of equally possible solutions that is used to calculate posterior probabil-

ity distributions for the model parameters via Bayesian inference (Gelman et al., 2003; Aster et al., 2012). These give direct indications of model resolution and parameter uncertainties. As random searches are computationally expensive, usually MCMC methods (e.g. Gamerman, 1997) are used for numerical inversion modelling, instead of straight Monte Carlo searches. Rosas-Carbajal et al. (2014) employed a pixel-based, fully probabilistic MCMC inversion for 2-D plane wave EM data. To make the inversion computationally feasible, the model structure has to be constrained. Rosas-Carbajal et al. (2014) point out that the uncertainty estimates are to some extent determined by these constraints and that the constraints might lead to biased models. Other factors influencing the results are the model parameterisation and the number of parameters, which seem to have great impact on the posterior probability distributions (Laloy et al., 2012; Linde and Vrugt, 2013), as well as the important choice of the parameter priors necessary for the inversion. The result of an MCMC inversion strongly depends on the used prior, as the resulting model can only reach regions of the model space that are contained in the prior. Hence, an insufficient prior can have adverse effects on the result.

Rosas-Carbajal et al. (2014) were not the first to use Bayesian inference and MCMC in EM inversion modelling. This method has been used previously in 1-D modelling (Tarits et al., 1994; Guo et al., 2011; Buland and Kolbjørnsen, 2012; Ray and Key, 2012), 2-D modelling (Chen et al., 2012), and even 3-D modelling (Grandis et al., 2002). MCMC methods are still too computationally demanding to perform full 3-D inversions, but Grandis et al. (2002) used thin-sheet modelling to increase the computational efficiency, while limiting the accuracy to thin structures.

Rosas-Carbajal et al. (2014) compared the uncertainty estimates of the MCMC inversion with results from a most-squares inversion (Jackson, 1976; Meju and Hutton, 1992), which has also been used by Kalscheuer et al. (2010) for joint inversion of direct current resistivity and radio-magnetotelluric data. Most-squares inversions are used to find the extremal values that the parameters of each model cell can adopt without altering the misfit beyond a specified threshold with respect to the best-fitting inversion model found by conventional means. This gives information about the feasible model ranges and model non-uniqueness.

MCM analysis (Meju, 1994; Tarantola, 2005; Menke, 2012) is, for example, used by Alumbaugh and Newman (2000). They used a linearised MCM approach to assess EM models from 2-D and 3-D inversions. The MCM contains the covariances between all parameters and the diagonal of the matrix represents the parameter variances. Usually the square root of these values is plotted to produce an image of the parameter standard deviations, which gives an estimate of how the parameter errors are influenced by data noise and incorrect a priori assumptions. These are valuable information, but they have to be treated with care. Alumbaugh and Newman (2000) suggest that the reliability of the linearisation, necessary to calculate the MCM for the highly non-linear EM problem, is difficult to determine. The need to linearise a non-linear problem might underestimate the error levels. The authors suggest that performing full non-linear inversions of multiple realisations of the model with different data and smoothing vectors could produce different results. However, this does not lessen the (at least qualitative) value of the information about the model quality that can be gained.

Alumbaugh and Newman (2000) also used a linearised approach to determine the MRM (Jackson, 1972; Meju, 1994; Ramirez et al., 1995; Menke, 2012). As with the MCM, usually the diagonal of the MRM is evaluated to gain information about the model resolution. However, the calculation and evaluation of the MRM suffer from similar problems as the MCM.

The methods discussed so far mostly estimate model parameter uncertainties. A different group of techniques is used to analyse the sensitivity of the model and the reliability of specific model features. Muñoz and Rath (2006) use a null-space projection technique to test the non-uniqueness of magnetotelluric models. The method has first been employed by Deal and Nolet (1996) and Rowbotham and Pratt (1997) on seismic tomography inversions and is based on perturbations of the best-fitting model generated with a standard inversion run. The parameters of the model to be analysed are perturbed by small amounts multiple times and those changes are projected onto the original model's null-space, producing multiple realisations of the model. Due to the projection of the changes onto the model's null-space the model misfit is not altered. This corresponds to the exploration of the parameter space close to the original model. The resolution and reliability of model structures can then be assessed by comparing the

differences and similarities of the inversion results of the new models. It is important to note that this technique does not make any statement as to how small changes to the data, for example those caused by noise, influence the model response. The method also has a few issues. First, the approach will only yield correct results if the chosen base model is close to the true model, which the whole process tries to determine. Second, the choice of setup parameters can greatly influence the outcome. Especially the null-space is greatly dependent on parameter choices and can vary significantly, which will influence the results.

A common method to determine the reliability and sensitivity of model structures is based on models that are manually perturbed and tested against the original model result via forward and inversion modelling (e.g. Becken et al., 2008; Thiel and Heinson, 2010). Its common use is founded in its relative simplicity and its comparatively easy implementation. To test structures and features of a model found by classic inversion, the model cells representing these features are changed to parameter values corresponding with the model background. These test models are then assessed by forward modelling or by using the new model, with the perturbed regions held fixed, as the starting model for additional inversions. Deterioration of the misfits of these new models would then indicate that the model features in question are constrained by the data. This checks to what extent the features in question are required by the data with certain error estimates.

In addition to model perturbation tests, Thiel and Heinson (2010) analyse the Jacobian matrix (sensitivity matrix), which provides information on the influence of small changes to a model parameter on the model response. Both the model perturbation method and the sensitivity matrix analysis suffer from the same shortcoming as the null-space projection approach discussed earlier; they only investigate how changes to the model influence the model response. In contrast the influence of perturbations to the data with regard to their error estimates cannot be inferred directly.

The methods described provide valuable information about the quality and reliability of models, but also have their shortcomings. They are often relatively complicated to implement, especially if one does not have access to the source code of the used inversion software.

In this paper we present an approach to assess the effect of data errors on model uncertainty and reliability in 2-D MT inversion modelling using bootstrap resampling (Efron, 1979, 1982). Like MCMC methods our approach creates multiple solutions. The exploration of the solution space is less comprehensive than with MCMC methods, which means the bootstrap approach yields qualitative rather than quantitative uncertainty estimates, while achieving higher computational efficiency. The model uncertainty is assessed with respect to a set of fixed starting parameters. The original data are resampled repeatedly, creating multiple realisations of the data set, which are each inverted to create a solution ensemble. This ensemble is statistically analysed to determine differences and similarities between the different solutions, allowing conclusions about the model quality. Our approach has the advantage of giving an indication of the effect of the data uncertainties on the model outcome, while being easy to implement. The method can be realized with almost any existing inversion code, as the availability of the inversion software's source code is not essential. Only a limited amount of new code has to be developed.

In the remainder of the paper we will describe our method, and especially bootstrap resampling, in more detail (Section 2.2), describe how the produced solution ensembles are analysed (Section 2.3), demonstrate the approach with a synthetic data example as well as a real world case study (Section 2.4), and finish the paper with a discussion of our findings (Section 2.5).

2.2 Method

2.2.1 Bootstrap resampling

Bootstrapping (Efron, 1979, 1982) is a resampling method used in statistics to calculate sample estimates by random sampling with replacement. It is based on resampling a sample population of fixed size, creating multiple realisations, and calculating the statistical property of interest for all realisations, which allows for inference of statistical accuracy measures for the property, such as sample averages and variances. The strength of the bootstrapping method is that it is easy to implement and enables the estimation

of any statistic, regardless of its complexity. This comes at the price of a higher computational cost, which nowadays is not much of a problem, as computational power is abundant.

The bootstrapping method was first introduced to the field of geophysics by McLaughlin (1988), who used it to estimate the uncertainty of seismic event magnitudes, and by Tichelaar and Ruff (1989), who used bootstrapping and other resampling techniques in a case study on the calculation of earthquake epicentre depths. Bootstrapping has since been used in seismology and seismic tomography on a regular basis for error and significance estimations for velocity data stacks (Flanagan and Shearer, 1998; Gurrola and Minster, 1998; Korenaga, 2013, 2014), to estimate uncertainties on earthquake locations (Shearer, 1997), in the analysis and inversion of velocity data (Koch, 1992; Gurrola et al., 1994; Sacchi, 1998; Choi et al., 2010), and to assess shear wave splitting errors (Sandvol and Hearn, 1994). Bootstrapping is also used in magnetics, for example in the analysis of magnetic susceptibility data (Tauxe et al., 1998), in error estimation for paleomagnetic data (Tauxe et al., 1991; Guyodo and Valet, 1996; Shaar et al., 2011), and for evaluating geomagnetic dipole intensities (Jonkers, 2007). In MT, the bootstrap method has not been used for modelling yet, but has been utilized in the estimation of MT transfer functions (Campanya et al., 2014; Chave, 2014a; Neukirch and Garcia, 2014) and the estimation of error of rotational invariant parameters (Martí et al., 2004; Chave, 2014b).

Given an N -element data set $X = \{x_1, \dots, x_N\}$, k bootstrap realisations X'_i , $i = \{1, \dots, k\}$ are created by performing N random draws with replacement from X for each bootstrap data set. This means each new data set has the same number of elements as the original set and the bootstrap data sets can contain some elements multiple times and might not contain some of the original elements at all. As mentioned before, the statistic of interest is then evaluated for each bootstrap set producing k solutions, from which solution averages and variances can be calculated.

We apply the bootstrapping principle to 2-D MT data (Figure 2.1). In our case, the properties of interest are the cell resistivity values of a model resulting from a numerical inversion performed on the data sets. To perform these inversions we use *Occam's* inversion for 2-D MT data (Constable et al., 1987; deGroot Hedlin and Constable, 1990) (Section 2.2.2). A

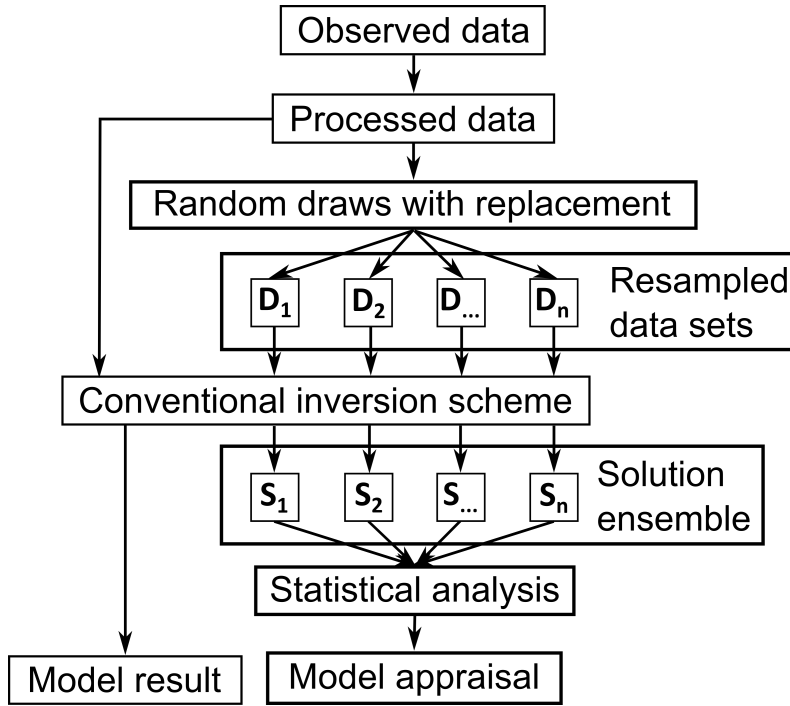


Figure 2.1: Workflow of the bootstrap resampling approach.

data element for the purpose of the bootstrap is equivalent to a data block containing the processed data for a specific evaluation frequency of a specific MT site. Each data block contains four elements: the values for the \log_{10} -scaled apparent resistivity $\rho^* = \log_{10}(\rho)$ and the phase ϕ for each the transverse electric (TE) mode and the transverse magnetic (TM) mode. By treating a whole data block as a contained unit rather than employing the bootstrap on the single data values, we avoid the creation of model artefacts, due to incomplete data for a certain frequency and site. Artefacts caused by the bootstrapping process have to be avoided, as they would be misinterpreted for uncertainty caused by the data.

The resampling process simulates repeated measurements and is executed in two stages. In the first stage a data block is drawn at random from a uniform distribution of the complete set of data blocks. For the second stage an error model with normally distributed data errors is assumed and Monte Carlo samples are created from the data blocks drawn in the first stage. The Monte Carlo samples are created by drawing from a normal distribution $x \sim \mathcal{N}(\mu, \sigma)$, with the value of the element (linear resistivity ρ or phase ϕ) as the expected value μ of the normal distribution and the error

assigned to the particular data block element as the standard deviation σ of the distribution. By sampling from these distributions of the values, the created bootstrap sets are equally likely realisations as the original measured data set. These are inverted with the same starting models and the same starting parameters, to then assess the differences and similarities between the bootstrap models, which are indicators of model uncertainty. The starting parameters for each group of bootstrap samples have to be identical to make them comparable and the uncertainty estimates will to some degree be dependent on the choice of starting parameter.

Model areas that show good accordance across the different model results are considered well determined and areas of large variability exhibit elevated uncertainty. In the case of perfect, noise free data all model results will be equal or at least very similar. Small variations would be caused by the fact that the samples are drawn with replacement and each bootstrap set is different, but even if certain data points are not drawn in a particular bootstrap set, the results would be very similar. This is due to the fact that in MT neighbouring frequencies contain similar information. Thus, most of the potentially missing information is contained in other data blocks. This is caused by the diffusive nature of the EM fields, which results in MT measurements representing averages over the volume of medium penetrated by the EM fields. Hence, Weidelt's dispersion relation (Weidelt, 1972):

$$\phi(\omega_0) = \frac{\pi}{4} - \frac{\omega_0}{\pi} \int_{\mathcal{P}}^{\infty} \log\left(\frac{\rho_a(\omega)}{\rho_0}\right) \frac{d\omega}{\omega^2 - \omega_0^2}, \quad (2.1)$$

which relates the apparent resistivity ρ_a to the impedance phase ϕ , predicts similar results for neighbouring frequencies $\omega = 2\pi f = 2\pi/T$.

There might be instances where a model includes regions that the data are not sensitive to, for example at great depth or far away from the sites. The resistivity distribution of these regions would greatly depend on the generally subjective choice of the starting model and other starting parameters, and would experience little to no change during the modelling and across all bootstrap realisations. This would lead to these regions being assigned high certainty even though the data does not have any sensitivity in these areas. To avoid this kind of misinterpretation, one should always analyse to which depth the model is actually supported by the data and does not only consist of artefacts. One method to do this is the *depth of investigation* in-

dex (DOI) developed by Oldenburg and Li (1999). The DOI is assessed by running multiple inversions with different starting models and comparing the differences and similarities (Oldenburg and Li, 1999; Marescot et al., 2003), to help avoid overinterpretation of the inversion result(s). Nevertheless, the influence from the starting model and other prior information, and therefore the potential for bias, increases with depth even above the depth threshold suggested by the DOI analysis.

2.2.2 Occam's inversion

Occam's inversion is a regularized smooth inversion algorithm, first employed for 1-D MT data by Constable et al. (1987) and later expanded by deGroot Hedlin and Constable (1990) to handle 2-D MT data. We chose this algorithm as it is still commonly used and is an accepted reference.

The algorithm uses a Tikhonov-type regularisation (Tikhonov and Arsenin, 1977) to regularize the inversion models by applying a penalty on the roughness of the model, seeking the smoothest model under the constraint that it explains the observed data to a degree specified by a desired data misfit Γ_*^2 . Model roughness is measured by the magnitude of the first or second derivative of the model resistivities. Assuming a 2-D structure with strike direction x the first derivative roughness of the M -element model vector \mathbf{m} in the lateral direction y and the vertical direction z is given by:

$$R_1 = \|\underline{\partial}_y \mathbf{m}\|^2 + \|\underline{\partial}_z \mathbf{m}\|^2. \quad (2.2)$$

By penalizing roughness, the simplest model that can fit the data to the desired misfit is sought. This ensures the principle of Ockham's Razor is followed, which states that the simplest solution to a problem is to be preferred. Thereby, unnecessarily complex models and the formation of model artefacts are avoided. Furthermore, the regularisation stabilizes the inversion process.

During the inversion, the algorithm minimizes a constrained objective functional U that contains the model roughness term and a model misfit term:

$$U[\mathbf{m}] = \underbrace{\|\underline{\partial}_y \mathbf{m}\|^2 + \|\underline{\partial}_z \mathbf{m}\|^2}_{\text{model roughness}} + \mu^{-1} \underbrace{[\|\mathbf{W}(\mathbf{d} - F(\mathbf{m}))\|^2 - \Gamma_*^2]}_{\text{model misfit}}, \quad (2.3)$$

where \mathbf{d} is the N -element data vector, F is the non-linear forward operator (Wannamaker et al., 1987), μ^{-1} is the Lagrange multiplier, and \mathbf{W} is the diagonal covariance weighting matrix, containing values inversely proportional to the standard deviation of the data errors.

The Lagrange multiplier μ^{-1} acts as a weighting parameter between the model roughness and the model misfit and is chosen automatically at each iteration to achieve the desired misfit.

If the desired misfit is not reached after the maximum number of iterations, it is common practice to rerun the inversion for a small amount of iterations using the last model result of the run as the starting model and using the achieved misfit increased by 5–10 % as the new desired misfit. This allows the algorithm to smooth out the model to find the simplest viable model and reduce model artefacts.

2.3 Ensemble Appraisal

After an ensemble of model solutions has been created from a set of resampled data, the variations between these model solutions have to be analysed to create uncertainty maps for the related *master-model*, which is based on the original data set.

We quantify uncertainty as the differences in the absolute cell value (resistivity) and the variations of the cell gradients across all models in the ensemble.

2.3.1 Variability in absolute value

Resistivities are usually considered a logarithmic parameter, as they generally show large variations. Hence, all calculations are performed with logarithmically scaled resistivities $\rho_i^*(y, z) = \log_{10}(\rho_i(y, z))$. The variation in absolute cell values are determined for each model cell by calculating the deviations of the cell resistivities $\rho_i^*(y, z)$ from the cell average $\bar{\rho}_w(y, z)$ over all k models of the ensemble.

As each bootstrap data set is different, the resulting inversion models will most likely have slightly differing misfit values. To avoid biasing the results we weight each solution with its misfit δ to calculate a weighted mean for each cell:

$$\bar{\rho}(y, z) = \frac{\sum_{i=1}^k \delta_i \cdot \rho_i^*(y, z)}{\sum_{i=1}^k \delta_i}. \quad (2.4)$$

The variance of the value of a specific model cell $\sigma_\rho^2(y, z)$, and thereby the standard deviation $\sigma_\rho(y, z)$, is given by

$$\sigma_\rho^2(y, z) = \frac{\left(\sum_{i=1}^k \delta_i \cdot (\rho_i^*(y, z) - \bar{\rho}(y, z))^2 \right) \cdot \sum_{i=1}^k \delta_i}{\left(\sum_{i=1}^k \delta_i \right)^2 - \sum_{i=1}^k \delta_i^2}. \quad (2.5)$$

The standard deviation $\sigma_\rho(y, z)$ of the resistivity values $\rho_i^*(y, z)$) represents the variability of the absolute cell value across the ensemble. To allow for a comparison of the standard deviation of different cells, the relative standard deviation $\sigma_{\rho,\text{rel.}}(y, z) = \sigma_\rho(y, z)/\bar{\rho}(y, z)$ is displayed in the final uncertainty map, rather than the absolute standard deviation.

2.3.2 Variability in cell gradient

By only evaluating the variability of the absolute cell values we can not distinguish between actual differences in magnitude and differences in structure. There might arise situations where the absolute cell values show high variability, but the different models show good structural agreement, which would indicate uncertainty in the absolute resistivity of anomalies, but nevertheless robustness in the position and shape of structures.

To evaluate the structural similarity between the ensemble members, we assess the variability in the cell gradients. The model parameter vector \mathbf{m} , containing the \log_{10} -scaled resistivities, are analysed. For the 2-D case

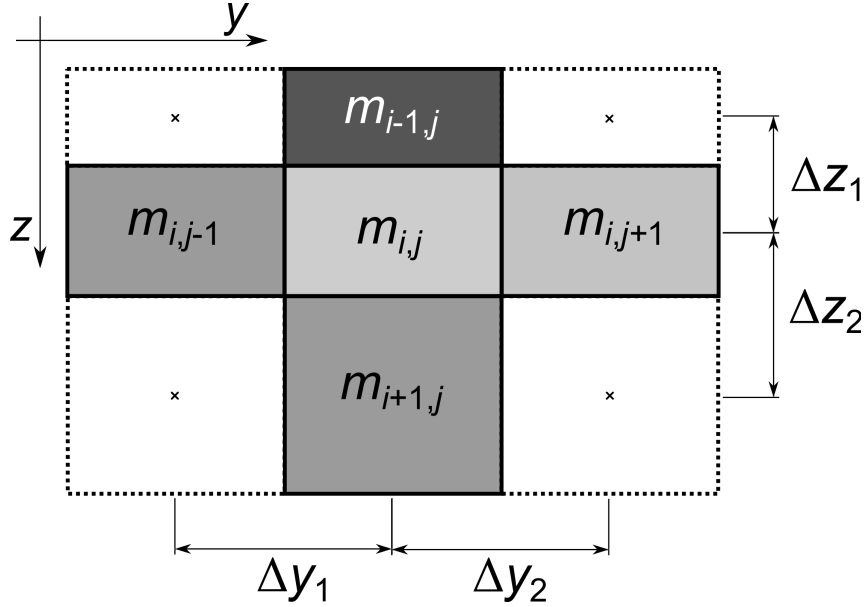


Figure 2.2: Definition of nearest neighbours for cell gradient calculation. Only adjacent cells are considered.

$\mathbf{m}(y, z)$ the gradient of the cell in the i th row and the j th column of the model mesh is defined as:

$$\nabla m_{i,j}(y, z) = \frac{\partial m_{i,j}}{\partial y} \hat{e}_y + \frac{\partial m_{i,j}}{\partial z} \hat{e}_z . \quad (2.6)$$

The derivatives in Equation 2.6 are estimated by first differences

$$\frac{\partial m_{i,j}}{\partial y} \cong \frac{1}{2} \left(\frac{m_{i,j} - m_{i,j-1}}{\Delta y_1} + \frac{m_{i,j+1} - m_{i,j}}{\Delta y_2} \right) \quad (2.7a)$$

$$\frac{\partial m_{i,j}}{\partial z} \cong \frac{1}{2} \left(\frac{m_{i,j} - m_{i-1,j}}{\Delta z_1} + \frac{m_{i+1,j} - m_{i,j}}{\Delta z_2} \right) . \quad (2.7b)$$

The notation is illustrated in Figure 2.2, which displays the five-cell scheme that is used for the calculation of the first differences.

The cell gradients of two models are compared by calculating the cell cross-gradients $\mathbf{cg}(y, z)$ (cross product of the gradients)

$$\mathbf{cg}(y, z) = \nabla m_{i,j}^\alpha(y, z) \times \nabla m_{i,j}^\beta(y, z) \quad (2.8)$$

between the two models α and β , which becomes large if the difference in gradient direction is large and small when the difference in gradient direction is small.

Using the dot product, the angle of aperture of the two gradients θ can be calculated:

$$\begin{aligned}\nabla m_{i,j}^{\alpha} \cdot \nabla m_{i,j}^{\beta} &= \|\nabla m_{i,j}^{\alpha}\| \|\nabla m_{i,j}^{\beta}\| \cos \theta \\ \Rightarrow \quad \theta &= \arccos\left(\frac{\nabla m_{i,j}^{\alpha} \cdot \nabla m_{i,j}^{\beta}}{\|\nabla m_{i,j}^{\alpha}\| \|\nabla m_{i,j}^{\beta}\|}\right).\end{aligned}\quad (2.9)$$

These angle differences are calculated for all possible pair combinations of the models in the solution ensemble and the average for each model cell is displayed as an uncertainty map. With k models there are

$$\binom{k}{2} = \frac{k!}{2!(k-2)!} = \frac{1}{2} \cdot k \cdot (k-1) \quad (2.10)$$

unique pair combinations.

2.4 Results

To demonstrate our bootstrapping approach, we employ it on a synthetic model case, as well as real world data.

The number of bootstrap samples that can be used in the tests is mostly limited by the computing power available. One should evaluate as many samples as is reasonable, as even though more samples cannot increase the amount of information in the original data, more samples increase the reliability of the statistic calculated and reduce possible bias. Efron and Tibshirani (1986) performed tests on the ideal parameters for bootstrapping and came to the conclusion that $k \in [50, 200]$ bootstrap realisations are enough to yield meaningful results in most cases. They state, that as few as $k = 25$ realisations give acceptable results and that there is not much improvement observable for $k > 100$. During our testing we found that as little as 20 bootstrap sets are enough to yield qualitative useful results, but we use 100 bootstrap samples in each of our tests, to ensure robust results.

2.4.1 Synthetic test case

For our synthetic test case we used a model similar to the synthetic models from Kalscheuer et al. (2010) and Rosas-Carbajal et al. (2014). It includes

a high-resistivity structure covering a low-resistivity structure, as well as the opposite setup. The model is simple enough to serve as a controllable test environment, but is complex enough to predict the results of the bootstrapping techniques for a variety of modelling situations.

The model has a $100 \Omega\text{m}$ background resistivity (Figure 2.3a). On the left side of the model a resistive block R_l ($1000 \Omega\text{m}$) is positioned 3.35 km above a conductive block C_l ($10 \Omega\text{m}$) and on the right side of the model a conductive block C_r ($10 \Omega\text{m}$) is positioned above a resistive block R_r ($1000 \Omega\text{m}$). The blocks on both sides have the same dimensions, with the top blocks starting at a depth of 3.1 km and being 13.3 km wide and 2.9 km high, and the bottom blocks starting at a depth of 9.35 km and being 8 km wide and 2.3 km high. The top blocks are 8 km apart and the bottom blocks are 13.3 km apart.

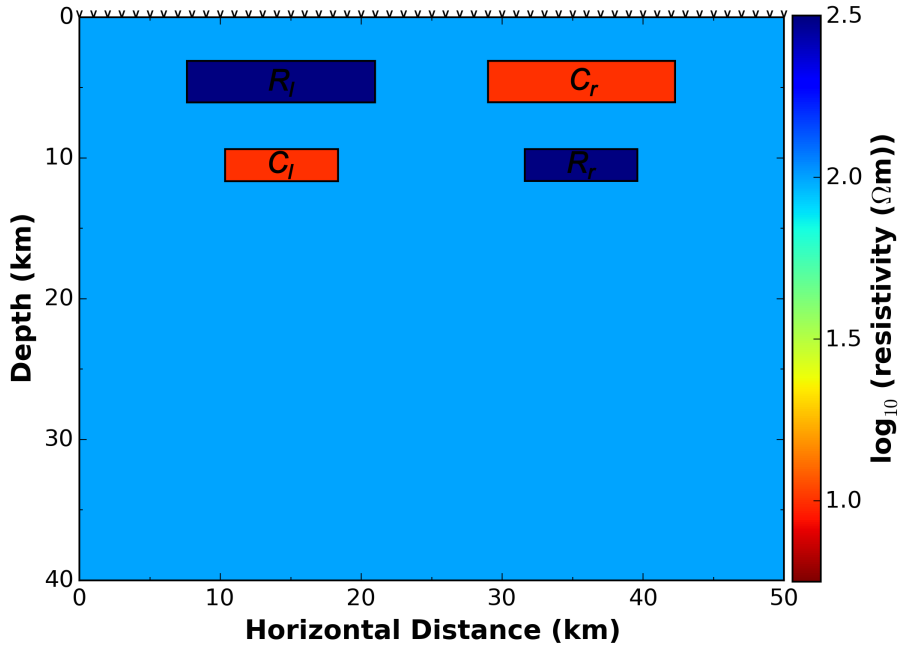
Forward data for 51 sites at a 1 km spacing for 42 frequencies in the range of $0.012 - 156.25 \text{ Hz}$ were calculated with the finite element 2-D forward code by Wannamaker et al. (1987). This resulted in 2142 data blocks with apparent resistivities and phases for transverse electric (TE) and transverse magnetic (TM) mode. White noise with a standard deviation equivalent to 5 % of the linearly-scaled resistivity amplitudes was added to the forward data. Under the standard assumption that the errors of the complex impedances are equal in the real and imaginary components the error of the phase σ_ϕ is related to the error of the resistivity σ_ρ by

$$\sigma_\phi = \arcsin\left(\frac{1}{2} \frac{\sigma_\rho}{\rho}\right) \quad (2.11)$$

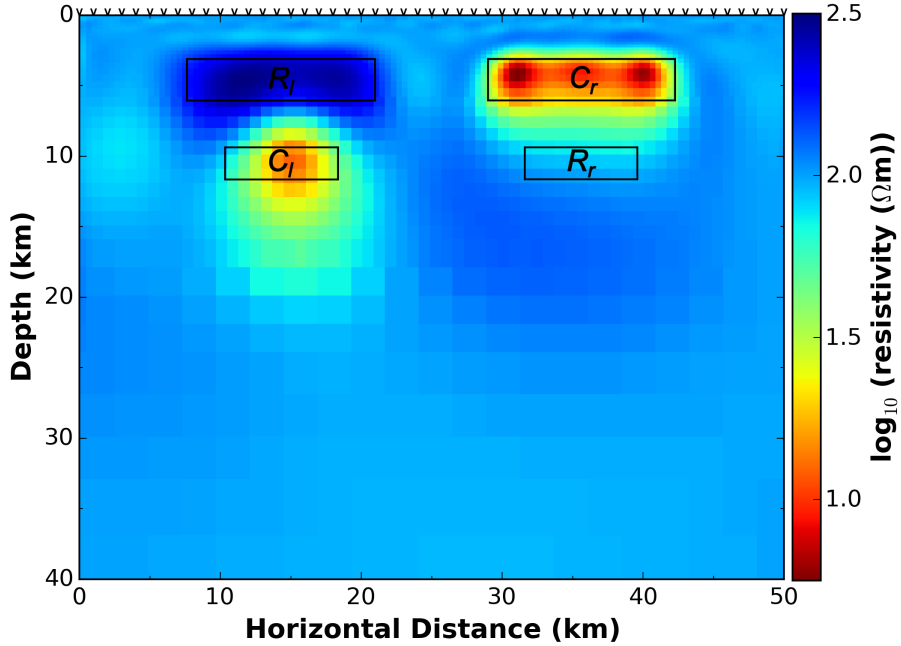
Accordingly, white noise with a standard deviation of $\sigma_\phi = \arcsin\left(\frac{1}{2} \cdot 0.05\right) \approx 1.43^\circ$ was added to the phase values. This is commonly (misleadingly) referred to as ‘5 %’ phase errors.

2.4.1.1 Conventional inversion

The complete data set was inverted with the Occam 2-D code (deGroot Hedlin and Constable, 1990), described in Section 2.2.2, using a $100 \Omega\text{m}$ half-space as the starting model (Figure 2.3b). A mesh different from the



(a) True synthetic model. The bodies R_l and R_r have a resistivity of $1000 \Omega\text{m}$, the bodies C_l and C_r have a resistivity of $10 \Omega\text{m}$, and the background has a resistivity of $100 \Omega\text{m}$. The scale has been limited to $10^{2.5} \Omega\text{m} = 316 \Omega\text{m}$ for easier comparison with the inversion results.



(b) Master-inversion.

Figure 2.3: (a) True synthetic model and (b) the inversion result based on the data forward calculated from the true model. Black \vee mark the locations of the 51 simulated recording sites. The true locations of the four anomalous bodies R_l , C_l , C_r , and R_r are marked with black boxes.

synthetic forward mesh was used for all inversions to avoid biasing the results.

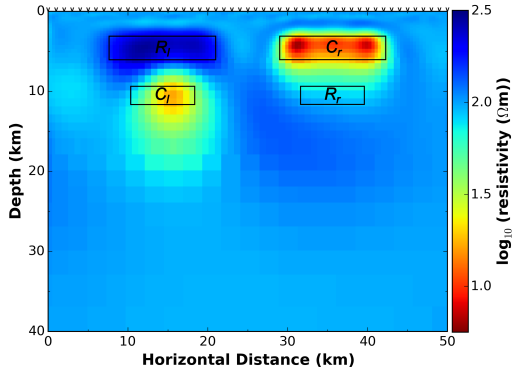
The inversion recovers structures R_l and C_r reasonably well. Both structures are smeared out, especially in the vertical direction. In case of the feature corresponding to structure R_l the smearing is most significant extending downwards from the left and right lower corners of the structure. The algorithm compensates for this by adjusting the resistivity of the features. The resistivity of the block R_l is underestimated by up to $680 \Omega\text{m}$ (68 %) and the ends of structure C_r (horizontal position $30 - 32 \text{ km}$ and $39 - 41 \text{ km}$) underestimate the true model by up to $5 \Omega\text{m}$ (50 %). There is very little indication of structure R_r , as it is shielded by the low-resistivity structure C_r . Structure C_l is also not well recovered. The centre of structure C_l is placed at roughly the correct depth, but the structure is greatly smeared out in the vertical direction and is too narrow in the horizontal direction. In addition to these shortcomings the model also shows a high number of small scale artefacts in the top 3 km which are most likely caused by the added noise.

An analysis of the DOI (Oldenburg and Li, 1999) (not shown) confirms that all regions of the model are supported by the data.

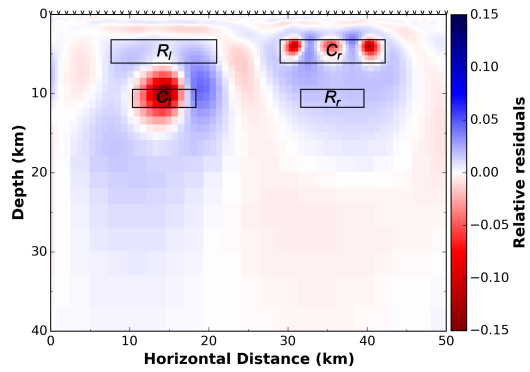
2.4.1.2 Bootstrap inversions

To perform the bootstrap analysis the original data set was resampled as described in Section 2.2.1 and 100 bootstrap representations of the data were created. All bootstrap data sets were inverted using the same model mesh and the same starting model as the master-inversion. A maximum of 30 iterations per model were performed after which the target misfits of each individual model was adjusted to allow Occam to find the smoothest solution, and each model was run for a maximum of 10 additional smoothing iterations. The average achieved misfit was $\bar{\delta} = 1.40$ (after adding 5 % smoothing buffer) and the final models had an average roughness of 17.8.

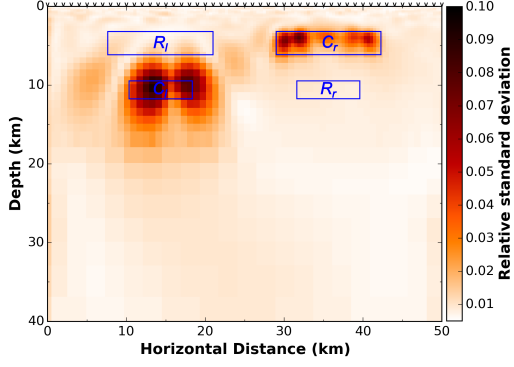
The resulting solution ensemble was analysed using Equations (2.4), (2.5) and (2.9), to calculate the uncertainty estimation maps (Figures 2.4 a–f). The average model (Figure 2.4a) is similar to the master-inversion, but



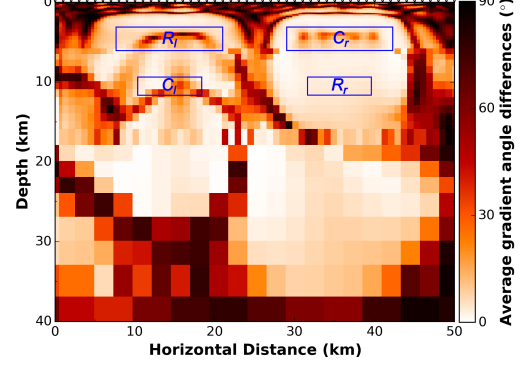
(a) Average of the models, calculated across all of the Monte Carlo bootstrap inversion runs.



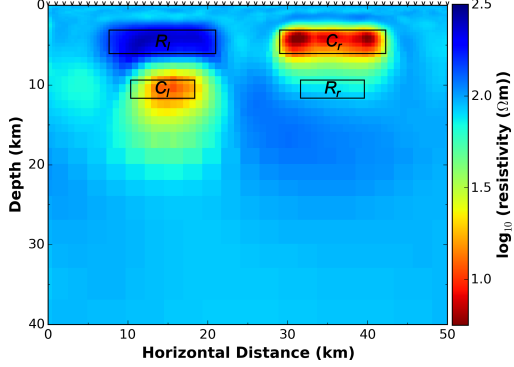
(b) Relative residuals of the master (Figure 2.3b) and the average result (Figure 2.4a), in percent of the master's cell values. Cells are red where the average result exhibits higher resistivity values than the master and blue where the average model exhibits lower resistivities.



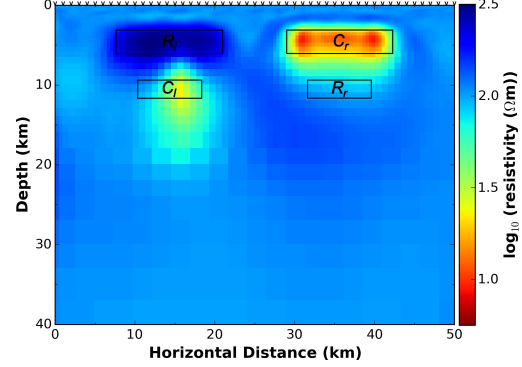
(c) Relative standard deviation of the Monte Carlo bootstrap inversion runs. Darker colours mark higher values.



(d) Average gradient angle deviations of the Monte Carlo bootstrap inversion runs. Darker colours mark higher values.



(e) Minimum cell values across all Monte Carlo bootstrap inversion runs.



(f) Maximum cell values across all Monte Carlo bootstrap inversion runs

Figure 2.4: Monte Carlo bootstrap results for the synthetic test data. Black V mark the locations of the 51 simulated recording sites. The true locations of the four anomalous bodies R_l , C_l , C_r , and R_r are marked with black/blue boxes.

exhibits some differences. These differences become evident in the map of the relative residuals between the master-result and the average bootstrap result (Figure 2.4b). The use of the relative residual as opposed to the absolute residual ensures comparability between the values for all cells.

Both models are generally very similar from a structural standpoint. The representation of feature C_r in the average model shows less extreme values than in the master-inversion, but the true resistivity is still underestimated. Comparing other model regions of the bootstrap average to the true model, it is also clear that the resistivity of structure R_l is still underestimated and the resistivity of structure C_l is overestimated. Furthermore, there is still no significant indication of structure R_r . This is not surprising as the bootstrapping models do not include or add any new information and the structure is effectively shielded by the low-resistivity feature above.

The relative standard deviation shown in Figure 2.4c is highest across the recovered low-resistivity feature corresponding to structure C_r and around the feature correlating to structure C_l . These regions coincide with the smearing effects around C_l and the regions of resistivity underestimation of structure C_r . Further areas of elevated standard deviation are extending downwards from the left and right lower corners of structure R_l , as well as various small scale artefacts in the top 3 km of the model. This indicates that these regions show the largest variations in resistivity cell values across the 100 bootstrap solutions and therefore, exhibit the largest uncertainty. The higher variability associated with conductive features rather than resistive features is caused by the higher sensitivity of the MT method to conductive features (Chave and Jones, 2012).

The deviations in gradient direction (Figure 2.4d) indicate variation in position and shape of structures. Large variations are indicated in the top 3 km of the model along the whole profile. Furthermore, variations are shown at the top of the recovered features corresponding to structures R_l and C_r , and in the middle of these features, running along the long axis, indicating the point where the gradient direction reverses over the structures. In addition to the line of gradient reversal, elevated levels of gradient deviation are indicated for the area extending down from the right corner of structure R_l and for an area extending down from a point about 2 km to the right of the lower left corner of the same structure. For structure C_l

the line of gradient direction reversal is less well defined. The model gradients also vary significantly at depths greater than 20 km, which is most likely caused by the lack of structure in those regions, so that even small differences result in large changes in gradient direction.

Some additional information about the range of possible cell values is given by the analysis of the minimum values across all bootstrap models for each cell (Figure 2.4e) and the maximum values respectively (Figure 2.4f). These maps display the extreme values for each individual cell and do not represent viable models and can therefore not be expected to achieve misfits comparable to the master-inversion. In our synthetic test case the range between minimum and maximum cell values is small. Structurally, the two plots do not differ greatly from each other or from the master and average results, and also give no real indication of the shielded structure R_r .

As the bootstrap approach is mainly sensitive to model errors caused by data noise, we performed an inversion on a control data set that has almost no noise added to it (a small noise component is added for stability purposes). By comparing the inversion result of the low noise data set with the master-inversion and calculating the residuals between the two (Figure 2.5), we can analyse which model errors were likely caused by the added noise, and not by the inversion algorithm or other influences the bootstrap method is not sensitive to. Viewing the residual map in Figure 2.5, it is apparent that the biggest differences caused by the added noise are in the areas of structure C_r and around it, structure R_l , and structure C_l , as well as under it. In addition, a variety of small scale artefacts are observable in the top 3 km of the model. Comparing the residuals with the map of the relative standard deviation, it is obvious that most of these areas are indicated as having elevated variability. The only exception is structure R_l , where the standard deviation shows little indication for increased uncertainty.

Assuming no knowledge of the true model, the combined interpretation of the calculated average model, the standard deviation and the average gradient direction differences would indicate that the various small scale features in the top 3 km are artefacts caused by data noise and that the amplitude of the resistivity values of the features correlated to the true structures C_r and C_l are subject to elevated uncertainty. Furthermore, the standard deviation map indicates that the lateral extension of the feature

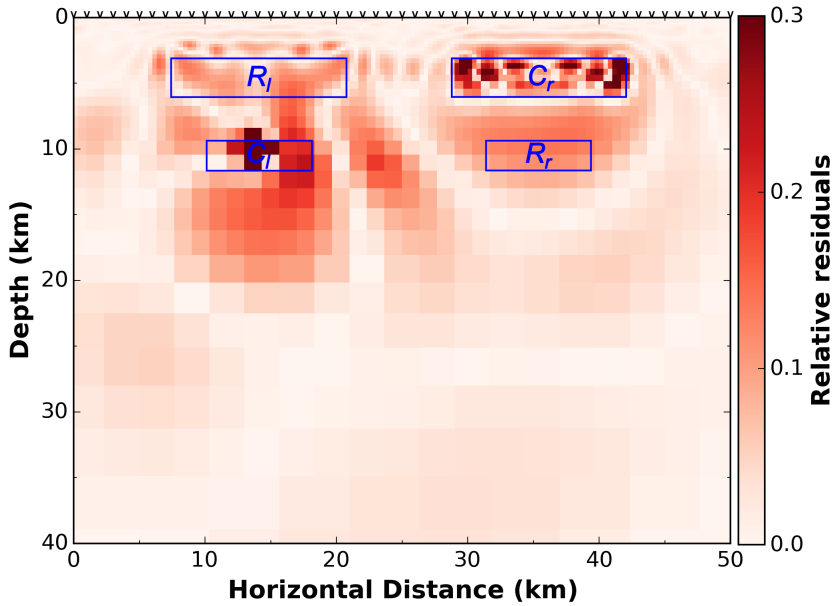


Figure 2.5: Relative residuals of the low-noise comparison run minus the master-result, in percent of the low-noise cell values (absolute values of the relative residuals shown for easier comparison with relative standard deviation map (Figure 2.4c)). Black V mark the locations of the 51 simulated recording sites. The true locations of the four anomalous bodies R_l , C_l , C_r , and R_r are marked with blue boxes.

belonging to C_l is unsure. Most other parts of the model, especially at depths of 20 km and greater, show low relative standard deviation and are rated as well determined. It has to be noted that the maximum skin depth of this set of MT data is about 50 km and there may be model regions that are not fully constrained by the data even before this depth.

2.4.2 Delamerian MT Transect

To demonstrate the application to real data we conducted a case study on a data set from the Delamerian MT transect (Figure 2.6). This data set consists of data from 68 broadband MT sites, with a sampling frequency of 1000 Hz, collected in 2010 and 2012 along the L193 AuScope 09GA-SD1 Southern Delamerian seismic line. For the 14 western-most sites the site spacing averages to about 5 km, and the 54 sites on the eastern side of the profile have a site spacing of about 1.5 km. The data cover a frequency range of 0.012–156.25 Hz, and have been corrected for a geo-electric strike of 49° west of north. The data were notch filtered for 50 Hz power line

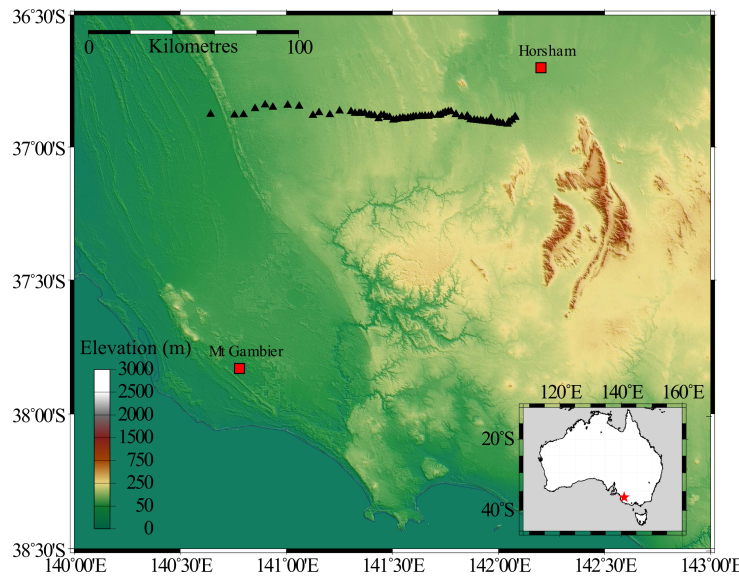


Figure 2.6: Map of the station locations of the Delamerian MT transect (\blacktriangle).

noise (including harmonics). Data blocks with phase tensor skew values of $-5^\circ > \beta > 5^\circ$ (Caldwell et al., 2004) were removed from the data set for violating the 2-D assumption. After the omission of these data points a total of 1667 data blocks remained. For a full geological interpretation see Robertson et al. (2014).

2.4.2.1 Conventional inversion

As with the synthetic data, the complete Delamerian MT transect data were inverted with the Occam 2-D code (deGroot Hedlin and Constable, 1990) to create the master-inversion (Figure 2.7). A $100\Omega\text{m}$ homogeneous half-space was used as the starting model. We used the same error floors as Robertson et al. (2014), they were set to 10 % for the phase and 20 % for the apparent resistivities. Following the definition in Section 2.4.1 this corresponds to a phase error of $\sigma_\phi \approx 2.87^\circ$. By setting the error floor of the phase lower than the error floor of the resistivities, the effects of possible static shift on the model outcome are reduced. The inversion was run for 50 iterations, plus an additional ten smoothing iterations and achieved a misfit of $\delta = 1.93$ (including 5 % smoothing buffer) and a roughness value of 217.3. These values are comparable to the values of $\delta = 1.95$ and a roughness of 197 reached by Robertson et al. (2014). The small differences are likely due to a slightly higher smoothing buffer used in Robertson et al. (2014),

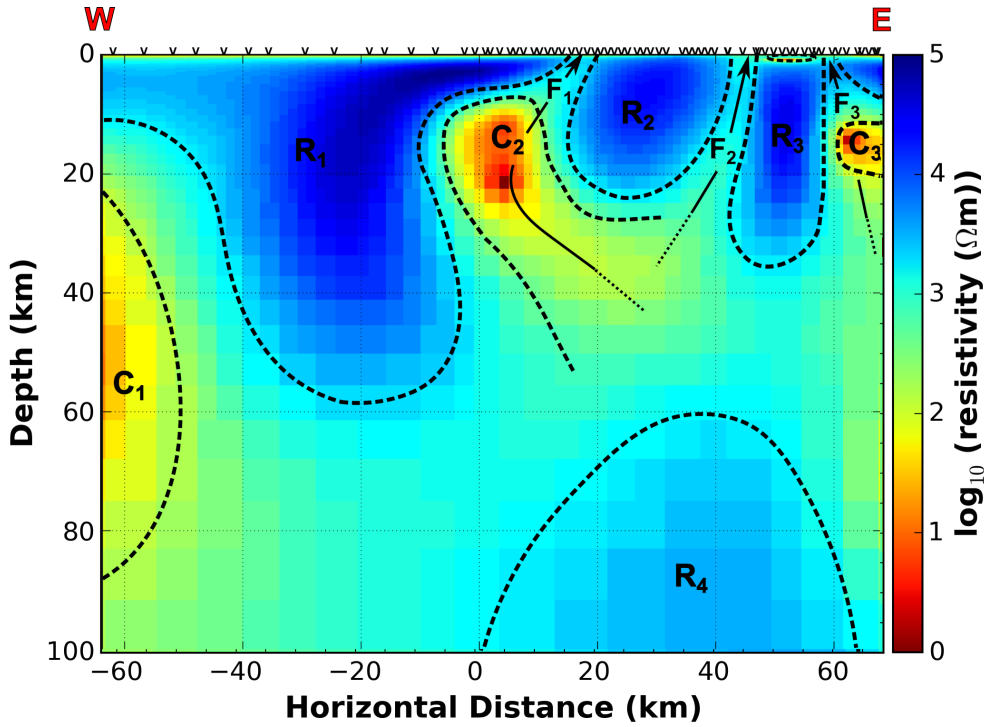


Figure 2.7: Master-inversion (original data set) of Delamerian MT Transect data set. Black \vee mark the locations of the 68 broad band MT recording sites. The interpreted locations of the model features $R_1 - R_4$ and $C_1 - C_3$ are marked by dashed lines. The interpreted fault structures $F_1 - F_3$ and their shape are marked with arrows.

which has a negligible influence on the model result, as demonstrated by the fact that the model from Robertson et al. (2014) is virtually identical to the master-result generated here.

The master-model covers a wide range of resistivity values, spanning 1–10000 Ωm , and the main features of the master-model are three low resistivity structures C_1 , C_2 and C_3 , as well as four high resistivity features R_1 , R_2 , R_3 and R_4 (Figure 2.7). Anomalies C_2 and C_3 range from 1 to 100 Ωm in resistivity, and anomaly C_1 has a minimum resistivity of about 37 Ωm . Anomaly C_1 is located at the very eastern edge of the model, connected to the model's padding cells. The data density for that area of the profile is sparse and the feature should be interpreted carefully, as it might be a boundary effect.

In addition to the main features the model shows low resistivity structures F_1 , F_2 and F_3 , marked by arrows in Figure 2.7, which were interpreted as faults serving as fluid pathways by Robertson et al. (2014).

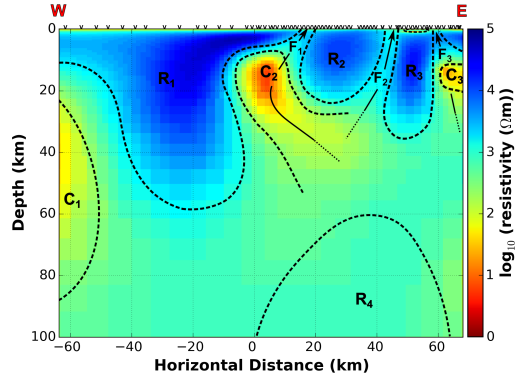
2.4.2.2 Bootstrap inversions

As with the synthetic test case, 100 resampled data sets were drawn from the original data set to perform the bootstrap analysis, using the same model mesh and starting model as the master-inversion. As with the master-inversion a maximum of 50 iterations were performed, followed by a maximum of ten smoothing iterations. The bootstrap inversion achieved misfits ranging from $\delta = 2.1$ to $\delta = 2.4$ with an average misfit of $\bar{\delta} = 2.2$ (after adding 5 % smoothing buffer). The average model roughness achieved was 186.4.

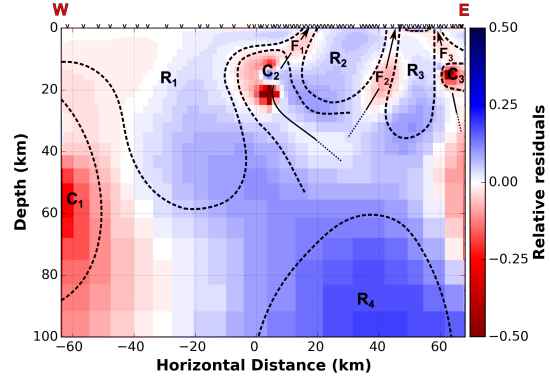
The average bootstrap model (Figure 2.8a) shows almost all of the same main features as the master-inversion, but differs in details. The average model shows a more homogeneous lower crust, that exhibits lower resistivities as is evident from the residuals between the master-model and the average model (Figure 2.8b). The high resistivity feature R_4 , which can be observed in the master-inversion is not evident in the average model. Compared to the master-result, features C_2 and C_3 show a smoother resistivity distribution and the boundary structure C_1 exhibits a higher resistivity closer to the background. Structures R_1 and R_3 extend less deep than in the master-result, which coincides with the overall reduced resistivity of the lower crust. The interpreted fault structures F_1 and F_2 are clearly evident and still show a connection going through to the surface. Most of structure F_3 is still evident in the average model, but feature R_3 seems to connect to the right boundary of the model, and the connection of F_3 to the surface is no longer clearly evident.

The map of the relative standard deviation across the bootstrap models (Figure 2.8c) shows values of more than 50 % in some regions of the model. Elevated variability is indicated for the centres of C_2 and C_3 . Other regions of elevated variability are the area around C_1 and the area under C_2 , extending downwards from the tip of R_1 .

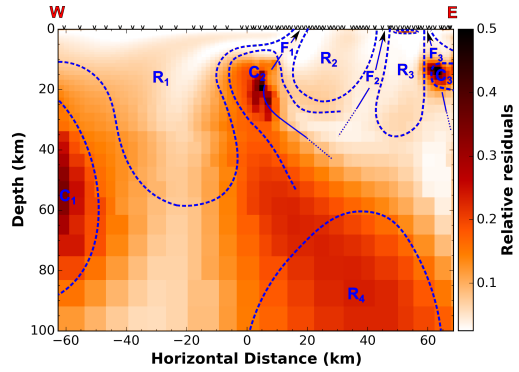
From the display of the average gradient angle differences (Figure 2.8d) we can infer the stability of position and extension of structures. Down to a depth of about 10 km the resistive structures R_1 , R_2 and R_3 show well defined and localized lines of gradient direction reversal, indicating that the position of these features is well defined in those depths. Below 10 km



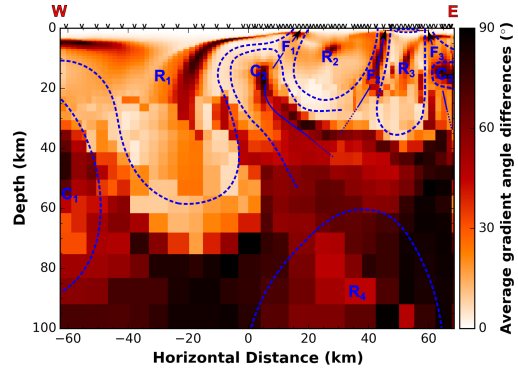
(a) Average of the models, calculated across all of the Monte Carlo bootstrap inversion runs.



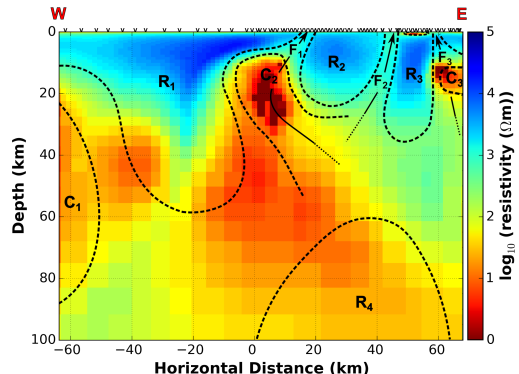
(b) Relative residuals of the master (Figure 2.7) and the average result (Figure 2.8a), in percent of the master's cell values. Cells are red where the average result exhibits higher resistivity values than the master and blue where the average model exhibits lower resistivities.



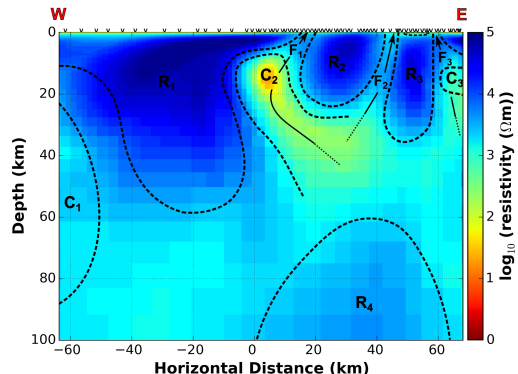
(c) Relative standard deviation of the Monte Carlo bootstrap inversion runs. Darker colours mark higher values.



(d) Average gradient angle deviations of the Monte Carlo bootstrap inversion runs. Darker colours mark higher values.



(e) Minimum cell values across all Monte Carlo bootstrap inversion runs.



(f) Maximum cell values across all Monte Carlo bootstrap inversion runs

Figure 2.8: Monte Carlo bootstrap results for the Delamerian MT transect data, derived from inversions performed on 100 bootstrap realisations of the original data. Black V mark the locations of the MT recording sites. The model features $R_1 - R_4$ and $C_1 - C_3$ are marked by dashed lines. Arrows mark the interpreted fault structures $F_1 - F_3$.

the points of gradient reversal are less well defined indicating a degree of uncertainty in the position of these structures. The line of gradient direction reversal of R_3 cuts across the indicated fault F_3 and extends all the way to the boundary of the model. A similar behaviour can be observed for F_1 , which is intersected by the line of gradient direction reversal of R_1 , but in this case F_1 is not cut off completely. Apart from that, F_1 shows low levels of gradient angle differences, indicating its position is well determined. This is not the case for F_2 , which shows elevated gradient angle differences, denoting elevated uncertainty in the position of this fault. Other areas of significant gradient angle differences are structure C_1 , the entire western side of the model from a depth of about 70 km down, and the whole eastern side of the model from a depth of about 40 km downwards. This eastern area of elevated gradient angle differences also extends along C_2 , marking a poorly defined line of gradient direction reversal for this feature, and along the right flank of the resistive structure R_1 , extending up to a depth of about 20 km. In contrast, the position of the lower edge and the left flank of R_1 and the lower edges of R_2 and R_3 seem well defined.

The high uncertainty in the position and extent of R_1 and C_2 is also evident in the display of the lowest and highest cell values reached across all bootstrap models (Figures 2.8e and 2.8f). The two maps show large differences. Most main features are still evident in both maps, except for boundary feature C_1 , which is no longer distinguishable from the background in the display of the maximum reached resistivity values. The fault structures are still visible in both maps, except for the fact that the fault feature F_3 is not connected to the surface in the maximum value display. Apart from these features, the biggest differences evident between the minimum and maximum value displays are the areas between and under R_1 and C_2 . In the minimum resistivities map, the main body of R_1 extends to a depth of only 20–30 km and a large low resistivity region is present under R_1 and C_2 that extends from 25 km downwards. On the maximum resistivities map R_1 is notably wider and extends into the area of the western side of C_2 .

Taking into account the additional information from the bootstrap analysis, the master-model can be reinterpreted (Figure 2.9). The bootstrap results show indications that the existence of features C_1 and R_4 is very uncertain and there is a high probability that they are artefacts. Most other features

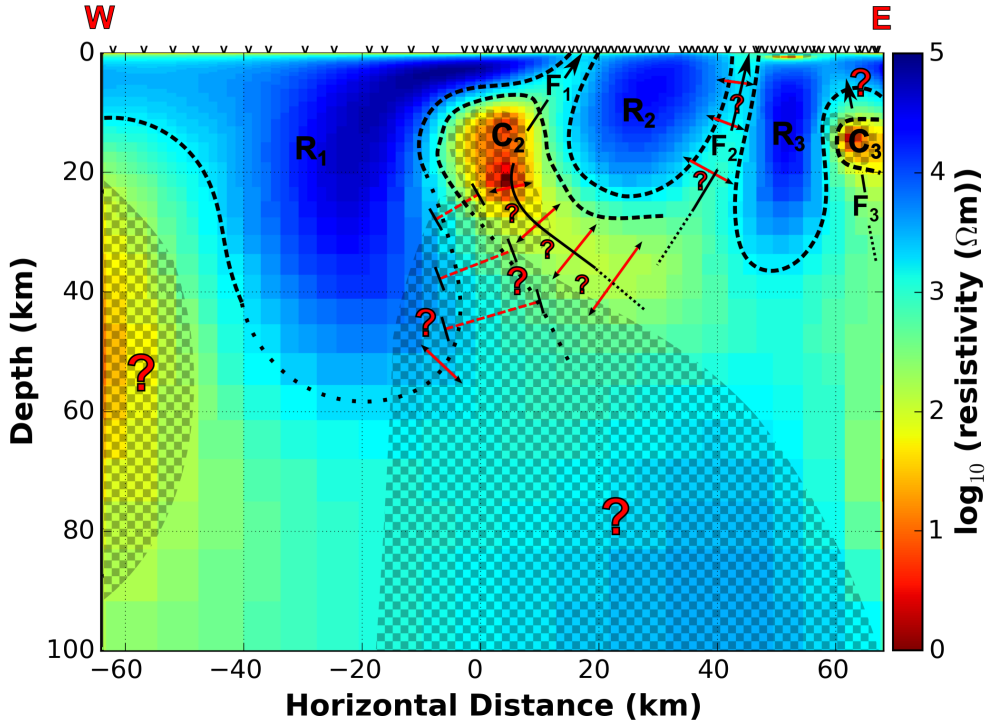


Figure 2.9: Reinterpretation of the master-model for the Delamerian MT transect data, taking into consideration the bootstrap results. Black \checkmark mark the locations of the 68 broad band MT recording sites. The interpreted locations of the model features R_1-R_3 and C_2-C_3 are marked by black dashed lines. Dotted borders mark parts of feature edges that are not well determined. The interpreted fault structures F_1-F_3 and their shape are marked with black arrows. Red arrows (\leftrightarrow) mark uncertainty in the location of a feature and red bars ($-[-]$) mark uncertainty of the width of a model feature or area. Areas overlain with a checker pattern have high uncertainty in the amplitude of the cell resistivity values and red question marks (?) are general markers for areas of uncertainty.

show a high degree of robustness. Only the extension of fault structure F_3 to the surface is subject to high uncertainty. The area between and under R_1 and C_2 is also not well determined, especially the transition between the two features and the downwards extension of R_1 are uncertain, in position as well as absolute resistivity value. Furthermore, features C_2 and C_3 are likely to have a smoother resistivity distribution than indicated by the master-model, with less extreme values towards low resistivities.

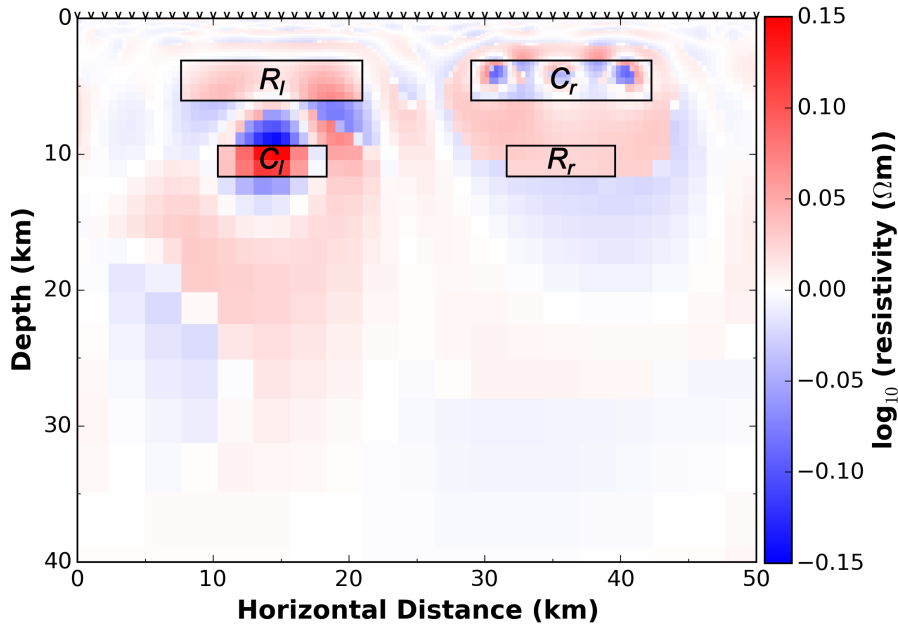


Figure 2.10: Differences between the residuals of the bootstrap average and the true model and the residuals of the master-model with the true model. Blue colours mark areas were the average bootstrap solution is closer to the true model than the master-inversion, red colours mark areas were the master-result is closer to the true model. Black V mark the locations of the 51 simulated recording sites. The true locations of the four anomalous bodies R_l , C_l , C_r , and R_r are marked with black boxes.

2.5 Discussion

Our bootstrapping method for the appraisal of inversion models yields estimates for a variety of different parameters. The standard bootstrapping result-package consists of the calculated average model, the residuals between average model and master-result, the relative standard deviation, the gradient angle differences, and the minimum and maximum cell values. These should all be interpreted together, when analysing the results of the bootstrap process to ensure that the correct conclusions are drawn.

Tests with a synthetic model show that the average bootstrap model exhibits less artefacts compared to the master-inversion, and that it is closer to the true model regarding the actual cell values for most parts of the model, as indicated by the blue regions in Figure 2.10, which compares the residuals between true model and the master-solution to the residuals between the true model and the average bootstrap model for the synthetic case. However, the average model is not an improvement over the master-

result in all regions of the model, as indicated by the red model regions. The average model can be used to infer the quality of the master-inversion with regards to location and gradient distribution of structures, but has to be treated carefully when assessing the magnitude of the model parameters as it is not unambiguous.

We interpret the average model as being a more realistic representation. This is also apparent for the real world example, as the average model shows less artefacts and less model cells with unrealistically extreme parameter values.

The most important indicators for the model uncertainty are the relative standard deviation and the average gradient angle differences maps, which allow for the identification of model areas with elevated variability. The standard deviation maps are especially sensitive to variations in absolute resistivity values, whereas the gradient angle difference maps indicate variations in structure shape and position; particularly by indicating the points of gradient direction reversal. Localised and well defined lines of gradient reversal are an indication for little variation, and therefore little uncertainty in the position of a structure. They are especially useful in the assessment of fault structures, as demonstrated in the analysis of the Delamerian data set.

Zones of low gradient angle differences around structures that are common to most model representations mark the minimum extend of a feature. The gradient angle differences have to be interpreted with care if they occur in large regions of uniform resistivity distribution, especially if they coincide with low standard deviation values of the cell parameters: areas with no structure cause even small cell value differences to result in large changes in gradient direction, which could be mistaken for high uncertainty. A weighting of the angle differences by the average gradient amplitude can correct for this, but would greatly complicate the interpretation.

The magnitude of the standard deviation does not necessarily indicate the magnitude of the error of the model cell value, but the areas of increased standard deviation are an indicator for the location of areas with increased uncertainty in the amplitude of the cell value. A DOI study should be performed before interpreting the bootstrapping results to avoid wrongly

identifying model regions, that the data is not sensitive to, as well determined.

In addition to the uncertainty estimates, valuable extra information is provided by mapping the extremal values of each model cell. The bootstrap method supplies only very limited information about the non-uniqueness of the model, but these plots give an important insight into the range of values that can be reached and can indicate the minimal/maximal feasible extent of an anomaly. The value of these plots is very evident in the analysis of the Delamerian MT transect data, as they highlighted areas of high uncertainty in the lower crust and give an indication of the variability of the location and extent of major anomalies. It is important to note that these maps represent the most extreme values reached by each individual cell across all bootstrap realisations. These maps do not represent feasible models and would not fit the data to the same level as the optimal model. Extremal models, which fit the data to a similar level as the optimal solution, are for example provided by the most-squares method (Jackson, 1976; Meju and Hutton, 1992; Kalscheuer et al., 2010; Rosas-Carbaljal et al., 2014).

Both MCMC methods (Metropolis and Ulam, 1949; Tarits et al., 1994; Gamerman, 1997; Chen et al., 2012; Rosas-Carbaljal et al., 2014) and bootstrapping create solutions ensembles and assess posterior distributions. MCMC methods comprehensively sample the solution space and hence, can use Bayesian statistics (Gelman et al., 2003; Aster et al., 2012) to gain a more complete estimate of the posterior probability density function of the model parameters and yield quantitative uncertainty estimates. On the other hand, the bootstrap approach samples the solution space less exhaustively and provides only qualitative uncertainty estimates, but is computationally more efficient. The easier implementation of the bootstrap method is also an advantage over both the MCM analysis (Meju, 1994; Alumbaugh and Newman, 2000; Tarantola, 2005; Menke, 2012) and the MRM analysis (Jackson, 1972; Meju, 1994; Ramirez et al., 1995; Alumbaugh and Newman, 2000; Menke, 2012).

The commonly used manual model perturbation technique (Becken et al., 2008; Thiel and Heinson, 2010) is attractive in its simplicity, but only investigates how model perturbations influence the model response, which is also a drawback of the analysis of the sensitivity matrix (Thiel and Heinson,

2010), and the null-space projection method (Deal and Nolet, 1996; Rowbotham and Pratt, 1997; Muñoz and Rath, 2006). Bootstrap resampling requires the calculation of more models, but is otherwise comparatively simple to implement as the model perturbation method, and has the advantage of providing direct information about how data perturbations map into the model.

In this paper we have presented conclusions from bootstrap runs with 100 resampled data sets each, but tests show that as few as 20 bootstrap models are enough to draw preliminary conclusions. We recommend the use of at least 30–50 model to achieve robust results.

In various forms the bootstrap approach makes a qualitative statement about the uncertainty of a model. This is valuable information, as the only measure of model quality provided by commonly used algorithms like Occam (deGroot Hedlin and Constable, 1990) is usually a single scale value. Furthermore, the bootstrap method can provide this information without requiring access to the inversion algorithm’s source code and without additional code development.

The approach is designed to provide increased uncertainty estimation capabilities to existing inversion algorithms. The bootstrapping approach does not require any additional assumptions. However, the results are affected by the assumptions required by the inversion algorithm. It has to be kept in mind that the uncertainty estimates are always biased by the respective inversion setup and the exact representations of the uncertainties will vary with the inversion parameters. Influencing parameters will be the used inversion scheme, such as forms of Newton’s method or nonlinear conjugate gradient methods, as well as the inversion parameters, such as smoothing operators and the modelling mesh. However, the qualitative result are expected to remain the same. Nevertheless, this should be verified with synthetic tests for each new inversion algorithm before the approach is used on real data.

We used the approach with the Occam 2-D inversion code as it is widely used and an accepted reference. Tests showed that excessive smoothing greatly reduces the variability in the solution ensemble, leading to very low uncertainty estimates. Also different starting models can influence the

magnitude of the estimates. As for most inversion approaches, the ideal parameter configurations have to be identified through tests before the main inversion.

The approach requires the calculation of several tens of inversion models, but by calculating all models in parallel, the increased computational cost is dispersed. Hence, for 2-D inversions, the execution is only marginally more time consuming than for a single inversion.

The bootstrap approach appears to be working better on the real world example than on the synthetic test model. This can not be verified as we do not know the true model underlying the Delamerian transect data, and might be a misinterpretation. It could be due to higher data noise levels in the real world data, which in turn cause more variability in the bootstrap models. Another possible cause is that the simulated noise in the synthetic example may not exactly replicate the effects of real world noise. As is common practice, we used white noise for the synthetic data, but the noise on real world MT data can be more complex and might not always be normally distributed (Garth and Poor, 1994; Manoj and Nagarajan, 2003). Bootstrap resampling may be more effective on data with real world noise. The second stage of the resampling process would need to be adjusted in cases where the noise model deviates considerably from the normal distributed noise assumed here. One such example would be spatially correlated noise. Situations like that might also require larger number of bootstrap samples to achieve reliable estimates. These questions require further research.

2.6 Conclusion

We have presented an uncertainty estimation approach for inversion modelling of 2-D MT data sets based on bootstrap resampling. We have demonstrated its effectiveness in detecting noise-induced uncertainty by testing it on synthetic and real data examples. The approach is suited for qualitative estimation of errors introduced into the model by data noise and for the analysis of model feature robustness. The method can generally be used with any available inversion algorithm, as it does not require access

to the inversion algorithm's source code, and it is easy to implement. It is therefore a viable tool for model uncertainty estimation.

Acknowledgments

The work has been supported by the Deep Exploration Technologies Co-operative Research Centre whose activities are funded by the Australian Government's Cooperative Research Centre Programme. This is DET CRC Document 2014/607.

We also thank Kate Robertson, the Geological Survey of Victoria and the University of Adelaide for providing us with the Delamerian MT Transect data, and thank Lars Krieger for his technical advice.

CHAPTER
THREE

A NOVEL APPROACH TO PARETO-OPTIMAL
JOINT INVERSION MODELLING AND DATA SET
COMPATIBILITY ANALYSIS OF GEOPHYSICAL
DATA

SEBASTIAN SCHNAIDT^{1,2}, LARS KRIEGER² AND GRAHAM HEINSON²

¹Deep Exploration Technologies Cooperative Research Centre,
Adelaide Airport SA 5950, Australia

²Electrical Earth Imaging Group, Department of Earth Sciences,
School of Physical Sciences, University of Adelaide, Adelaide SA 5005, Australia

Statement of Authorship

Title of Paper	A Novel Approach to Pareto-optimal Joint Inversion Modelling and Data Set Compatibility Analysis of Geophysical Data
Publication Status	<input type="radio"/> Published, <input type="radio"/> Accepted for Publication, <input type="radio"/> Submitted for Publication, <input checked="" type="radio"/> Publication style
Publication Details	Schnaidt, S., Krieger, L., and Heinson, G. (2015). A novel approach to pareto-optimal joint inversion modelling and data set compatibility analysis of geophysical data.

Author Contributions

By signing the Statement of Authorship, each author certifies that their stated contribution to the publication is accurate and that permission is granted for the publication to be included in the candidate's thesis.

Name of Principal Author (Candidate)	Sebastian Schnaidt
Contribution to the Paper	Developed code and method, designed and performed feasibility study, wrote manuscript, and acted as corresponding author
Signature	Date 2015-09-11

Name of Co-Author	Lars Krieger
Contribution to the Paper	Assisted in design of feasibility study and code, and provided critical manuscript evaluation
Signature	Date 29.08.2015

Name of Co-Author	Graham Heinson
Contribution to the Paper	Supervised development of work and provided manuscript evaluation
Signature	Date 8/9/15

Name of Co-Author	N/A
Contribution to the Paper	N/A
Signature	Date

SUMMARY

In the process of modelling geophysical properties, jointly inverting different data sets can greatly improve model results, provided that the data are compatible, i.e. sensitive to similar features. Such a joint inversion requires a relationship between the different data sets, which can either be of analytical or structural nature. Classically, the joint problem is expressed as a scalar objective function that combines the misfit functions of all involved data and a joint term accounting for the assumed connection between the data. This approach suffers from two major disadvantages: firstly, it can be difficult to assess the compatibility of the data sets, which, if misjudged, can lead to incorrect model results; and secondly, by aggregating all misfit terms a weighting of the data sets is enforced. We present a Pareto-optimal multi-objective joint inversion approach based on an advanced genetic algorithm. The algorithm treats each data set as a separate objective, avoiding forced weighting and generating curves of the trade-off between the different objectives. The shape and evolution of these curves are analysed to evaluate the compatibility of the used data. Furthermore, the statistical analysis of the generated solution population provides valuable model uncertainty estimates.

3.1 Introduction

Geophysical models can benefit greatly from the combined inversion of multiple data sets. Different methods are sensitive to different petrophysical parameters and different parts of the subsurface, and they usually have uncorrelated noise components. Even the use of multiple data sets from the same method can be beneficial, as the noise components of data sets collected at different times are also likely to be uncorrelated. Thus, the additional information available for the inversion will improve the quality of the resulting model by reducing solution non-uniqueness (Muñoz and Rath, 2006), which is commonly present in geophysical modelling. Standard joint inversion approaches are generally used for data that are sensitive to the same petrophysical parameter, such as resistivity (Yang and Tong, 1988; Abubakar et al., 2011) and seismic velocities (Julià et al., 2000), or methods that are sensitive to different physical parameters, but have a petrophysical or structural connection (Gallardo and Meju, 2003, 2007; Commer and Newman, 2009; Jegen et al., 2009; Moorkamp et al., 2011).

The classical approach to the joint inversion problem is based on a scalar objective function that combines misfit measures for all data sets and also includes a joint term that connects the different data sets (Haber and Oldenburg, 1997; De Stefano et al., 2011). Weighting has to be employed to aggregate all misfits into a joint objective function. Data sets can either be weighted equally (Dobróka et al., 1991; De Nardis et al., 2005) or individual weights have to be selected (Julià et al., 2000; Mota and Monteiro dos Santos, 2006). There is no standard way of defining these weights, which vary between problems (Treitel and Lines, 1999), and the choice of inappropriate weights can lead to bias in the results (De Stefano et al., 2011).

The use of a combined objective function also makes it difficult to judge the compatibility of the involved data sets: it is important to determine if data sets are sensitive to similar features, and if the assumed relationship between the data sets is valid. Forcing incompatible data sets into a joint model may yield a model that is worse than the corresponding single data set models, as an inversion algorithm will produce unnecessary artefacts trying to compensate for an underlying incompatibility, as we demonstrate in a later example.

An alternative to the conventional approaches are so called multi-objective optimisation methods, particularly multi-objective evolutionary algorithms (MOEAs), which mimic natural evolution processes (Holland, 1975). Multi-objective optimisation algorithms treat each data set as a separate objective rather than aggregating them into a single objective function, which avoids forced weighting. This leads to the creation of data set trade-off surfaces, which allow inference of the compatibility of different data sets. These methods are global optimisation approaches (Sen and Stoffa, 2013) and perform direct searches (Lewis et al., 2000). Hence, these methods do not require any linearisation approximations or gradient information. They also create an ensemble of solutions rather than a single best fit result, which has the added advantage that the solution ensemble can be evaluated to infer qualitative estimates of model uncertainty.

MOEAs have great potential to solve pressing problems in modelling and they are regularly used in a wide range of disciplines, such as engineering, computer sciences and finance (for a list of applications see e.g. Coello Coello et al., 2007; Zhou et al., 2011). However, they have been widely neglected in the geophysics modelling community. Kozlovskaya et al. (2007) compared conventional and multi-objective methods for seismic anisotropy investigations, and used a neighbourhood algorithm (Sambridge, 1999a,b) rather than an evolutionary algorithm. The only applications of MOEAs in geophysics to date are by Moorkamp et al. (2007, 2010). They used the MOEA NSGA-II (Deb et al., 2002b) to jointly invert teleseismic receiver functions and magnetotelluric data (Moorkamp et al., 2007), as well as receiver functions, surface wave dispersion curves, and magnetotelluric data (Moorkamp et al., 2010). They had a first look at how MOEAs can be used for geophysical modelling, and how they may assist in judging data compatibility. However, their approach to judging data compatibility from the shape of the trade-off surfaces was based on a mostly visual analysis of the trade-off plots.

We present the multi-objective joint optimisation algorithm (MOJO), which is based on the “Borg” multi-objective evolutionary algorithm by Hadka and Reed (2013). MOJO was developed to measure data set compatibility in a quantifiable way, so that a visual inspection of the trade-off plots is usually not required. We will first introduce the algorithm in detail and

show how the solution ensemble can be used to generate reliable models. We will then demonstrate the functionality of our data set compatibility measure in synthetic model tests and evaluate influences of data noise and data error estimates.

3.2 Theory

3.2.1 Definition of multi-dimensional Pareto-optimality

Objectives based on different geophysical data sets will always be conflicting objectives, as even measurements with the same method, at the same location will sense slightly different geophysical rock properties. Hence, there exists no single solution that can simultaneously optimise all objectives. In combination with solution non-uniqueness, this is the reason that conventional approaches which search for a single best fit solution to a joint-inversion problem produce biased results. When dealing with multiple conflicting objectives it is impossible to define a single best solution without introducing explicit or implicit weighting of the objectives.

Nevertheless, to solve an optimisation problem, solutions have to be rated, to enable search progression. Therefore, a new way to define optimality has to be employed in order to mitigate this problem. In the field of multi-objective optimisation the most widely used concept to rate solution quality is that of *Pareto-optimality*, which was first introduced by Edgeworth (1881) and Pareto (1896). A set of solution is considered Pareto-optimal if there is no other feasible solution that can improve on an objective value without deteriorating any other objective values, and the entirety of solutions fulfilling this criterion are called the *Pareto-optimal set*. When the Pareto-optimal set is projected onto a surface it is referred to as the *Pareto-front*, which composes a trade-off surface between the different objectives (Figure 3.1).

The objective value vectors of the Pareto-optimal solutions are *Pareto-non-dominated*. For a minimisation problem with N objectives, the objective vector $\mathbf{x}^* = (x_1^*, x_2^*, \dots, x_N^*)$, containing the N objective function

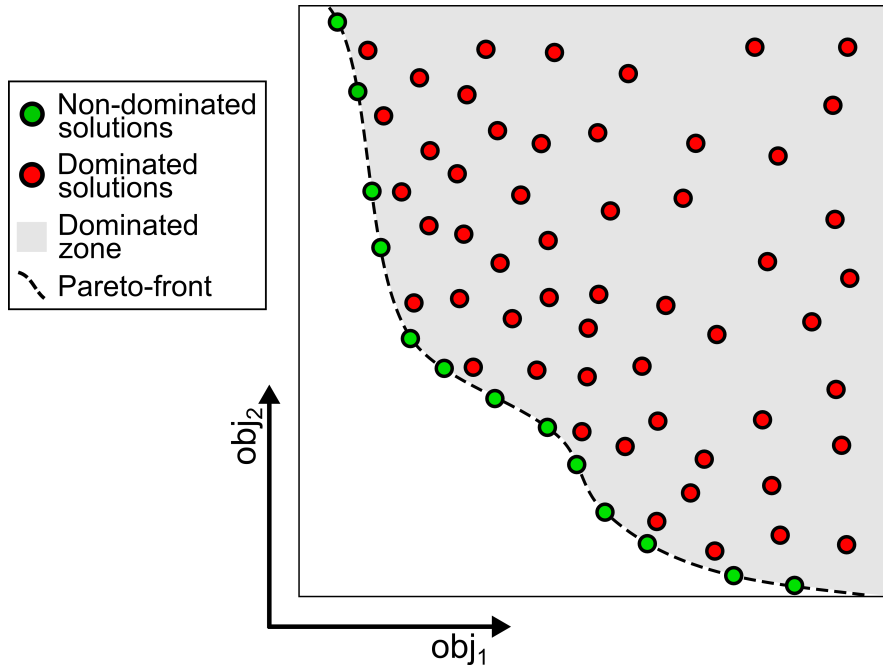


Figure 3.1: Illustration of Pareto-dominance using the example of a two objective minimisation problem. The green dots symbolise non-dominated solutions, red dots mark dominated solutions, which are located in the dominated zone (grey background). The dashed line marks the Pareto-front.

values for a given solution, is defined to Pareto-dominate another vector $\mathbf{x} = (x_1, x_2, \dots, x_N)$ if and only if:

$$x_i^* \leq x_i \quad \forall i \in \{1, 2, \dots, N\} \quad \wedge \quad \exists j \in \{1, 2, \dots, N\} : x_j^* < x_j, \quad (3.1)$$

which is denoted by $\mathbf{x}^* \prec_p \mathbf{x}$ (e.g. Coello Coello et al., 2007, p. 10-11).

All non-dominated solutions are rated as optimal and equally good. This rating of the solutions using Pareto-efficiency allows for solving of the optimisation problem free of weighting biases.

3.2.2 The Multi-objective Joint Optimisation Algorithm

MOJO is a stochastic method, which yields an ensemble of model solutions to an inversion problem. It is based on the auto-adaptive “Borg” Multi-objective Evolutionary Algorithm (Hadka and Reed, 2013). The following explanation of the “Borg” algorithm is mainly adapted from (Hadka and Reed, 2013), which should be referred to for more in-depth information.

We will concentrate on the main features of the “Borg” algorithm, for additional information on the basics of MOEAs and alternative approaches we refer the reader to (Coello Coello et al., 2007).

We chose the “Borg” algorithm, as it is a state-of-the-art MOEA capable of automatically adapting to varying problems. “Borg” was shown to outperform its competitors on a variety of test problems, particularly on problems with many objectives (Hadka and Reed, 2012, 2013). This is of high importance, as many MOEAs generally deteriorate in performance for more than three objectives (Ishibuchi et al., 2008; Zhou et al., 2011), whereas we are expecting to regularly run problems in excess of three objectives. “Borg” has displayed good convergence and produces a final solution ensemble with high solution diversity, which is necessary to infer model ranges and generate reliable information on the compatibility of different objectives.

“Borg” shares a lot of its basic functionality with many other evolutionary algorithms, as it is a metaheuristic optimisation algorithm that simulates the process of natural evolution. More specifically it is based on a genetic algorithm (De Jong, 1975; Goldberg, 1989). Candidate solutions are treated as members of a population and are undergoing recombination, mutation, and selection to produce new candidate solutions, progressing the search. Based on the theory of Holland (1975) the population members are often expressed as binary strings, but they can also be expressed as real-valued arrays. In our approach we express the population members as real-coded arrays, as it is a more direct representation of the parameter values occurring in geophysical modelling.

Evolutionary algorithms are direct search methods, that is derivative-free algorithms that do not require any information about the gradient of the objective function(s). This simplifies the implementation, at the expense of the algorithms computing efficiency. These methods require significantly more function evaluations than conventional inversion algorithms, but parallelisation of codes is often possible and enhanced computing power is readily available. The stochastic component inherent in evolutionary algorithms makes them very robust against local minima.

The process of MOJO is illustrated in Figure 3.2. It begins by initialising a starting population with random parameters inside predetermined parameter thresholds. All member solutions of the population are then evaluated against the measured data and objective values are calculated for every objective. This is followed by an evaluation of the domination status of each solution. The objective values are usually expressed as root mean square deviations δ , the misfit of the forward calculated response of a set of model parameters \mathbf{m} to a set of n observed data points \mathbf{d} , normalised by the errors of the observed data points σ_d :

$$\delta = \sqrt{\frac{1}{n} \sum_{i=0}^n \left(\frac{d_i - F(\mathbf{m})_i}{\sigma_{d_i}} \right)^2}. \quad (3.2)$$

The algorithm also allows the user to set misfit constraints, which effectively limit the feasible region of the objective space. Solutions outside the feasible region are treated as invalid.

In addition to the misfit functions, a regularisation measure has to be defined to stabilise the inversion. The actual implementation depends on the model parameters and geometries.

New population members are created via recombination operators after the solutions are evaluated and their domination status is determined. The solutions to be used for recombination are chosen via tournament selection (Miller and Goldberg, 1995), where randomly picked population members compete against each other.

There are a variety of different recombination operators available, but usually only one is implemented in a given algorithm. Different kinds of operators have different degrees of effectiveness, depending on the type and nature of each individual optimisation problem. This led to the proposal of adaptive operators to be employed (Vrugt and Robinson, 2007; Vrugt et al., 2009), a concept that has been embraced in the “Borg” algorithm. “Borg” can choose from six different operators: simulated binary crossover (Deb and Agarwal, 1994), differential evolution (Storn and Price, 1997), parent-centric recombination (Deb et al., 2002a), unimodal normal distribution crossover (Kita et al., 1999; Deb et al., 2002a), simplex crossover (Tsutsui et al., 1999; Higuchi et al., 2000), and uniform mutation (Syswerda, 1989).

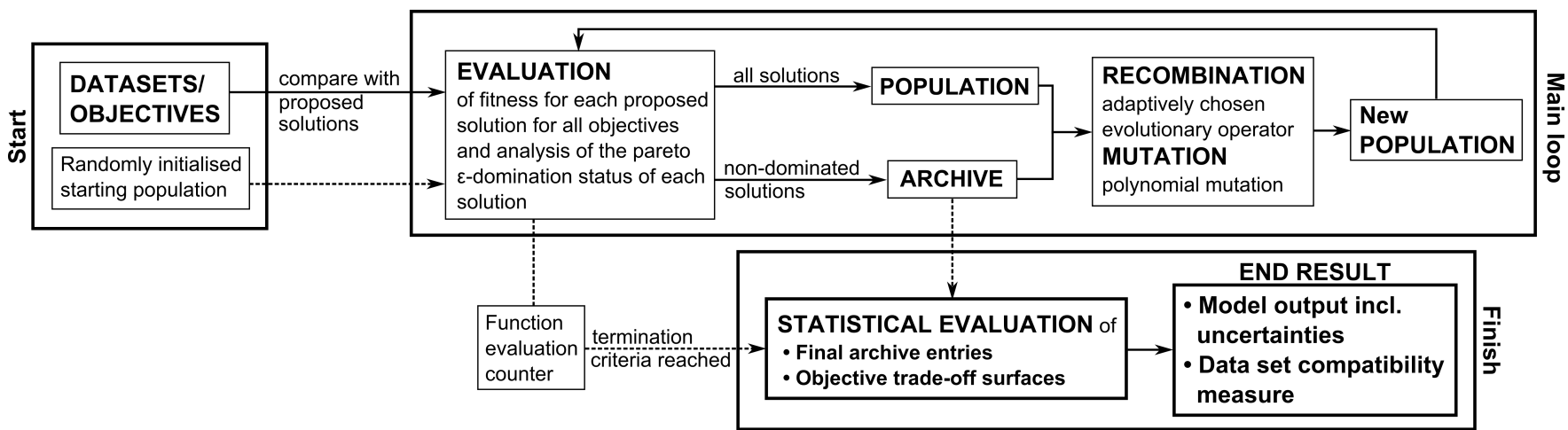


Figure 3.2: Flowchart of the MOJO algorithms functionality.

The algorithm analyses which operator produces the best solutions and adapts the probability for a given operator to be used accordingly. New solutions produced by all recombination operators, except for the uniform mutation operator, are subjected to polynomial mutation (Deb and Goyal, 1996). The mutation operators randomly mutate a given parameter of a solution and add a stochastic component to the search, ensuring better search space exploration and robustness of the search against getting trapped in local minima.

The new population produced by the recombination and mutation process is then evaluated and this loop is repeated until a termination criterion, usually a maximum number of solution evaluations, is reached.

It is important to retain optimal solutions during the search to ensure optimisation success and convergence of the search (Zitzler, 1999; Zitzler et al., 2000). “Borg” exercises this so-called *elitism* by keeping an archive of the non-dominated solutions. When using Pareto-efficiency as the optimality criterion for a multi-objective optimisation approach one has to ensure that the calculated Pareto-front is as complete and as close to the real Pareto-front as possible. As population and archive cannot be of infinite size, a MOEA will eventually be forced to eliminate solutions even though they might be non-dominated, which is known as deterioration of the Pareto-front (Hanne, 1999). Preventing the Pareto-front from deteriorating requires active diversity management (Purshouse and Fleming, 2007), which earlier MOEAs lack. “Borg” employs a modified version of ε -dominance (Hanne, 1999; Laumanns et al., 2002) to ensure solution diversity, as used in the algorithms ε -MOEA (Deb et al., 2003) and ε -NSGA-II (Kollat and Reed, 2007).

The N -dimensional objective space is discretised by dividing it into hyperrectangles (Coxeter, 1973) with side lengths $\varepsilon > 0$. Using the notation $\left\lfloor \frac{\mathbf{x}}{\varepsilon} \right\rfloor = \left(\left\lfloor \frac{x_1}{\varepsilon} \right\rfloor, \left\lfloor \frac{x_2}{\varepsilon} \right\rfloor, \dots, \left\lfloor \frac{x_N}{\varepsilon} \right\rfloor \right)$ ($\lfloor \cdot \rfloor$ denotes the floor function) for a ε -box index vector for an N -objective problem, dominance (Equation (3.1)) is redefined as discrete ε -box dominance.

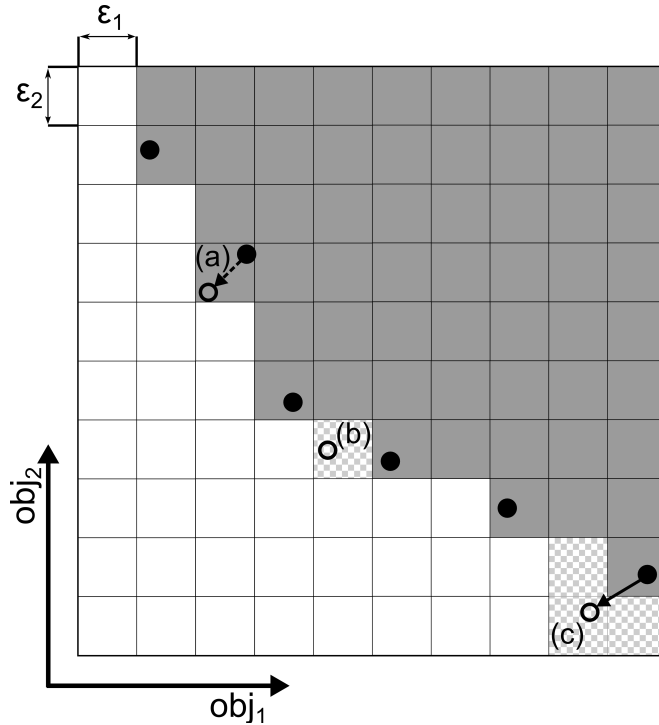


Figure 3.3: Illustration of ε -dominance and ε -progress for a hypothetical two objective case. •-symbols mark existing archive members, o-symbols mark solutions that are newly added to the archive, and grey ε -boxes mark the area dominated by the existing archive members. Solutions (a) and (c) will replace existing archive members, solutions (b) and (c) also satisfy the conditions for ε -progress and the ε -boxes marked with a chequerboard pattern are newly dominated. Modified from (Hadka and Reed, 2013).

An objective vector $\mathbf{x}^* = (x_1^*, x_2^*, \dots, x_N^*)$ is defined to ε -box dominate a vector $\mathbf{x} = (x_1, x_2, \dots, x_N)$ if and only if one of the following equivalent conditions holds:

$$\left\lfloor \frac{\mathbf{x}^*}{\varepsilon} \right\rfloor \prec_p \left\lfloor \frac{\mathbf{x}}{\varepsilon} \right\rfloor, \text{ or} \quad (3.3a)$$

$$\left\lfloor \frac{\mathbf{x}^*}{\varepsilon} \right\rfloor = \left\lfloor \frac{\mathbf{x}}{\varepsilon} \right\rfloor \wedge \left\| \mathbf{x}^* - \varepsilon \left\lfloor \frac{\mathbf{x}^*}{\varepsilon} \right\rfloor \right\| < \left\| \mathbf{x} - \varepsilon \left\lfloor \frac{\mathbf{x}}{\varepsilon} \right\rfloor \right\|, \quad (3.3b)$$

which is denoted by $\mathbf{x}^* \prec_\varepsilon \mathbf{x}$ (after Hadka and Reed, 2013). The algorithm also allows for individual $\varepsilon_i > 0 \forall i, i = \{1, \dots, N\}$ to be assigned for each objective.

Only one solution per ε -box is added to the archive. If a new solution is found that ε -box dominates another solution in the same ε -box, the former solution will be replaced with the new one (Figure 3.3).

The ε -box criterion is also used to monitor search progress. So-called ε -progress is achieved if a new-found solution not only ε -dominates at least one existing archive entry, but is also located in a previously unoccupied ε -box. ε -progress is checked sporadically and search restarts will be triggered if search stagnation is detected. If a restart is triggered, the size of the main population is adjusted in relation to the current archive size, according to a predetermined population-to-archive ratio and the population is purged and refilled with new solutions. These new solutions are generally made up of (mutated) archive entries or new randomly initialised solutions. For more detailed information about the restart procedure refer to (Hadka and Reed, 2013, p. 238–240). Maintaining a constant population-to-archive ratio can assist in the avoidance of local minima (Tang et al., 2006). This constant ratio also means that the ε -values limit the archive and population sizes and the ε -values can be chosen to control these.

We have adapted the “Borg” algorithm to jointly optimise multiple geo-physical data sets, such as electromagnetic data, resistivity well-logs, and seismic constraints. We have added modules for the statistical evaluation of the resulting solution ensembles of the final archive and intermediate archives, to calculate model statistics and uncertainties, and to determine data compatibility. In the following sections we will discuss in detail how we analyse the solutions and how we gauge objective compatibility.

3.2.3 Solution ensemble appraisal

The $n_{\text{arch.}}$ solutions contained in the final archive represent the full range of Pareto-optimal solutions found by the algorithm before the termination criterion was reached. This final solution ensemble can be used to analyse the variability of the model parameters across all solutions to estimate parameter uncertainties. An ideal point in objective space is determined and the solutions close to the ideal point are evaluated to determine the variability of these solutions in parameter space, which indicates parameter uncertainties (Kozlovskaya et al., 2007). The solution with the smallest euclidean distance to the ideal point is rated as the optimal solution found by the algorithm.

In our tests we will consider the hypothetical solution with a misfit of $\boldsymbol{\delta} = \mathbf{1}$ in all objectives as the ideal solution or ideal point for our tests, with

$$\begin{aligned}\boldsymbol{\delta} &= (\delta_1, \delta_2, \dots, \delta_N)^T \\ \mathbf{1} &= (1, 1, \dots, 1)^T.\end{aligned}$$

Weighted means \bar{x} and the corresponding variances σ_x^2 are calculated for all parameters $\{x_k\}_{k=1 \dots n_{\text{arch.}}}$:

$$\bar{x} = \frac{\sum_{k=1}^{n_{\text{arch.}}} w_k \cdot x_k}{\sum_{k=1}^{n_{\text{arch.}}} w_k}, \quad (3.4a)$$

$$\sigma_x^2 = \frac{\left(\sum_{k=1}^{n_{\text{arch.}}} w_k \cdot (x_k - \bar{x})^2 \right) \cdot \sum_{k=1}^{n_{\text{arch.}}} w_k}{\left(\sum_{k=1}^{n_{\text{arch.}}} w_k \right)^2 - \sum_{k=1}^{n_{\text{arch.}}} w_k^2}. \quad (3.4b)$$

The weights $\{w_k\}$ are chosen as the distance of a given solution k to the ideal solution in objective space:

$$w_k = \|(\boldsymbol{\delta}_k - \mathbf{1})\|_2. \quad (3.5)$$

This ensures that solutions closest to the ideal point have the largest influence on the result. The regularisation objective is not included in the computation of the weights, as it is not calculated as a misfit-function.

The solution's distance from the ideal point is also used to assess the convergence of the population during an inversion run by calculating the median of the distances of all analysed solutions.

3.2.4 Data set compatibility

The Pareto-front objective trade-off surfaces can be used to analyse the compatibility of the different objectives to each other. The shape and evolution of the fronts during search progression is dependent on the compatibility of the objectives.

Identical data sets are considered maximal compatible. Hence, for any solution the misfits $\{\boldsymbol{\delta}_k\}_{k=1 \dots n_{\text{arch.}}}$ for perfectly compatible data sets would be identical across all N objectives and would be distributed in objective misfit space along $\delta_{k,1} = \delta_{k,2} = \dots = \delta_{k,N} \forall k$. Therefore, in 2-objective misfit space the ideal fit is equivalent to a line with slope $m_{\text{ideal}} = 1$.

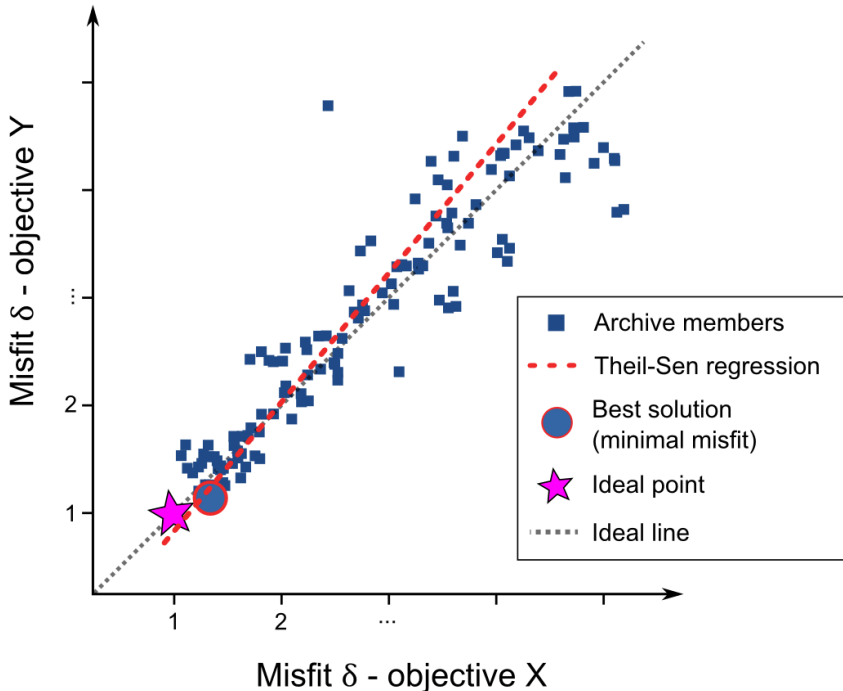


Figure 3.4: Conceptual misfit visualisation of two objectives for a hypothetical archive of two compatible data sets. The archive members are scattered around the ideal line with slope 1. The optimal solution is defined as the archive member with the smallest norm deviation from the point **1** in the space of normalised misfits. The slope of a Theil-Sen linear regression through all archive members is calculated to evaluate the compatibility of the data sets.

To assess the pairwise compatibility of any two objectives we calculate a linear fit for the solutions in the 2-D plane of objective misfit space of the objectives in question. The deviation of this fit from the ideal line with slope 1 indicates the degree of compatibility between the two data sets. This scheme is illustrated in Figure 3.4.

The standard linear least squares regression (Lawson and Hanson, 1974) is a non-robust measure (McKean, 2004). We choose the robust Theil-Sen estimator (Theil, 1950; Sen, 1968) as a regression method to avoid bias from outliers without needing to analyse the data set for outliers. For a set of Q 2-D points $\{(x_i, y_i) \mid i = 1 \dots Q\}$ this estimator is calculated as the median \tilde{m} of the slopes $\{m_{i,j} \mid i, j = 1 \dots Q\}$ calculated between every possible two point combination:

$$m_{i,j} = \frac{y_j - y_i}{x_j - x_i} \quad \forall i \neq j, i > j; \quad \tilde{m} = \text{median}\{m_{i,j}\}. \quad (3.6)$$

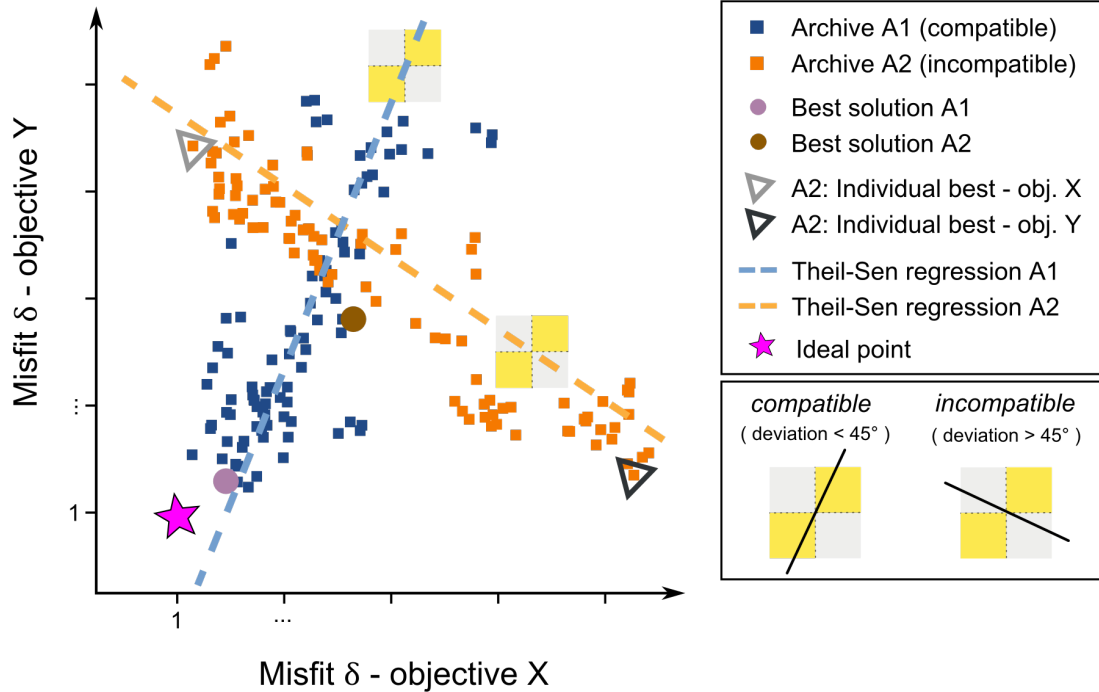


Figure 3.5: Conceptual misfit visualisations for two hypothetical pairs of data sets: one pair of compatible data sets (blue) and one pair of incompatible data sets (orange). The members of the archive of models for the compatible data exhibit the properties explained in Figure 3.4, but with a higher degree of scattering. The incompatible data yield individually optimised solutions for each objective, but their archive does not contain members with small overall deviation norms. The slopes of the Theil-Sen regressions through both archives are indicated by 'compatible' and 'incompatible' regions. The slope for the compatible points is positive, whereas incompatible data sets are characterised by negative slopes of the regression.

The opening angle γ between the ideal line and the fitted line is assessed. We compute

$$\tan \gamma = \left| \frac{\tilde{m} - m_{\text{ideal}}}{1 + \tilde{m} \cdot m_{\text{ideal}}} \right| = \left| \frac{\tilde{m} - 1}{1 + \tilde{m}} \right|, \quad (3.7)$$

to make the analysis independent of the choice of objective misfit scale.

In a graphical representation with identically scaled axes perfect compatibility results in a deviation angle from the ideal line of $\gamma = 0^\circ$ and maximum incompatibility results in a deviation angle of $\gamma = 90^\circ$. Deviation angles of $\gamma < 45^\circ$ indicate data compatibility, whereas deviation angles of $\gamma > 45^\circ$ indicate incompatibility. Figure 3.5 demonstrates the conceptual differences between the misfits of solutions for compatible and incompatible data sets respectively.

For real world data sets, perfect compatibility can never be achieved due to a variety of reasons, which will have different manifestations in the way the Pareto-fronts deviate from the ideal line: different methods can have different sensitivities and resolution, different depth of investigation, or data sets might have different levels of data error. Different sensitivities or different depth of investigation can cause data sets to neither be fully compatible nor incompatible, but rather partially compatible or disconnected. The Pareto-fronts surfaces for disconnected or partially compatible data sets will have different characteristics than fronts of truly incompatible data sets.

3.3 Feasibility Study: Example Data

We demonstrate the functionality of our approach using sets of synthetic data. Since the authors field of expertise is EM geophysics, we use simulated 1-D magnetotellurics (MT) data sets and resistivity well-logs, which will be inverted for isotropic resistivity and layer thickness. However, the algorithm is not in any way restricted to any specific type of data, but can be applied to other geophysical methods.

By using 1-D MT data we ensure complete controllability of the compatibility of the data sets, while still being able to simulate a variety of different compatibility situations, such as partially compatible data sets with different depth of sensitivity.

The depth sensitivity for EM methods is expressed as the skin depth ζ , which is dependent on the apparent resistivity of the medium ρ_a and on the signal frequency ω (Simpson and Bahr, 2005, p. 2):

$$\zeta = \sqrt{\frac{2\rho_a}{\omega\mu_0}}. \quad (3.8)$$

The misfit for the i -th frequency is calculated as

$$\delta_\nu^F = \sqrt{\left(\frac{d_\nu - F(\mathbf{m})_\nu}{\sigma_{d_\nu}}\right)^2}. \quad (3.9)$$

To assess partial compatibility we analyse the misfits for each individual recording frequency, in addition to the standard misfits, calculated from the sum of all individual misfits.

Using 1-D data also enables easy implementation and greatly reduces the runtime of the algorithm, allowing for intensive testing.

There are a variety of different regularisation functionals with different characteristics (Pek and Santos, 2006, p. 144), of which we use the discretised version (discretisation h) of the total variation functional (Rudin et al., 1992)

$$\sum_{i=1}^{n_{\text{layers}}} \sqrt{(\mathbf{m}_i - \mathbf{m}_{i-1})^2 + \beta^2} \xrightarrow{h \rightarrow 0} \int_0^\infty |\nabla \mathbf{m}(z)| dz, \quad (3.10)$$

with a small regularisation constant $\beta > 0$ for numerical stabilisation. We chose the total variation, as it can conserve sharp contrast in the model. This is advantageous, as sharp contrasts are often required in layered models. In a conventional inversion scheme the regularisation functional is part of the objective function and its influence in comparison to the misfit measure(s) is determined by a weighting factor, which has to be determined appropriately. Treating the regularisation functional separately from the objective-functions eliminates the need to find this weight factor.

We created two different synthetic resistivity models (Figure 3.6). Model I is the reference model with a low-resistivity anomaly between 500–600 m and Model II has been designed to generate data incompatible to the first set. Model II has higher resistivities than Model I in the top 1290 m of the model and lower resistivities below that depth.

3.3.1 Data set properties

For each of the models two MT data sets with different frequency ranges are created using Wait's recursion formula (Wait, 1954). This allows us to assess how the compatibility measures behave for data with different depths of sensitivity. The MT data sets have 17 frequencies each, with a frequency range of 6–1448 Hz (broadband (BB) data), and 128–32768 Hz respectively (audio-magnetotelluric (AMT) data). Eight data points of each of the two different types of MT data lie within the overlapping frequency range of 128–1448 Hz. Everything deeper than the penetration depth corresponding to a 128 Hz signal can therefore only be detected by the simulated BB MT measurements. Additionally, a resistivity well-log

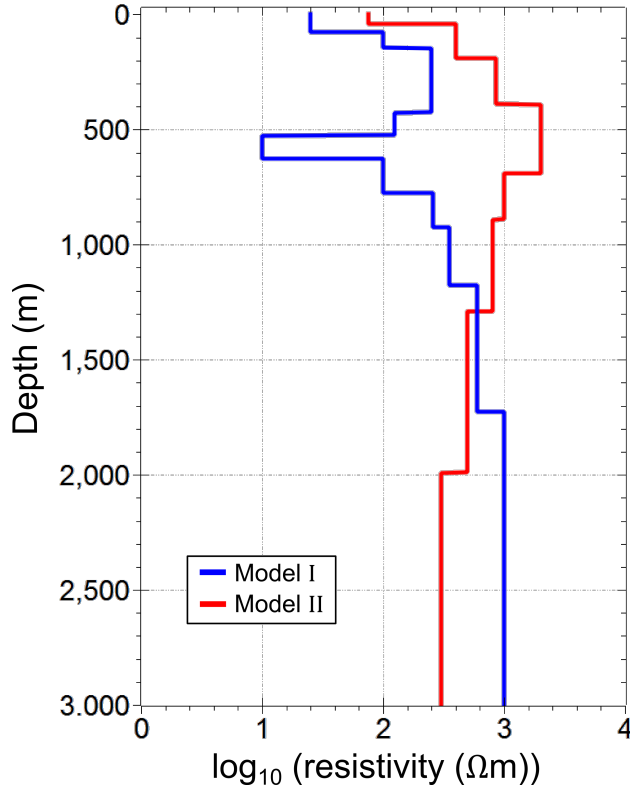


Figure 3.6: The synthetic 9-layer model Model I (blue) and the synthetic 7-layer model Model II (red).

was built for each model, ranging from a depth of 150 m to 1000 m, with a 0.25 m sample interval, reflecting a realistic data range.

White noise with a standard deviation equivalent to 3 % of the impedance tensor amplitude is added to both the MT data types. Accordingly, error estimates equivalent to 3 % of the impedance tensor amplitudes are assigned. White noise of 5 % is added to the well-log data and error estimates equivalent to 5 % of the parameter values are assigned.

For Model I we also generate an AMT data set with 5 % white noise added and 5 % error assigned, as well as an AMT data with 10 % noise added and 5 % error assigned. These data sets are used to analyse the influence of noise on the compatibility measures. If not specified otherwise the MT data sets with 3 % noise and 3 % errors are used.

All tests were run for 250000 solution evaluations each. For the data set compatibility analysis intermediate solutions archives are extracted after 1000, 10000, and 100000 solution evaluations in addition to the final archive.

As all non-dominated solutions are retained during the processing, the same solutions can be contained in multiple iterations of the archive. Hence, whenever solutions from multiple archives are analysed together only unique solutions are considered to avoid skewing the statistical analysis.

3.3.2 Resulting model distribution

The resulting ensemble of models is evaluated with regard to the geometry and the resistivity of the layers.

The parameters of each solution are transferred into a unified segment space to allow for better comparability between the different archive solutions, which have the same number of layers but different layer thicknesses. The depth interval between the surface and the deepest estimate for the bottom of the last layer is evenly divided into model segments. The parameter values of the different layers are mapped to the corresponding resulting segments for each solution, and the parameter distributions for the segments are analysed statistically.

For MT data the sensitivity decreases with depth, but the segments are of constant thickness. This guarantees that no information is lost when jointly working with data sets from different methods, which have varying sensitivities and resolution.

The segment resistivities are analysed by calculating weighted averages across all extracted solutions as described in Section 3.2.3.

The layer geometry is evaluated by computing the probability for an interface to be located in a specific segment. This is calculated using the number of archive solutions that have an interface in a given segment c_i and the total number of final archive solutions $n_{\text{arch.}}$:

$$p_i^{\text{interface}} = \frac{c_i}{n_{\text{arch.}}}, i \in \{1, 2, \dots, n_{\text{seg.}}\} \quad (3.11a)$$

$$\Rightarrow \sum_i^{n_{\text{seg.}}} p_i^{\text{interface}} = n_{\text{layers.}} \quad (3.11b)$$

If all solutions have an interface in the same segment, the interface probability at that segment will be 1. Including the top interface of the first

layer, which is always assigned a probability of 1, the sum of all interface probabilities over all segments equals the number of model layers.

In addition to the standard misfit for all data points, as defined in Equation (3.2), for the MT data we calculate the cumulative misfit over the eight overlapping frequencies (CMOF) 128–1448 Hz (Equation (3.9)), to allow for a detailed comparison of the identical sensitivity regions of the different MT data types:

$$\delta^{\text{CMOF}} = \sqrt{\frac{1}{8} \sum_{\nu=0}^8 \delta_\nu^F} \quad (3.12)$$

For different types of data, for example seismic data, potential field data, and different configurations of data, such as 2-D and 3-D data sets, the analysis of the resulting models may vary accordingly.

3.4 Feasibility Study: Analysis

The MOJO algorithm’s resulting model outputs will depend on the respective forward modules and their implementations. The detailed analysis and evaluation of the modelling software dependent characteristics of the final models is therefore not within the scope of this work. We rather focus on the evaluation and analysis of the overall solution space, and especially on the interpretation of data compatibility.

In order to demonstrate the feasibility of MOJO, we analyse the example data sets successively and in detail, to illustrate the influences of the various parameters. Firstly, we demonstrate the overall functionality and present the algorithm’s outputs using ideal compatible data. Secondly, we evaluate the influence of data noise and uncertainty. Then we characterise incompatible data sets, and extend the concepts from two to multiple objectives. Finally, we discuss the negative influence of ill posed problems and the lack of adequate regularisation.

3.4.1 Two objectives - compatible data sets

We will first evaluate a simple case with two objectives to introduce the concepts of MOJO data analysis. The objectives are built from AMT and BB data sets, combined with regularisation. This compatible data example uses the MT data sets that both have been calculated from Model I.

3.4.1.1 Optimal data without noise

We first analyse noise-free data to isolate the effects of the degree of compatibility. A small error floor is required to stabilise the inversion and allow for the calculation of standard misfits (c.f. Equation (3.2)). We use 0.4 % of the impedance tensor amplitude.

Firstly, we look at the model output that is generated using the methods described in Sections 3.2.3 and 3.3.2. Displayed in Figure 3.7 are the best solution and the average result based on the final solution archive after 250000 solution evaluations. The best solution as well as the average model achieve qualitatively good fits. The optimal solution achieved misfits of $\delta_{\text{AMT}_I} = 1.2$ and $\delta_{\text{BB}_I} = 1.5$ and is at a distance of 0.5 from the ideal point. The average model exhibits an average standard deviation of 6 % relative to the average segment values. The low resistivity anomaly of Model I at depths of 525–625 m is detected and placed in the correct depth range, but can not be resolved in detail. The inversion algorithm produces a single layer that has the same conductance as the layers of the true model in the corresponding depth range. This causes the same surface response as the true model, but results in an overestimation of the resistivity of the anomaly with $24 \Omega\text{m}$ for the best solution and $29 \Omega\text{m}$ for the average model, as opposed to the $10 \Omega\text{m}$ of the true model. The locations of the layer interfaces are well determined at low depths, but are subject to higher uncertainty at larger depths, as can be expected from the use of MT data. From a depth of about 1500–2500 m the interface probabilities are nearly equally distributed, not indicating any well determined interface positions. This shows the benefit of the joint inversion, as the region of the model to depth of 700–800 m, where the interfaces are better determined, corresponds to the part of the model that is jointly constrained by

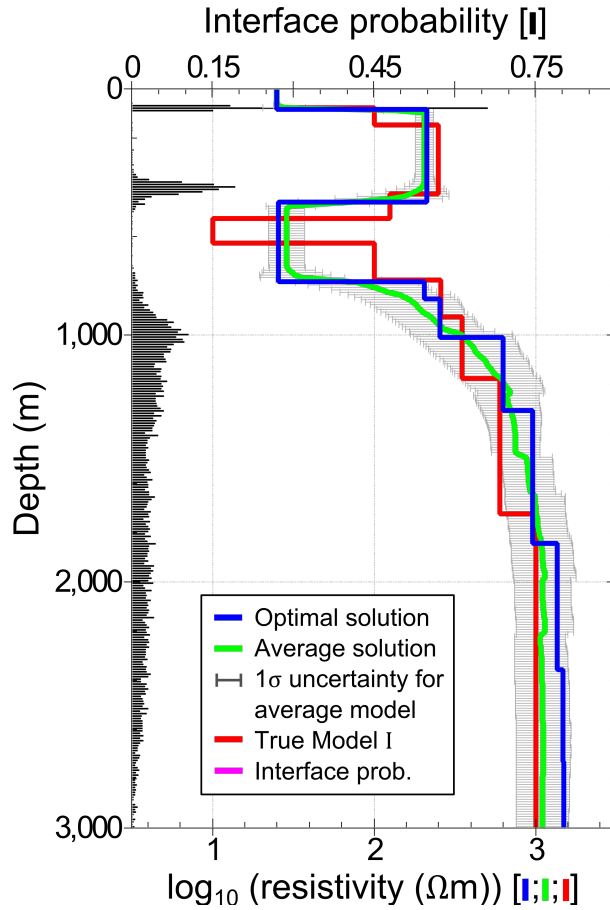


Figure 3.7: Model results from the noise-free 2-objective case (Section 3.4.1.1). The red line shows the true synthetic models and the green line represents the weighted average models based on the 1101 solutions of the final archive, including the model uncertainties in grey. The optimal solution is presented in blue. It achieved misfits of $\delta_{\text{AMT}_I} = 1.2$ and $\delta_{\text{BB}_I} = 1.5$ and was at a distance of 0.5 from the ideal point. The average model exhibits an average standard deviation of 6 % relative to the average segment values. The interface probabilities are presented in black calculated from the final archive solutions.

both MT data sets. This is also illustrated by the smaller error bars of the average model in that depth range. Figure 3.8a displays the coinciding frequencies cumulative misfits of the AMT and BB data sets for all extracted archive solutions. The display is a projection from the space of objectives combined with the regularisation onto the $\delta_{\text{AMT}}-\delta_{\text{BB}}$ -plane. As expected for perfectly compatible noise-free data the solutions are distributed along the ideal line and the Theil-Sen analysis yields a linear fit that does not show any deviation from the ideal line (Table 3.1).

Figure 3.8b shows the locations in objective space of all solutions extracted from the archives for all frequencies. The solutions are not distributed

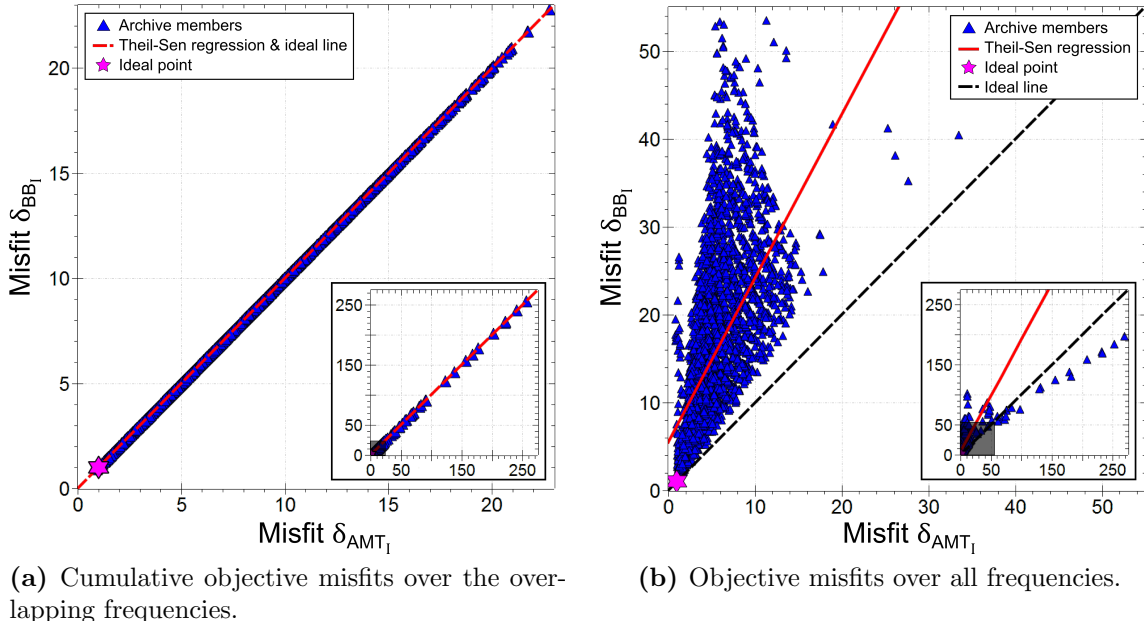


Figure 3.8: Pareto-front for the AMT-objective and the BB-objective in the compatible noise-free 2-objective case (Section 3.4.1.1). The 2620 unique solutions combined from the archives after 1000, 10000, 100000 and 250000 solution evaluations are displayed. The solutions are represented by blue triangles and the ideal point is represented by a magenta star. The red line represents the corresponding Theil-Sen regression and the dashed line represents the ideal line. The main plots show the main cluster of the solution distribution and its extent is marked by a grey box in the inset, which shows an overview of complete distribution. (a) cumulative objective misfits over the overlapping frequencies (c.f. Equation (3.12)). (b) objective misfits over all frequencies (Equation (3.2)). All following solution distribution plots are presented in the same manner.

along the ideal line, but are clustered in a cone shape, shifted towards higher misfits in BB. The main cluster extends over a misfit of about 1–17 in the direction of the AMT misfit and over 1–54 in direction of the BB misfit. The linear fit through all solutions deviates from the ideal line by 17° (Table 3.1).

The reasons for this asymmetry of the solution cluster is that the data span different frequency ranges. The BB data include the lower frequencies and so are sensitive not only to the same depth ranges as the AMT data set, but also cover deeper regions. Therefore, the BB data constrain the complete bandwidth of AMT data, but vice versa the AMT data only partially constrains the BB data. Hence, there can be solutions that vary at depths below the AMT sensitivity threshold and will show identical misfits for the AMT data set, but different misfits for the BB data.

Table 3.1: Analysis of the deviation from the ideal line and median distance from the ideal point (1,1) for the noise-free compatible 2-objective case (Section 3.4.1.1). The analysis is performed for archives at different stages of the inversion run, as well as for all extracted archive members combined and the CMOF of the combined archive members.

Solution evaluations	Deviation from ideal line	Median distance from ideal point
1000	66°	65.6
10000	17°	17.0
100000	18°	17.2
250000	18°	17.6
Combined	17°	—
CMOF	0°	9.9

3.4.1.2 Influence of white noise

After we have demonstrated the general functionality we now test what influence data noise has on the compatibility measures and the model quality. We use the same raw data as in Section 3.4.1.1, but with 3% white noise added.

Figure 3.9 shows the best solution and the average result for the compatible case calculated from the final solution archive. The best solution and the average model show characteristics similar to the noise-free case. The optimal solution achieved misfits of $\delta_{\text{AMT}_I} = 1.3$ and $\delta_{\text{BB}_I} = 1.5$ and was at a distance of 0.5 from the ideal point. The average model exhibits an average standard deviation of 21% relative to the average segment values. The added noise slightly increases the overestimation of the resistivity in the low resistivity zone, which reaches values of $30 \Omega\text{m}$ for the best solution and $43 \Omega\text{m}$ for the average model, as opposed to the $10 \Omega\text{m}$ of the true model. Noise effects also lead to an underestimation of the resistivities at greater depths, with the best solution showing a closer fit than the average solution. As in Section 3.4.1.1 the locations of layer interfaces are well determined at low depths, but are subject to higher uncertainty at larger depths.

The CMOF are shown in Figure 3.10a. As for the noise-free setup the solutions are distributed along the ideal line. The noise causes the linear fit to deviate from the ideal line by 3°.

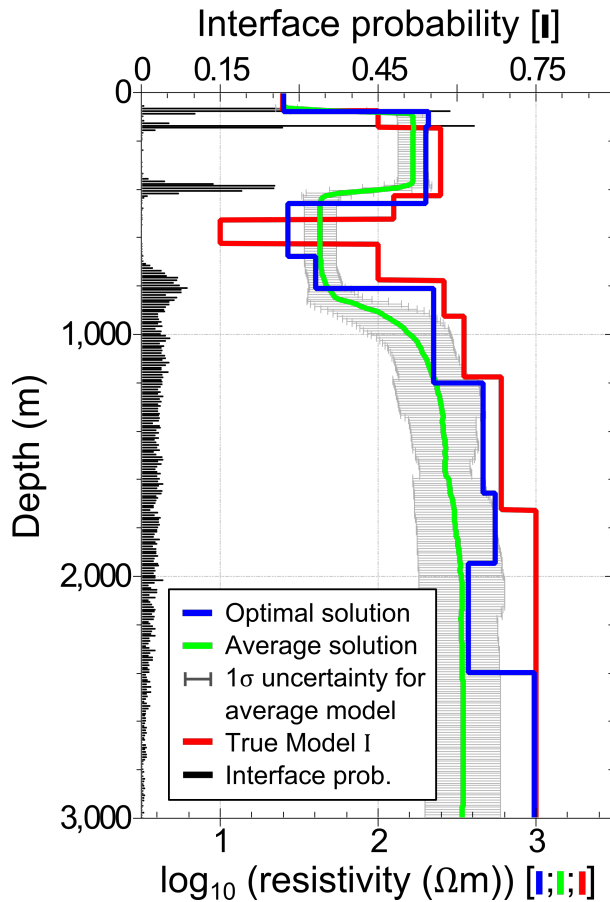


Figure 3.9: Model results from the 2-objective case with 3 % noise (Section 3.4.1.2). The red line shows the true synthetic models and the green line represents the weighted average models based on the 1142 solutions of the final archive, including the model uncertainties in grey. The optimal solution is presented in blue. It achieved misfits of $\delta_{\text{AMT}_I} = 1.3$ and $\delta_{\text{BB}_I} = 1.5$ and was at a distance of 0.5 from the ideal point. The average model exhibits an average standard deviation of 21 % relative to the average segment values. The interface probabilities are presented in black calculated from the final archive solutions.

Figure 3.10b displays the locations in objective space of all the solutions extracted from the archives. Again, the different depths of investigation of the two data sets cause the solutions to be distributed in a cone shape, shifted towards higher BB misfits. The main cluster extends over a misfit of about 1.3–2.4 in the direction of the AMT misfit and from about 1.5–6.8 in direction of the BB misfit, with the optimal solution found with misfits of $\delta_{\text{AMT}_I} = 1.3$ and $\delta_{\text{BB}_I} = 1.5$, at a distance of 0.6 from the ideal point. The deviation of the linear fit from the ideal line is 23°, which is similar to the noise-free case (Table 3.2).

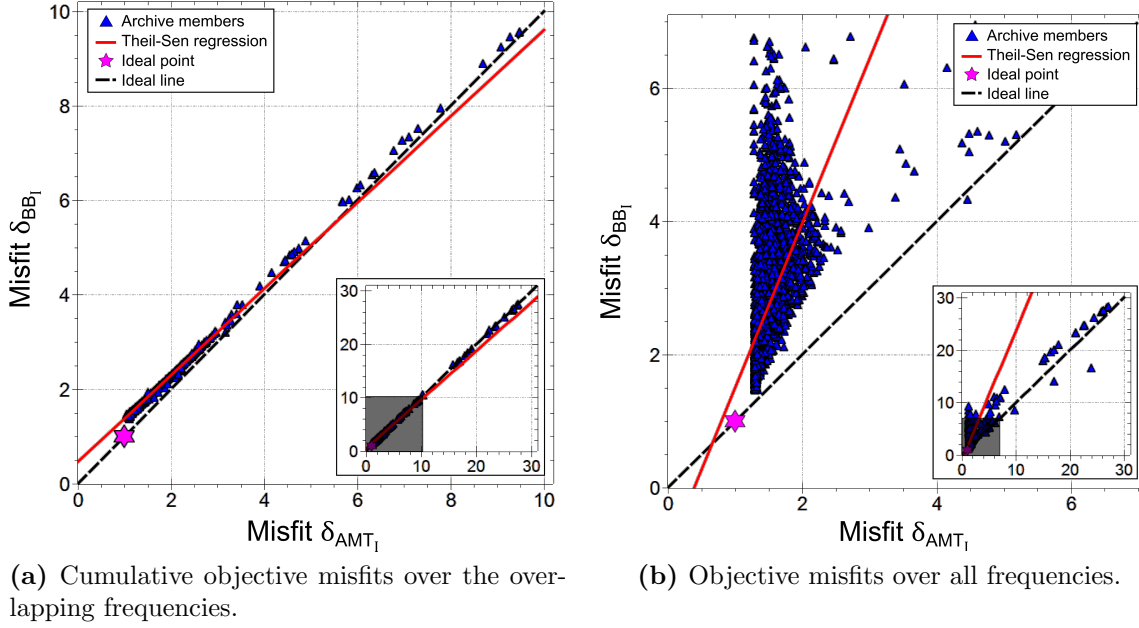
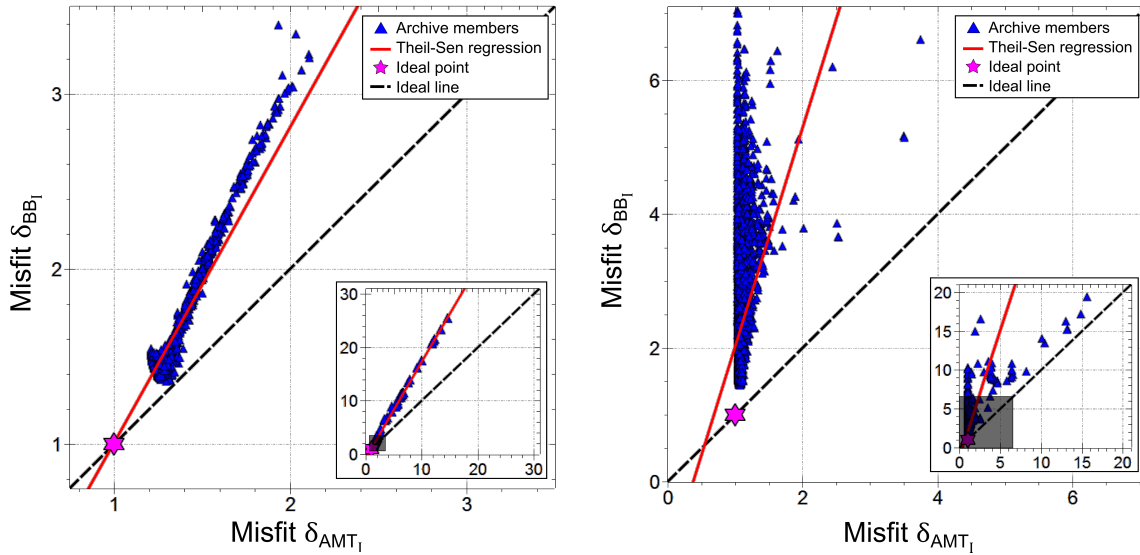


Figure 3.10: Pareto-front for the AMT-objective and the BB-objective in the compatible 2-objective case with 3 % noise (Section 3.4.1.2). The 2440 unique solutions combined from the archives after 1000, 10000, 100000 and 250000 solution evaluations are displayed, as well as the corresponding Theil-Sen regression, the ideal line, and the ideal point.

This test shows that data noise has an influence on the deviation from the ideal line. To investigate this influence in greater detail we perform two tests that use the same BB data set configuration as before, but AMT data sets with 5 % and 10 % noise white noise added. The errors for both AMT data sets are estimated as 5 % of the impedance values. The data set with

Table 3.2: Analysis of the deviation from the ideal line and median distance from the ideal point (1,1) for the compatible 2-objective case (with 3 % noise) (Section 3.4.1.2). The analysis is performed for archives at different stages of the inversion run, as well as for all extracted archive members combined and the CMOF of the combined archive members.

Solution evaluations	Deviation from ideal line	Median distance from ideal point
1000	27°	5.6
10000	9°	2.3
100000	26°	1.9
250000	23°	1.9
Combined	23°	—
CMOF	3°	0.8



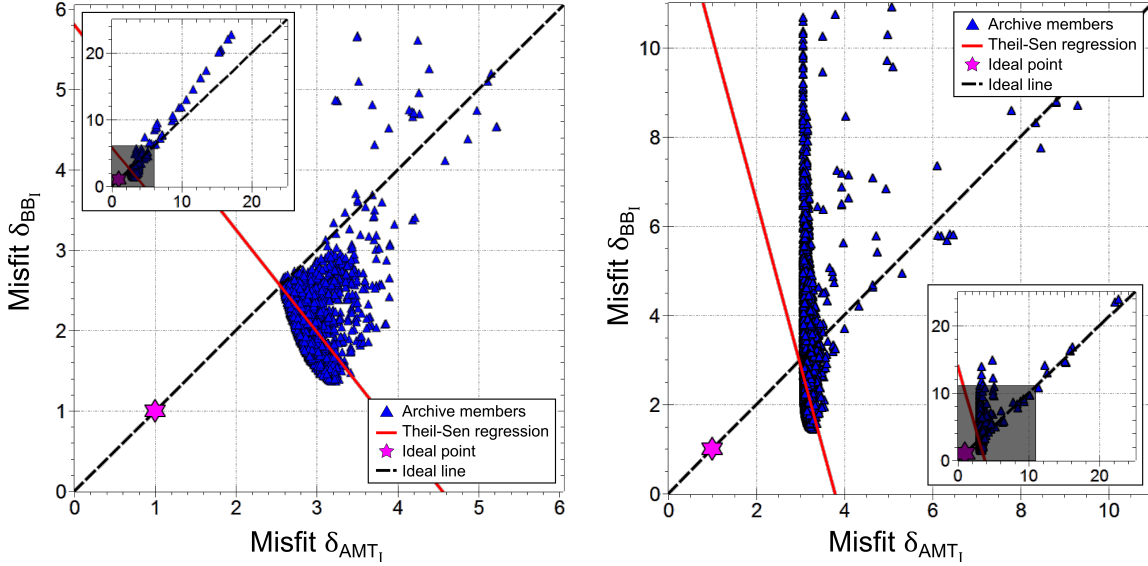
(a) Cumulative objective misfits over the overlapping frequencies.
(b) Objective misfits over all frequencies.

Figure 3.11: Pareto-front for the AMT-objective and the BB-objective in the compatible 2-objective case with 3 % noise and assigned errors for the BB data set and 5 % noise and 5 % assigned errors for the AMT data set (Section 3.4.1.2). The 2530 unique solutions combined from the archives after 1000, 10000, 100000 and 250000 solution evaluations are displayed, as well as the corresponding Theil-Sen regression, the ideal line, and the ideal point.

a higher noise level than the assigned data error simulates a real world situation where the actual noise level is underestimated. Hereinafter we will identify these two test runs as the *5/5-case* and the *10/5-case* respectively.

Figure 3.11 shows the distributions of the solutions for the 5/5-case, which exhibit a similar pattern as for the original data sets (Figure 3.10). The linear fits show higher deviations from the ideal line than before, with 28° (+22 %) for all solutions and 16.0° (+519 %) for the CMOF (Table 3.3). Comparing the median distances from the ideal solution with the original data sets it is apparent that the 5/5-case solutions are closer to the ideal solution. This is caused by the larger error floor of the AMT data sets, which allows for solutions that fit the BB data set more closely without worsening the AMT objective.

The solution distributions in the 10/5-case (Figure 3.12) vary from the distributions observed before. In the original case and the 5/5-case the solution distributions get narrower towards the ideal point, but for the 10/5-case the distribution widens towards the ideal point. The reason for



(a) Cumulative objective misfits over the overlapping frequencies.
(b) Objective misfits over all frequencies.

Figure 3.12: Pareto-front for the AMT-objective and the BB-objective in the compatible 2-objective case with 3% noise and assigned errors for the BB data set and 10% noise and 5% assigned errors for the AMT data set (Section 3.4.1.2). The 4049 unique solutions combined from the archives after 1000, 10000, 100000 and 250000 solution evaluations are displayed, as well as the corresponding Theil-Sen regression, the ideal line, and the ideal point.

this is the higher noise levels of the AMT data set, which are not appropriately reflected in the assigned error levels. This also causes a wider spread distribution for the CMOF (Figure 3.12a). The corresponding fit deviation

Table 3.3: Analysis of the deviation from the ideal line and median distance from the ideal point (1,1) for the 5/5-case and the 10/5-case (Section 3.4.1.2). The analysis is performed for archives at different stages of the inversion run, as well as for all extracted archive members combined and the CMOF of the combined archive members.

Solution evaluations	Deviation from ideal line		Median distance from ideal point	
	5/5-case	10/5-case	5/5-case	10/5-case
1000	62°	0°	8.5	6.9
10000	11°	61°	1.9	2.8
100000	30°	60°	1.4	2.5
250000	25°	56°	1.3	2.5
Combined	28°	60°	—	—
CMOF	16°	83°	0.6	2.2

angles show values that are clearly above the compatibility threshold of 45° , with 60° for all solutions and 83° for the CMOF (Table 3.3). A simple visual inspection of the complete CMOF distribution would suggest that the solutions were distributed close to the ideal line, but the robust linear fit is reflecting the dominance of main solution cluster close to the ideal point.

The imbalance of true noise and estimated error levels in the AMT data leads to the fact that no solutions with AMT objective values of less than $\delta_{\text{AMT}} = 3.1$ are found (Figure 3.12b), which is also reflected in the elevated median distances from the ideal point (Table 3.3).

3.4.2 Two objectives - incompatible data sets

We have established how resulting model distributions behave for compatible data. Now we explore the results of MOJO for incompatible data. The AMT data is built from Model I and the BB data is calculated using Model II to simulate data incompatibility.

3.4.2.1 Optimal data without noise

As for the compatible case we first analyse noise-free data sets. Figure 3.13 shows the optimal solution, the average model, and the interface probabilities based on the final archive. The optimal solution and the average model neither fit Model I nor Model II and the only interface probabilities of 0.1 or higher occur at depths of about 60 m and 435 m, which are depths where Model I and Model II have coinciding interfaces, which is in strong contrast to the compatible case in Section 3.4.2.1. The optimal solution achieved misfits of $\delta_{\text{AMT}_I} = 60.0$ and $\delta_{\text{BB}_{II}} = 114.3$ and was at a distance of 126.0 from the ideal point. The average model exhibits an average relative standard deviation of 13 %.

Major artefacts can be observed in the optimal solution, the most prominent being high resistivity artefacts of about $1750 \Omega\text{m}$ in the depths range of 395–930 m and $2190 \Omega\text{m}$ in the depth range of 1620–2160 m.

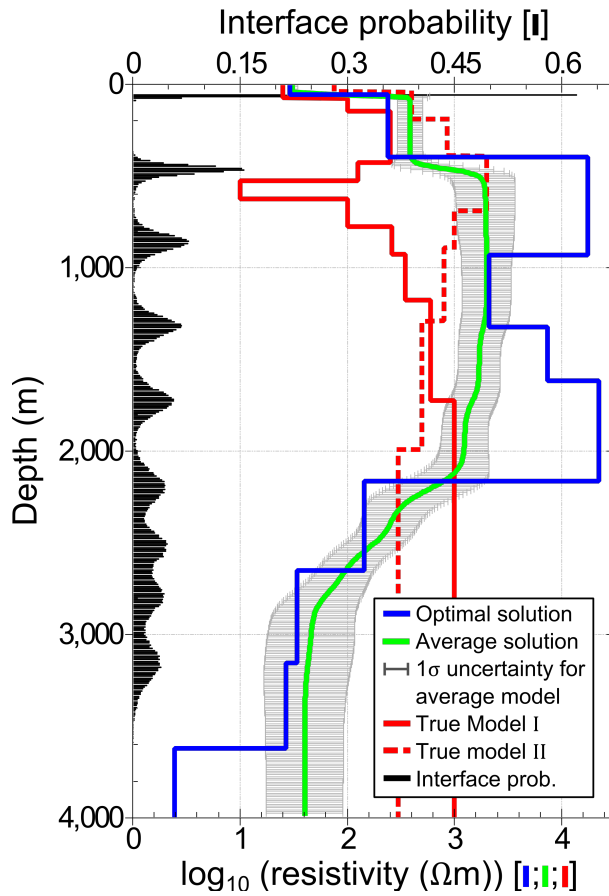
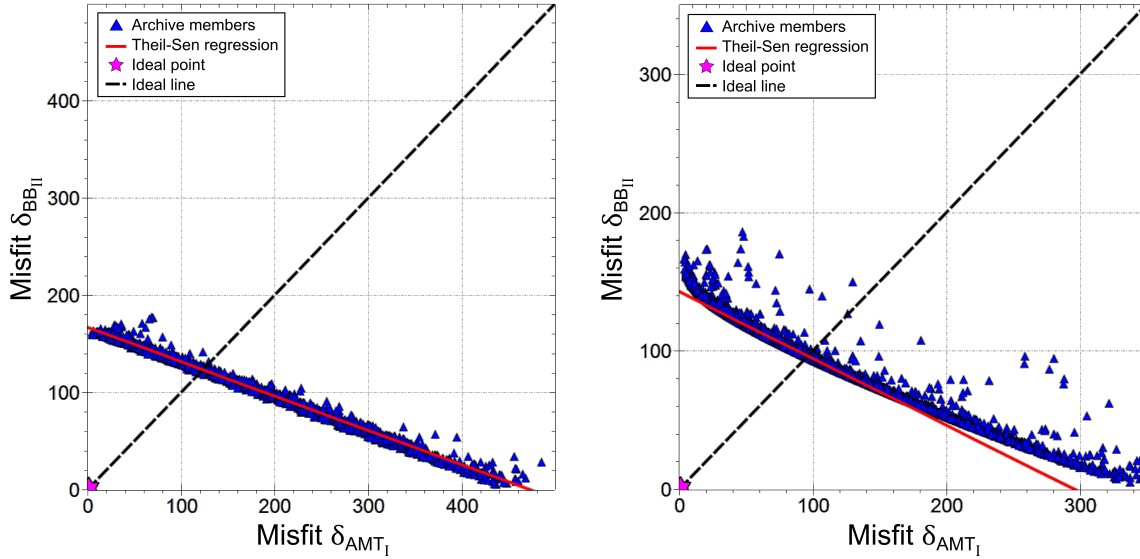


Figure 3.13: Model results from the incompatible noise-free 2-objective case (Section 3.4.2.1). The solid red line shows the true synthetic model Model I and the dashed red line represents the true synthetic model Model II. The green line represents the weighted average model based on the 17894 solutions of the final archive, including the model uncertainties in grey and the optimal solution is presented in blue. The optimal solution achieved misfits of $\delta_{\text{AMT}_I} = 60.0$ and $\delta_{\text{BB}_{II}} = 114.3$ and was at a distance of 126.0 from the ideal point. The average model exhibits an average standard deviation of 13% relative to the average segment values. The interface probabilities are presented in black calculated from the final archive solutions.

The solutions of the final archive exhibit a higher variability than in the compatible case, which is expressed in higher uncertainties of the average model.

The resulting Pareto-fronts are shown in Figure 3.14. The CMOF are distributed along a line with a deviation of 64° from the ideal line and a median distance from the ideal point of 164.2 (Table 3.4), which stands in strong contrast to the analysis of compatible data (Section 3.4.1.1). The main cluster of solutions covers AMT misfits of 4–350 and BB misfits of 5–170. These differences in misfit ranges are caused by the fact that the



(a) Cumulative objective misfits over the overlapping frequencies.
(b) Objective misfits over all frequencies.

Figure 3.14: Pareto-front for the AMT-objective and the BB-objective in the incompatible noise-free 2-objective case (Section 3.4.2.1). The 26553 unique solutions combined from the archives after 1000, 10000, 100000 and 250000 solution evaluations are displayed, as well as the corresponding Theil-Sen regression, the ideal line, and the ideal point.

models for Model I and Model II exhibit greater similarity at depth than close to the surface. Hence, the misfits of the lower frequency BB data are smaller.

Table 3.4: Analysis of the deviation from the ideal line and median distance from the ideal point (1,1) for the noise-free incompatible 2-objective case (Section 3.4.2.1). The analysis is performed for archives at different stages of the inversion run, as well as for all extracted archive members combined and the CMOF of the combined archive members.

Solution evaluations	Deviation from ideal line	Median distance from ideal point
1000	68°	158.0
10000	70°	139.3
100000	71°	132.1
250000	71°	130.5
Combined	71°	—
CMOF	64°	164.2

The same pattern can be observed for the full frequency range misfits (Figure 3.14b). Compared to the CMOF the line shows a higher degree of scatter, a slight curvature, and exhibits a deviation from the ideal line of 71° . This curvature is caused by the different frequency ranges of the two data sets.

The distances from the ideal solution and the large deviation from the ideal line illustrate that the algorithm is able to find solutions with low misfits for each of the objectives individually, but it is impossible to find a solution that reaches acceptable misfits for both objectives at the same time.

3.4.2.2 Influence of white noise

Repeating the analysis as in Section 3.4.2.1, but with 3% white noise added to the data generates Pareto-fronts that show qualitatively identical behaviour to the noise-free case in Section 3.4.2.1 (Figure 3.15). The deviation angles of the corresponding linear fits are 65° for the CMOF and 71° for the complete misfit (Table 3.5).

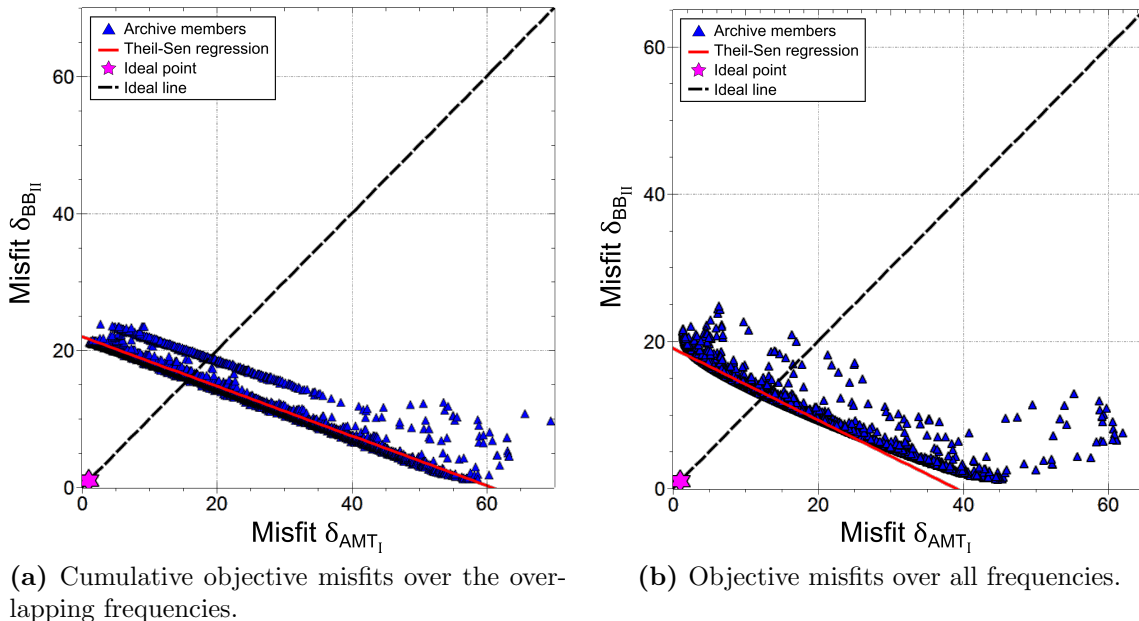


Figure 3.15: Pareto-front for the AMT-objective and the BB-objective in the incompatible 2-objective case with 3% noise (Section 3.4.2.2). The 22148 unique solutions combined from the archives after 1000, 10000, 100000 and 250000 solution evaluations are displayed, as well as the corresponding Theil-Sen regression, the ideal line, and the ideal point.

Table 3.5: Analysis of the deviation from the ideal line and median distance from the ideal point (1,1) for the incompatible data 2-objective case with 3% white noise on the data (Section 3.4.2.2). The analysis is performed for archives at different stages of the inversion run, as well as for all extracted archive members combined and the CMOF of the combined archive members.

Solution evaluations	Deviation from ideal line	Median distance from ideal point
1000	69°	20.1
10000	70°	17.8
100000	71°	16.7
250000	71°	16.4
Combined	71°	—
CMOF	65°	20.64

3.4.3 Multiple objectives

We perform two test runs with three objectives to investigate the behaviour of the compatibility measures for compatible and incompatible cases with more objectives. Both tests use the AMT and the BB data set based on Model I. The test simulating compatible data sets uses the synthetic resistivity well-log based on Model I and the test for incompatible data uses the Model II resistivity well-log. Both well-logs cover depths of 150–1000 m.

Figure 3.16 shows the best and average results for the compatible 3-objective case. The added information from the well-log helps to better define the position and resistivity of the low resistivity anomaly, compared to the 2-objective case in Section 3.4.1.2 (Figure 3.9). The anomaly is identified at the true location and has a resistivity of $11.8 \Omega\text{m}$ for the best solution and $24.5 \Omega\text{m}$ for the average solution. The benefit of the information added is also reflected in the smaller error bars of the average solution, as compared to the 2-objective case. It exhibits an average standard deviation of 18% relative to the average segment values.

As there are three objectives competing in this test, the compatibility analysis is performed pair-wise for each of the three possible 2-objective combinations. In the case of the compatible data sets the linear fits for ex-

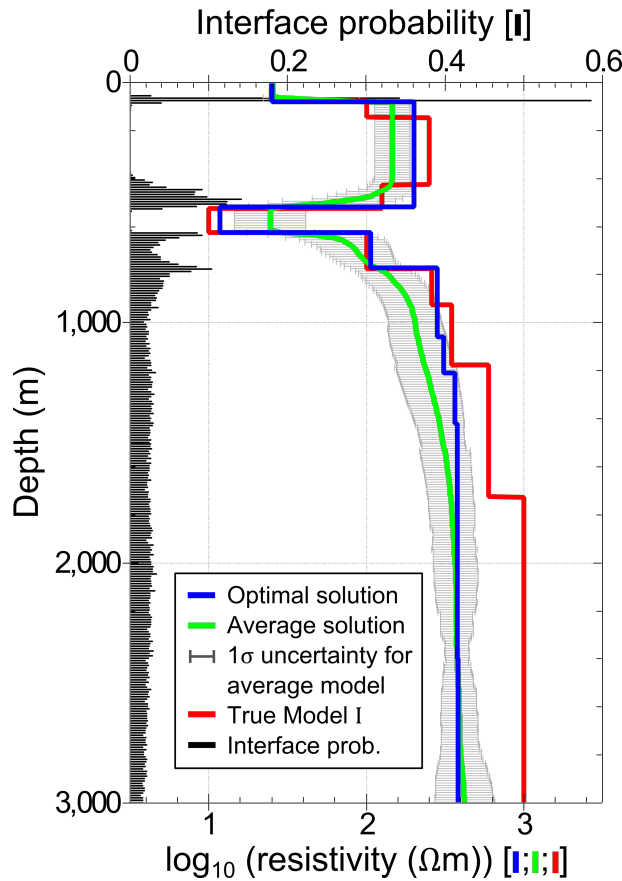


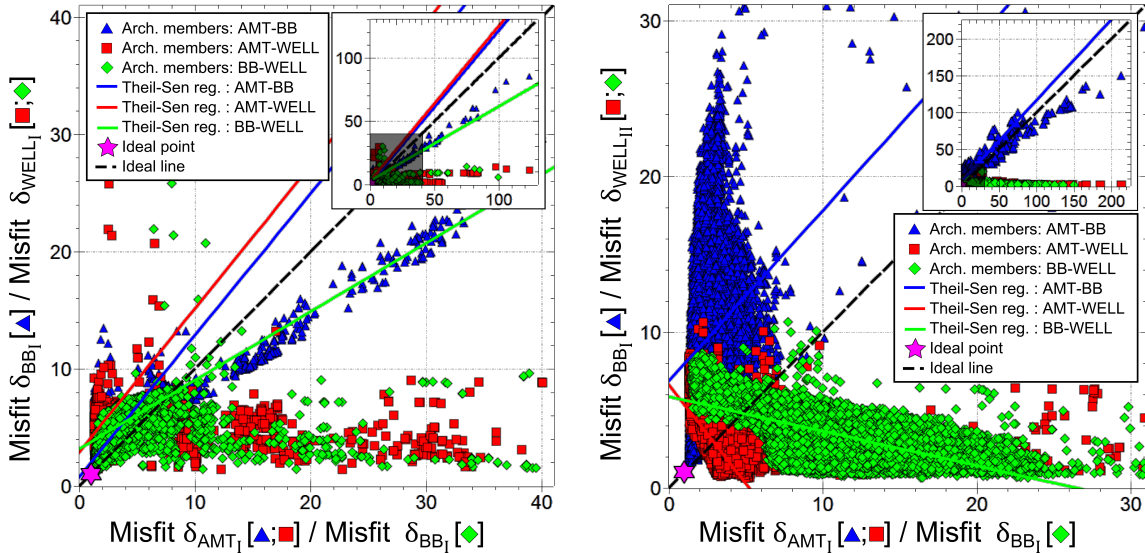
Figure 3.16: Model results from the multi-objective case (Section 3.4.3). The red line shows the true synthetic models and the green line represents the weighted average models based on the 6771 solutions of the final archive, including the model uncertainties in grey. The optimal solution is presented in blue. It achieved misfits of $\delta_{\text{AMT}_I} = 1.3$, $\delta_{\text{BB}_I} = 1.7$, and $\delta_{\text{WELL}_I} = 1.4$ and was at a distance of 0.8 from the ideal point. The average model exhibits an average standard deviation of 18 % relative to the average segment values. The interface probabilities are presented in black calculated from the final archive solutions.

tracted solutions exhibit deviations from the ideal line of $\gamma_{\text{comp};\text{AMT-BB}} = 5^\circ$, $\gamma_{\text{comp};\text{AMT-WELL}} = 6^\circ$ and $\gamma_{\text{comp};\text{BB-WELL}} = 15^\circ$, indicating good compatibility between all objectives (Table 3.6). The optimal found solution has objective values of $\delta_{\text{AMT}_I} = 1.3$, $\delta_{\text{BB}_I} = 1.7$ and $\delta_{\text{WELL}_I} = 1.4$, and is at a distance of 0.8 from the ideal point. The median distance of the final archive solutions from the ideal point is 4.85.

Good objective compatibility is also indicated for the two MT objectives in the case of incompatible data, with the linear fit for all solutions deviating by $\gamma_{\text{incomp};\text{AMT-BB}} = 3^\circ$. The two objective combinations featuring the well-log data on the other hand show clear signs of incompatibility.

Table 3.6: Analysis of the deviation from the ideal line and median distance from the ideal point (1,1,1) for the multi-objective case inversion runs (Section 3.4.3). The analysis is performed for archives at different stages of the inversion run, as well as for all extracted archive members combined and the CMOF of the combined archive members.

Solution evaluations	Deviation from ideal line						Median distance from ideal point	
	compatible data			incompatible data			comp.	incomp.
	AMT-BB	AMT-WELL	BB-WELL	AMT-BB	AMT-WELL	BB-WELL		
1000	28°	58°	64°	4°	49°	50°	11.6	11.1
10000	1°	32°	23°	20°	56°	53°	5.3	12.6
100000	2°	1°	15°	2°	86°	56°	5.0	9.8
250000	9°	13°	13°	6°	80°	59°	4.9	9.1
Combined	5°	6°	15°	3°	83°	57°	—	—



(a) Objective misfits over all frequencies for the compatible case, based on data sets AMT_I , BB_I and $WELL_I$. The 10878 unique solutions from the archive after 1000, 10000, 100000 and 250000 solution evaluations, are displayed

(b) Objective misfits over all frequencies for the incompatible case, based on data sets AMT_I , BB_I and $WELL_{II}$. The 20,806 unique solutions from the archive after 1000, 10000, 100000 and 250000 solution evaluations, are displayed.

Figure 3.17: Pareto-front for the AMT-BB-objectives (blue triangles), AMT-WELL-objectives (red squares) and BB-WELL-objectives (green diamonds) with the corresponding Theil-Sen regressions in the same colours, for the multi-objective case (Section 3.4.3). The ideal point is represented by a magenta star and the broken black line represents the ideal line.

The linear fit of the solutions projected onto the objective space plane of the AMT and the well-log misfit exhibits a deviation of $\gamma_{incomp;AMT-WELL} = 83^\circ$ from the ideal line, and for the combination of BB MT data and well-log the deviation is $\gamma_{incomp;BB-WELL} = 57^\circ$ (Table 3.6). This smaller deviation for the BB-WELL projection compared to the AMT-WELL combination is caused by the larger penetration depth of the BB data that exceeds the depth range constrained by the well-log, whereas most of the depth range the AMT data is sensitive to is constrained by the well-log. The median distance from the ideal point is 9.1, and as such significantly larger than for the compatible data.

The clear separation into compatible and incompatible data apparent from the analysis of the deviations of the linear fits from the ideal line is less obvious from a visual inspection of the solution distributions (Figure 3.17). The objective combinations including the well-log show similar solution distributions for the compatible and the incompatible case. In each case

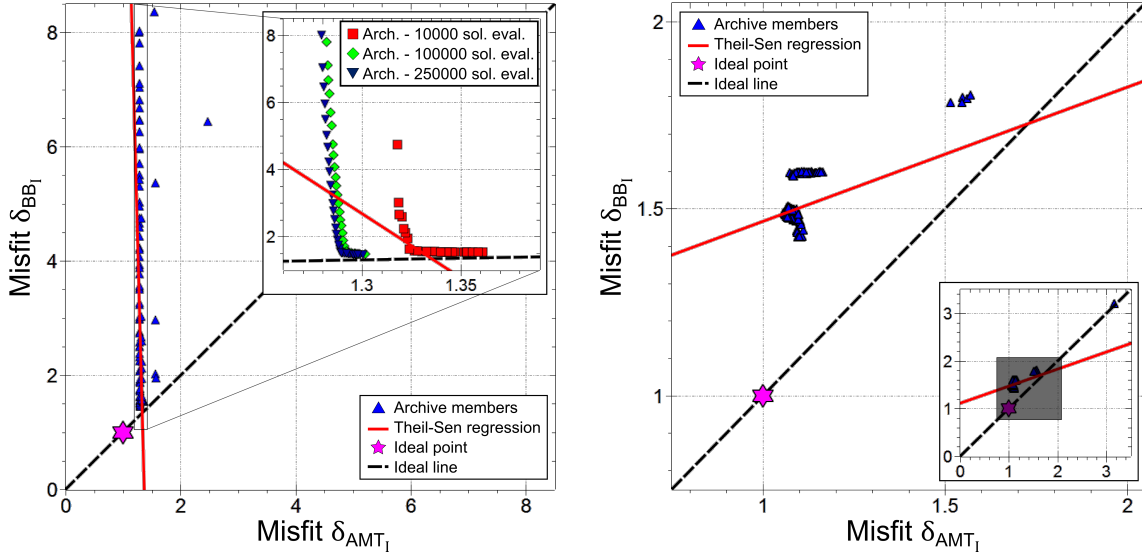
the main solution clusters have a width of about 10 in direction of the well-log objectives and a width of 40–90 in direction of the MT objectives. This asymmetry is caused by the fact that the well-log only constrains part of the model, so that models fitting the well-log can still vary significantly in the misfit of the MT data sets.

3.4.4 Influence of the numbers of objectives on the stability of the compatibility measure

Up to this point all presented test cases suggest that the angle of deviation in combination with the median distance from the ideal solution is a good indicator for data set compatibility. These criteria worked for almost all test configurations we examined, but we also found examples where this concept fails. One important case is a situation where assigned error levels do not reflect the actual noise level, as presented in Section 3.4.1.2.

Furthermore, problems can arise if an inversion is performed with only two objectives, omitting regularisation. To demonstrate this we use the same data sets as in the compatible 2-objective case (with 3% noise) (Section 3.4.1.2), but without employing regularisation. As a result no solution clustering occurs, as the nature of the definition of solution optimality based on Pareto non-domination only allows for solution fronts to form (Figure 3.18a). The linear fit of all analysed solutions exhibits a deviation from the ideal of 47° . Without prior knowledge this indicates incompatible objectives, although the data sets are compatible. The low median distances of the solutions from the ideal solution however indicate that the found solutions fit both objectives to acceptable levels (Table 3.7). It is only for the CMOF that a deviation angle of less than $\gamma < 45^\circ$ is achieved (Figure 3.18b). The fit deviation angle of $\gamma = 25^\circ$ and the median distance from the ideal point of 0.5 indicate objective compatibility (Table 3.7).

The solutions displayed in Figure 3.18a cover a wider misfit range for the BB data and the inset in Figure 3.18a illustrates that the Pareto-front is already close to the final front after just 10000 solution evaluations. Furthermore, the fronts form two arms, one of which extends along the δ_{BB_1} -direction and the other one extending along the ideal line. As discussed before this is caused by the greater penetration depth of the lower frequency BB data,



(a) Objective misfits over all frequencies. In the inset the solutions from the archive after 10000 (red squares), 100000 (green diamonds) and 250000 (blue triangles) solutions evaluations, are displayed.

(b) Cumulative objective misfits over the overlapping frequencies.

Figure 3.18: Pareto-front for the AMT-objective and the BB-objective in the 2-objective case without regularisation (Section 3.4.4). The 142 unique solutions combined from the archives after 1000, 10000, 100000 and 250000 solution evaluations are displayed, as well as the corresponding Theil-Sen regression, the ideal line, and the ideal point.

and the resulting asymmetry in the mutual constraining of BB and AMT data. The resulting misfit distribution is narrow in the AMT direction and wide in the BB direction. MOJO's ε -dominance criterion ensures solution

Table 3.7: Analysis of the deviation from the ideal line and median distance from the ideal point (1,1) for the 2-objective case without regularisation. The analysis is performed for archives at different stages of the inversion run, as well as for all extracted archive members combined and the CMOF of the combined archive members.

Solution evaluations	Deviation from ideal line	Median distance from ideal point
1000	45°	2.0
10000	79°	0.7
100000	45°	0.9
250000	45°	0.8
Combined	47°	—
CMOF	25°	0.5

diversity and limits the number of solutions per area, leading to more solutions along the BB direction than the AMT direction. This in turn results in the linear fit being dominated by the solutions along the BB axis.

We also performed an equivalent test with only two objectives for incompatible data. The solution distributions are very similar to the incompatible 2-objective case (Section 3.4.2.2) and the data sets are clearly identifiable as incompatible from the deviation angle and the median distance of the solutions to the ideal solution, as well as from visual inspection of the solution distribution in objective space.

In summary, compatible data may be misidentified as incompatible in situations with only two objectives and no regularisation, whereas incompatible data sets are clearly identified as incompatible at any stage.

3.5 Discussion

The MOJO algorithm is an evolutionary algorithm, which generates solution ensembles for geophysical inversion problems. The final set of models is interpreted as a distribution of possible models that can be analysed with respect to various model parameters and characteristics. These points hold for the analysis of arbitrary geophysical data as no general restrictions are inherently imposed on the data sets or on the actual inversion and modelling algorithms. This is in contrast to classical joint inversion approaches, which require weighting of the different data sets.

MOEAs also have the unique ability to effectively map the trade-offs between different objectives, which can be used to infer the objective compatibility. Similar trade-off surfaces could also be produced by testing large numbers of weight combinations for the different data sets. However, this would be computationally expensive and not all solutions accessible to a multi-objective Pareto-scheme can be found with conventional linearised approaches (Podinovsky and Nogin, 1982; Kozlovskaya et al., 2007). Hence, better solution space exploration can be achieved by using MOEAs.

MOEAs face unique issues, which are not encountered with conventional single-objective approaches, such as dominance resistance (Hanne, 2001;

Ikeda et al., 2001; Purshouse and Fleming, 2007) and population deterioration (Hanne, 1999). These can lead to poor performance of a MOEA, especially for many-objective problems, but can be counteracted with appropriate algorithm design, and the “Borg” MOEA used in this study counters these problems by applying ε -dominance (Laumanns et al., 2002; Hadka and Reed, 2013).

We have implemented the MOJO algorithm and have demonstrated its general applicability to geophysical data, using synthetic MT and well-log data. The resulting model distributions reproduced the original input parameters. The addition of (white) noise to the data, as well as a variation of data errors influence the absolute values of the model parameters (here layer depths and layer resistivities) and their respective uncertainties. The solution model distribution is robust under these variations, but the estimated values of the deep layer resistivities are more prone to be effected by noise, as deeper model areas are supported by fewer data points.

The evaluation of jointly inverted or jointly interpreted geophysical data is complicated, and it is vital to assess if information from different data sets can be jointly analysed in the first place. We have demonstrated that the output of the MOJO algorithm can be interpreted as a measure for the mutual compatibility of multiple data sets. The slope of the Theil-Sen regression of the projection of the solution distribution into 2-D objective space is a good indicator for objective compatibility. Incompatible objectives generally show deviations of $\gamma > 45^\circ$ and compatible objectives exhibit deviations of $\gamma < 45^\circ$.

The results for the deviation angles are consistent across individual archives, but cases can occur were the deviation angle results based on different intermediate archives vary significantly. Analysing only individual archives could therefore lead to false conclusions about the level of objective compatibility. Archives from the early stage of an inversion run in particular often contain only a small number of solutions, yielding misleading results. Hence, a maximal number of solutions should be extracted during inversion runs to be analysed together. The number of solutions that can be extracted for analysis is dependent on the computational facilities available. In particular, the calculation of the Theil-Sen estimator is computationally expensive, as for n solutions to be investigated, $\binom{n}{2}$ solution pairs have to

be analysed and saved to allow for the determination of the median. This makes the calculation primarily memory expensive. Nevertheless, such a robust linear regression approach is essential to achieving correct results, therefore computationally less expensive methods like the commonly used least-squares estimation are not suitable.

The necessity for a statistical analysis of the solution distributions is illustrated in Section 3.4.3. This case demonstrates that visual inspection can be deceiving and Theil-Sen analysis is required. Inspecting the solution distributions of the MT-well-log projections, the distributions look very similar for the compatible and the incompatible case, but the Theil-Sen analysis detects major differences in the distributions and correctly indicates the compatibility in both cases. The close clustering of a large number of solutions can especially lead to false interpretations, as distribution patterns may be obscured.

Evolutionary algorithms have an intrinsic robustness against the effects of low levels of noise, but noise can have a significant impact on convergence and population diversity of MOEAs (Goh and Tan, 2007). We tested the influence of different noise levels on the compatibility measure. The algorithm performed robustly in the presence of white noise and the objectives were reliably identified as compatible, providing the assigned data error estimate was adequate for the noise level. This was also supported by the analysis of the solution distance from the ideal point. The ideal line deviations for the high noise 5/5-case showed increased values (Section 3.4.1.2), but were still inside the compatibility envelope.

Instances with assigned error levels that do not reflect the true noise level can lead to misinterpretation of objective compatibility, as demonstrated in the 10/5-case. The assignment of too low error levels to one of the data sets caused the objectives to be identified as incompatible, as deviation angles for full misfit solutions, as well as for the CMOF were well above the $\gamma = 45^\circ$ threshold. The wrong error levels also caused elevated misfits for the affected objective, which lead to an increased median distance from the ideal point. Both indicators would point towards incompatibility between the two data sets. Correct assignment of error levels has to be assured before data is used in an inversion, to ensure valid results. This highlights

that for real data analysis in the future, particular attention has to be paid during data processing and data set preparation.

Any joint-inversion problem that uses a regularisation objective is at least a 3-objective situation. If a joint-inversion problem with only two objectives were to be performed, the results have to be interpreted with care, as compatibility may not be inferred correctly under these conditions, as demonstrated in Section 3.4.4. The nature of the Pareto-definition of optimality can lead to situations where solution distributions can be mistakenly interpreted as signs of objective incompatibility, if only the fit deviation is viewed without considering the distance of the solutions to the ideal solution. The deviation angles show values just above the compatibility threshold, whereas the distances from the ideal point are very low and indicate that acceptable misfits are reached for both objectives. Only the analysis of the misfits for the coinciding frequencies yields a deviation angle below the threshold, with $\gamma = 25^\circ$. These are the kind of solution distributions that also have been found to represent compatible objectives by Moorkamp et al. (2007). In cases like this a thorough visual and numerical analysis of the solution distributions has to be performed. This has to be done carefully, as close clustering of solutions can give false impressions. In the test situation the linear fit is dominated by solutions that extend along the δ_{BB_I} -direction. This is caused by the BB MT data fully constraining the AMT data, as the BB data have a higher penetration depth, which is expressed in the solution distribution being shifted towards higher BB data misfits. These types of shifted distribution can also be observed in (Moorkamp et al., 2010), especially for the combination of Rayleigh wave dispersion data and MT data. A detailed visual analysis in Section 3.4.4 reveals that the subset of solutions, which is closest to the ideal point exhibit the lowest misfits for both objectives, and its members are distributed along the ideal line, confirming that the objectives are indeed compatible.

We observed that the average misfits of the solutions increase with the number of jointly inverted objectives. The solutions of the final archive in the compatible multi-objective case (Section 3.4.3) reach a median distance from the ideal point of 4.85, compared to 1.90 in the 2-objective case (Section 3.4.1.2) and 0.80 in the 2-objective case without regularisation (Section 3.4.4). The more objectives are used, the more different noise components

are present and the wider spread the solution distributions become, which leads to larger median solution distances from the ideal point. The model result is improved by inverting multiple data sets together, which reduces the influence of the noise on the result, assuming that the noise components of the different data sets are uncorrelated.

For the assessment of the balance of mutual data constraint it is important that the misfits of the objectives are of comparable magnitude. The normalisation of the data misfits by the data error (Equation (3.2)) ensures that the misfits become comparable to some extend and also guarantees that fits below the error level are expressed in misfits of $\delta < 1$ regardless of the type of data. Nevertheless, different data types and/or varying error levels can influence the deviation measure and may bias the assessment of the mutual constraint balance, as seen in Section 3.4.1.2, where increased levels of data noise lead to larger deviation angles. Regardless of noise levels and the type of data the core concept of compatibility assessment will not break down. Compatible solutions will generally achieve linear fits with deviations of $\gamma < 45^\circ$. Further research is necessary to determine the level of influence different data types and noise levels have and to explore different misfit measures that might mitigate this problem, as current relative misfit measures, like the normalised root-mean-square deviation, do not take data errors into account.

Further work is also required on the appraisal of the solution ensemble to make multi-objective evolutionary algorithms a reliable tool that can be widely used for joint inversion of geophysical data. We have defined the best solution to be the one closest to the optimal solution with misfits of $\delta = 1$ for all objectives and have made a first attempt to estimate model uncertainties based on the work of Kozlovskaya et al. (2007). However, more research is needed to develop consistent workflows on the optimal selection of final solutions and to determine the ideal method to estimate model uncertainties from the solution ensemble.

The algorithm is implemented in C/C++ and has been tested on a desktop computer with an Intel® Core™ i7-2600 CPU and 8 GB of RAM. Multi-objective joint-inversion is an embarrassingly parallel problem, as the objectives are independent of each other, making it easy to parallelise the algorithm to increase the performance for future many-objective problems.

Additionally in the case of EM-data, a parallelisation over the frequencies is also possible to further reduce run times.

The inversion runs for this study had run times of 1–20 min for 100000–250000 solution evaluations. General run time analysis for MOEAs has been performed (Laumanns et al., 2004), but precise run time predictions are difficult as they are highly problem dependent. The run times are dependent on the number of objectives and the degree of compatibility between the objectives, as compatible objectives make it easier to find well fitting solutions and therefore show accelerated convergence. The adaptive nature of the “Borg” algorithm underlying MOJO makes run time predictions especially difficult, as the variable population and archive sizes and the search restarts performed to mitigate search stagnation can not be projected.

3.6 Conclusion

Multiple approaches to joint inversion modelling of geophysical data exist, but the application of evolutionary algorithms is not common in this field. The ability to jointly invert a number of data sets without the need for data weighting, while providing model uncertainty and data compatibility information makes multi-objective approaches advantageous over conventional linearised schemes.

We have developed and implemented MOJO, a Pareto-optimal multi-objective inversion algorithm for the analysis of geophysical data. The actual modelling steps involved can utilise existing forward calculation algorithms and software. Hence, MOJO is not restricted to specific types of data sets.

The use of an evolutionary algorithm allows the evaluation of a distribution of solution models. This distribution can be analysed with regard to the physical implications of the model parameters and with respect to the quality of the data. Potential contained ambiguities and resolution restrictions of the data can be expressed in terms of data set compatibility. We have presented a scheme to effectively assess this compatibility as part of MOJO. This analysis can be applied independent of the actual modelling part, and can be combined with other (multi-objective) inversion and mod-

elling software to independently assess data quality. This can improve the overall data and model interpretation, and therefore is a valuable addition to the general toolbox for geophysical data inversion modelling.

We have demonstrated the capabilities of MOJO by applying it to synthetic data. The data have been chosen to be able to prove the concepts of the algorithm in a controlled environment. By defining different objective functions the application of MOJO to other data sets, both synthetic and real, is a straight forward process and does not require major alterations to be made to the code. However, in this publication we have focused on the introduction of MOJO and proving its general functionality in a feasibility study. The detailed evaluation for other data types and real data is not within the scope of this study and is part of further research.

Acknowledgments

We thank the developers of the “Borg” Algorithm David Hadka and Patrick Reed from the Pennsylvania State University, for making their algorithm available to us (<http://borgmoea.org>). The work has been supported by the Deep Exploration Technologies Cooperative Research Centre whose activities are funded by the Australian Government’s Cooperative Research Centre Programme. This is DET CRC Document 2015/627.

CHAPTER
FOUR

PARAMETER STUDIES OF GEOPHYSICAL
JOINT INVERSION MODELLING - USING
MULTI-OBJECTIVE OPTIMISATION

SEBASTIAN SCHNAIDT^{1,2}, LARS KRIEGER² AND GRAHAM HEINSON²

¹Deep Exploration Technologies Cooperative Research Centre,
Adelaide Airport SA 5950, Australia

²Electrical Earth Imaging Group, Department of Earth Sciences,
School of Physical Sciences, University of Adelaide, Adelaide SA 5005, Australia

Submitted to *Geophys. J. Int.* on April 24th, 2015,
but not accepted for publication as of September 10th, 2015.

Statement of Authorship

Title of Paper	Parameter Studies of Geophysical Joint Inversion Modelling - Using Multi-objective Optimisation
Publication Status	<input type="radio"/> Published, <input type="radio"/> Accepted for Publication, <input checked="" type="radio"/> Submitted for Publication, <input type="radio"/> Publication style
Publication Details	Schnaidt, S., Krieger, L., and Heinson, G. (2015). Parameter Studies of Geophysical Joint Inversion Modelling - Using Multi-objective Optimisation. Submitted to Geophys. J. Int.

Author Contributions

By signing the Statement of Authorship, each author certifies that their stated contribution to the publication is accurate and that permission is granted for the publication to be included in the candidate's thesis.

Name of Principal Author (Candidate)	Sebastian Schnaidt
Contribution to the Paper	Designed analysis, performed analysis and interpretation, wrote and edited manuscript and acted as corresponding author
Signature	Date 2015-05-05

Name of Co-Author	Lars Krieger
Contribution to the Paper	Assisted in design of analysis and provided critical manuscript evaluation
Signature	Date 3.5.2015

Name of Co-Author	Graham Heinson
Contribution to the Paper	Supervised development of work and provided manuscript evaluation
Signature	Date 6/5/15

Name of Co-Author	N/A
Contribution to the Paper	N/A
Signature	Date

SUMMARY

MOJO is a data-weighting-free multi-objective joint inversion algorithm that generates a solution ensemble, which is statistically analysed to provide model uncertainty estimates and an assessment of the compatibility of the inverted data sets. This eliminates the risk that incompatible data sets are inverted and model artefacts are introduced. We investigate the parameter dependencies of the compatibility analysis and the model distributions generated by MOJO, and demonstrate how the choice of parameters appropriate to the modelling stage can be utilised to improve the robustness and reliability of the results. Furthermore, the algorithm is tested on two real data case studies to proof its effectiveness under real world conditions. The generated results show good data fits and are consistent with the known geology, and the predicted compatibility relationships are correctly identified. We present an improved workflow that allows for reliable results.

4.1 Introduction

Numerical joint inversion approaches are increasing in popularity (Haber and Oldenburg, 1997; Gallardo and Meju, 2003; Colombo and De Stefano, 2007; Commer and Newman, 2009; Jegen et al., 2009; Moorkamp et al., 2011; Haber and Holtzman Gazit, 2013) and are generally advantageous over single data set inversions. Nevertheless, the conventional joint inversion approach exhibits several shortcomings. Firstly, the objective functions for the different data sets are aggregated into a single joint objective function (De Stefano et al., 2011; Menke, 2012), requiring weighting of the different objectives (Dobróka et al., 1991; Julià et al., 2000; De Nardis et al., 2005; Mota and Monteiro dos Santos, 2006). The lack of standard approaches for choosing the weights bears the risk of biased results (Treitel and Lines, 1999; De Stefano et al., 2011). Secondly, it has to be ensured that the jointly inverted data sets are compatible to be inverted together to avoid significant model artefacts (Moorkamp et al., 2010, Chapter 3). Lastly, conventional inversion approaches optimise just a single solution, which is insufficient for exploring the solution space for geophysical data, as most geophysical methods suffer from high levels of solution non-uniqueness (Muñoz and Rath, 2006; Reading et al., 2011; Menke, 2012).

In Chapter 3 we introduced the multi-objective joint optimisation algorithm MOJO, which represents an approach to solve the problems of conventional joint inversion algorithms. It is based on the “Borg” multi-objective evolutionary algorithm (Hadka and Reed, 2013) and treats each data set as a separate objective, completely eliminating the need for data weighting. The approach uses a genetic algorithm (Holland, 1975) to optimise a population of solutions, which is statistically analysed to infer model distributions and uncertainties, as well as assess the data compatibility. Compatibility between objectives is analysed pair wise by comparing a robust Theil-Sen (Theil, 1950; Sen, 1968) regression of the solution distributions in objective space against an ideal line, which corresponds to the solution distribution of identical and therefore perfectly compatible data. Opening angles γ between the regression and the ideal line of $\gamma < 45^\circ$ indicate compatible objectives, while deviations of $\gamma > 45^\circ$ indicate data incompatibility.

MOJO does not depend on the calculation of parameter gradients and linearisation assumptions, as genetic algorithms are direct search methods (Lewis et al., 2000). Standard linearised approaches (e.g. Tarantola, 2005; Aster et al., 2012) require starting models, and are prone to getting stuck in local minimums. Other than standard modelling parameters, such as the number of free model parameters, MOJO requires only one significant parameter to be user-defined, the ε -box value. The ε -value limits the solution density in objective space, which influences the model distributions as well as the associated data compatibility assessment.

We have demonstrated MOJO’s capabilities with a comprehensive feasibility study on synthetic data (Chapter 3). The compatibility state of the analysed data sets was reliably identified and problems occurred only in isolated cases with very dense solution clustering in objective space, and for incorrect data error estimates. Furthermore, we identified several areas that require further research, such as ways to reduce the influence of differently-scaled misfits on the compatibility measure and investigations into the optimal way to assess the generated model distributions. In addition, MOJO has been extensively tested on synthetic test data. Synthetic data are sufficient for demonstrating the concept, but proving the general applicability of the approach requires tests on real data. Real data usually have more complicated data error distributions than the commonly assumed white noise (Garth and Poor, 1994; Manoj and Nagarajan, 2003), and although the synthetic data have been carefully created, trying to resemble a real world scenario, synthetic models can never simulate the complexity of reality.

In this paper we investigate the effects of the ε -value on the model results and the compatibility measure, and perform a systematic analysis to increase the reliability of the compatibility measure. We will also demonstrate MOJO’s effectiveness in two real data case studies.

4.2 Parameter Analysis

4.2.1 Redefinition of the misfit δ

The MOJO algorithm works on a population of solutions rather than a single solution. This has the advantage that this resulting ensemble can be analysed statistically to provide uncertainty estimates for the model output. The population members are rated by means of *Pareto-optimality* (Edgeworth, 1881; Pareto, 1896) and the best solutions found during the inversion are retained in a solution archive. The solution archive ensures that the principle of *elitism* is followed, which is important for optimisation success (Zitzler, 1999; Zitzler et al., 2000). Previously, we analysed the final archive ensemble based on a modified version of the *ideal point* approach introduced by Kozlovskaya et al. (2007). Weighted averages and the corresponding parameter variances were calculated for the solutions of the final archive, where the weights were calculated with respect to the Euclidean distance between a given N -objective solution vector and an ideal point of $\boldsymbol{\delta}_{\text{ideal}} = (\delta^1, \delta^2, \dots, \delta^N)^T = (1, 1, \dots, 1) = \mathbf{1}$. This point was chosen as the ideal point under the assumption that with correctly estimated data errors the normalised misfit will reach a value of $\delta_i^j = 1$ for the optimal solution. We found that this definition bears an inherent potential to bias results for data sets with incorrectly estimated data errors. To make the ideal point less dependent on the correct estimation of the data errors, we redefine the ideal point as $\boldsymbol{\delta}_{\text{ideal}} = (\min(\delta_i^1), \min(\delta_i^2), \dots, \min(\delta_i^N))$, and normalise the misfits by the minimum reached misfit of each objective:

$$\delta_{i;\text{norm.}}^j = \frac{\delta_i^j}{\min(\boldsymbol{\delta}^j)}. \quad (4.1)$$

4.2.2 The box size parameter ϵ

The population size, as well as the archive size, is variable to adapt to the optimisation problem at hand. Nevertheless, the population and archive sizes are limited, and without active diversity management (Purshouse and Fleming, 2007) there might arise situations where solutions have to be deleted from the archive despite being non-dominated, which causes the al-

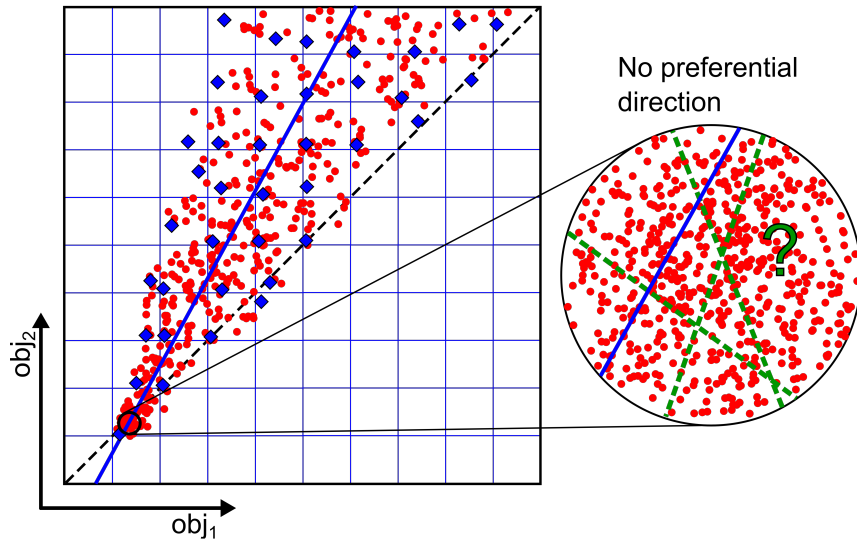


Figure 4.1: Illustration of the effects of the ε -values on the solution distributions in objective space (Section 4.2.2). Smaller ε lead to a high solution density (red), especially in regions of small objective values, whereas a larger ε -grid leads to lower solution density (blue). The solid lines represent potential regression fits corresponding to the solution distributions for small (green) and large (blue) ε -values, and the broken black line represents the ideal line corresponding to perfectly compatible objectives.

gorithm's performance to deteriorate (Hanne, 1999). There are a variety of different ways to control populations diversity, and "Borg" is implemented with a variant of ε -dominance (Hanne, 1999; Laumanns et al., 2002), which discretises the objective space into hyperrectangles (Coxeter, 1973) with side lengths $\varepsilon^j > 0$, $j = \{1, \dots, N\}$. The Pareto-domination criterion is then modified to discrete ε -box dominance, allowing only the best solution out of every ε -box to be stored in the archive (Hadka and Reed, 2013). Thus, the choice of ε^j -values controls the solution density in objective space as well as the population and archive size, with small ε^j -values increasing the solution density and population/archive sizes.

An advantage of MOJO is its ease of use. Unlike many other algorithms MOJO requires very few parameters to be determined by the user. The ε^j -values are the only user determined parameters that significantly influence statistical behaviour.

Figure 4.1 illustrates how the solution density influences the compatibility assessment as well as the generated model distributions for compatible objectives. Solutions found early in the inversion process generally have higher misfits, but for compatible objectives the misfits are quickly reduced.

During search progression the solutions converge towards the optimal solution and the achievable reduction in misfit per search step decreases, resulting in a denser solution distribution. The smaller the ε -boxes are, the denser the solution distributions can become near the optimal solution, creating an imbalance in the solution density between the areas of larger misfits and smaller misfits. This dense clustering around the optimal solution is desirable in the model analysis stage, but can lead to misleading results from the unweighted Theil-Sen estimator. This is caused by the fact that the shape of the distribution close to the optimal solution is dominated by small-scale differences, at or below the noise level, rather than the compatibility relation between the data. Hence, in the compatibility assessment phase of the inversion process larger ε -values make the assessment more robust. In the model distribution analysis phase smaller ε -values are advantageous, as we want to analyse the model distribution around the optimal solution.

For incompatible objectives there exists no common optimal solution fitting all objectives simultaneously. Thus, no dense solution clustering in a single area of objective space can occur, making the compatibility assessment of incompatible robust against the choice of ε -value.

4.2.2.1 The ε -value dependent compatibility measure

In Chapter 3 all inversion runs were performed with $\varepsilon = 5 \cdot 10^{-4}$, as empirical tests showed this to yield good model outputs. Furthermore, the analysis was done on non-normalised misfit values. It was demonstrated that the Theil-Sen based compatibility assessment is generally robust, even in presence of white noise.

Nevertheless, cases with high solution density around the optimal solution can make the compatibility measure less reliable. Larger ε -values reduce the solution density and lessen the influence of high density clusters, allowing for a more robust identification of the compatibility state.

We demonstrate this using the example of the synthetic 10/5-case presented in Chapter 3, a situation in which compatible data sets were wrongly identified as incompatible. The two data sets used are both synthetic mag-

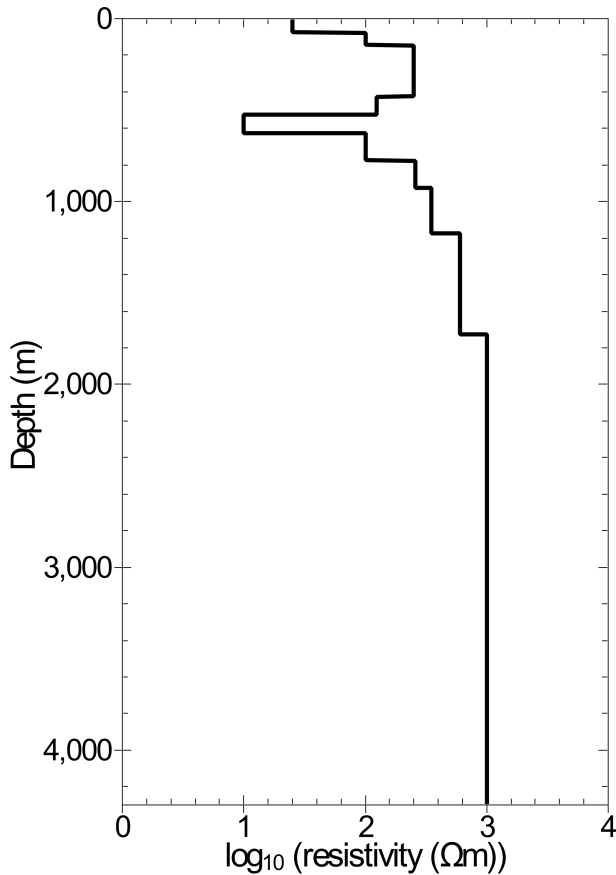


Figure 4.2: The true synthetic model for the 10/5-case (Section 4.2.2.1).

netotellurics (MT) data sets created from the same model (Figure 4.2), simulating audiomagnetotellurics (AMT) data (128–32768 Hz) and broadband (BB) MT data (6–1448 Hz). The two data sets have different levels of random Gaussian noise added. The BB MT data have white noise with a standard deviation equivalent to 3 % of the impedance tensor amplitude added. On the other hand, the AMT data were designed to simulate data with underestimated errors: 10 % white noise was added, but only 5 % errors assigned. The opening angles for the solution ensembles from different stages of the inversion run ranged from $\gamma = 56^\circ$ to $\gamma = 61^\circ$, identifying the objectives as incompatible.

To test the effects of different ε -values on the compatibility measure we performed MOJO inversion runs with the same data sets for 200000 solution evaluations and identical ε -values for all objectives ranging from $\varepsilon = 10^{-1}$ to $\varepsilon = 10^{-5}$.

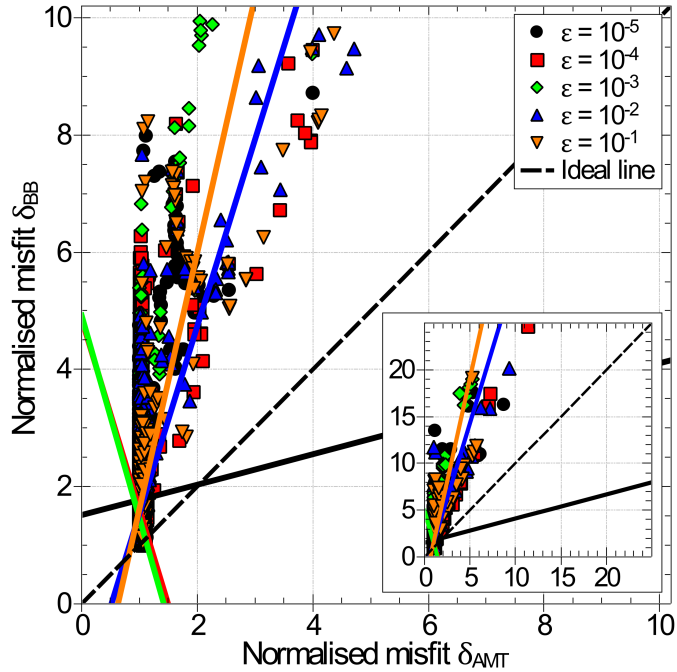


Figure 4.3: Comparison of the solution distributions and corresponding Theil-Sen regressions for inversion runs of the 10/5-case for ε -values of $\varepsilon = 10^{-1}$ (orange), $\varepsilon = 10^{-2}$ (blue), $\varepsilon = 10^{-3}$ (green), $\varepsilon = 10^{-4}$ (red), and $\varepsilon = 10^{-5}$ (black) (Section 4.2.2.1). Note that the green and red regression lines are almost identical. The dashed line represents the ideal line.

Figure 4.3 displays the solution distributions for different ε -values. The distributions show similar patterns with a strong asymmetry towards higher BB MT misfits which is caused by the different frequency content and hence different penetration depth of the two data sets. The larger penetration depth of the BB MT data leaves it partially unconstrained by the AMT data and therefore allows for a wider range of BB MT misfits. The Theil-Sen analysis (Table 4.1) shows that the objectives are identified as compatible for ε -values of $\varepsilon = 10^{-1}$ and $\varepsilon = 10^{-2}$, with opening angles ranging from $\gamma = 21^\circ$ to $\gamma = 37^\circ$. For smaller ε -values opening angles of $\gamma < 45^\circ$ are achieved for only a few individual cases and the values are generally pointing towards incompatible objectives, reaching opening angles of up to $\gamma = 89^\circ$.

We also performed the compatibility analysis with varying ε -values for all test cases presented in Chapter 3 and cases that had been identified correctly previously were reliably identified across all tested ε -values.

Table 4.1: Analysis of the deviation from the ideal line for MOJO runs with varying ε -values for the 10/5-case (Section 4.2.2.1). The analysis is performed for archives at different stages of the inversion run, as well as for all extracted archive members combined.

Solution evaluations	ε -values				
	10^{-1}	10^{-2}	10^{-3}	10^{-4}	10^{-5}
1000	21°	34°	52°	53°	72°
10000	37°	28°	5°	20°	54°
100000	26°	25°	60°	61°	89°
200000	30°	26°	56°	53°	59°
Combined	32°	28°	61°	62°	30°

Concluding, larger ε -values increase the reliability of the compatibility analysis and should be employed in the compatibility assessment stage of the inversion process.

4.2.2.2 The effects of the ε -value on the model distribution

The ε -values and therefore the solution density will also influence the model results. For the model creation stage smaller ε -values beneficial as they permit for a higher solution density, which allows for a more detailed exploration of the parameter space around the optimal solution. Previously, we used averages to analyse the model distributions (Chapter 3). These have the disadvantage that they only yield accurate results if the parameters are distributed close to a normal distribution. When analysing results from inversions with multiple objectives they are not guaranteed to be normally distributed and could exhibit multi-modal distributions, especially for data sets that are not fully compatible. Hence, in the remainder of this paper we will display the complete model distributions as these yield a more complete picture of the model results and the associated parameter uncertainties.

We will demonstrate the benefits of smaller ε in the model creation stage using the same example as before. Figure 4.4 shows the model distributions and the best model for the 10/5-case for $\varepsilon = 10^{-1}$, $\varepsilon = 10^{-3}$, and $\varepsilon = 10^{-5}$ in comparison with the true model. It is apparent that all distributions recover the the main features of the true mode, showing a low-resistivity anomaly between 400–1000 m. For $\varepsilon = 10^{-1}$ and $\varepsilon = 10^{-3}$ distributions can

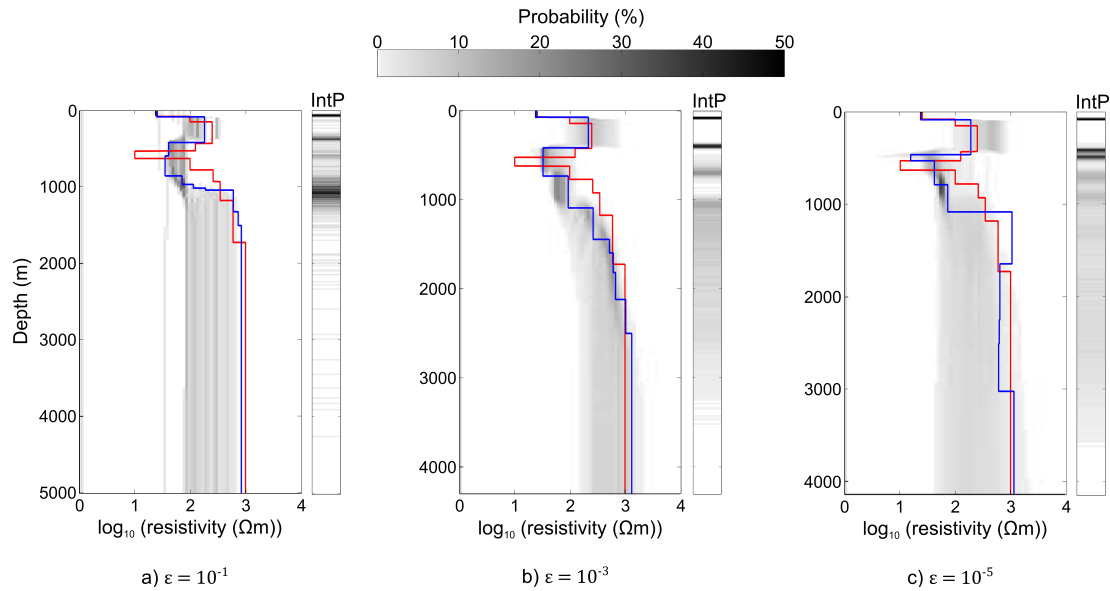


Figure 4.4: Model distributions of the archive solutions for inversion runs of the 10/5 case for ε -values of a) $\varepsilon = 10^{-1}$, b) $\varepsilon = 10^{-3}$, and c) $\varepsilon = 10^{-5}$ (Section 4.2.2.2), expressed as resistivity value probabilities and interface probabilities (IntP). The solid red line marks the true model and the solid blue lines represent the respective best solutions.

not individually resolve the small-scale low-resistivity anomaly at a depth of 500–600 m, but create a thicker anomaly with a conductance corresponding to the conductance of the same depth range in the true model.

The model distribution of the solutions from the $\varepsilon = 10^{-3}$ MOJO run (Figure 4.4 b) is closer to the true model than for $\varepsilon = 10^{-1}$ and exhibits less variability at depth larger than 1000 m. The low-resistivity anomaly is better resolved than before, but the thickness is still overestimated.

For $\varepsilon = 10^{-5}$ (Figure 4.4 c) some of the final archive solutions recover the low-resistivity anomaly with roughly the correct resistivity and with the correct layer thickness. However, the model distribution for $\varepsilon = 10^{-5}$ exhibits a slightly higher variability at depths than the model distribution for $\varepsilon = 10^{-3}$.

The depths of 0–1000 m roughly correspond to the depth range that is constraint by the AMT as well as the BB MT data. Below 1000 m the model is constraint by the BB MT data only and shows increasing variability in the distribution, indicating elevated uncertainty.

In summary, lower ε -values are to be used in the model generation stage, as the higher solution density generates model distributions closer to the true model.

4.2.3 Model distribution analysis

Up to this point we have only looked at the model distributions of the complete solution archives, which give an important overview of the range of parameters reached. Nevertheless, it is not an ideal representation of the optimal model range, as it includes all non-dominated solutions regardless of the reached objective misfits. Due to the way Pareto-optimality is defined the final archive includes a variety of extremal solutions, which only fit some of the objectives satisfactorily, and solutions that are physically improbable, such as solutions with very little parameter variation, which dominate the roughness/regularisation objective. Even though we are trying to avoid general weighting of the objectives we are still looking for solutions that can simultaneously fit all objectives to a satisfactory level. Hence, it is advantageous to analyse a smaller subset of the complete archive. As an example we will analyse subsets of the final archive corresponding to the 10 % solutions closest to the ideal point (Section 4.2.1), as well as the best 10 % solutions for each individual objectives. Analysing the distributions with respect to the individual objectives can yield valuable additional information, such as the varying depth of investigations of the different objectives, which we will demonstrate using the data example from the previous sections. Depending on the individual inversion problem and the particular solution distribution, the percentage of solutions analysed can be adjusted.

Figure 4.5 shows the model distributions for the complete final archive and various subsets of the archive. The archive subset model distributions generally show better defined distributions than the complete archive and are closer to the true model. This is especially true for model depths of more than 1000 m, where the complete archive distribution shows a high variability in the parameter values, whereas the distribution of the 10 % best solutions, and the best 10 % solutions with respect to the BB MT objective show lower variability. The exception is the distribution of the

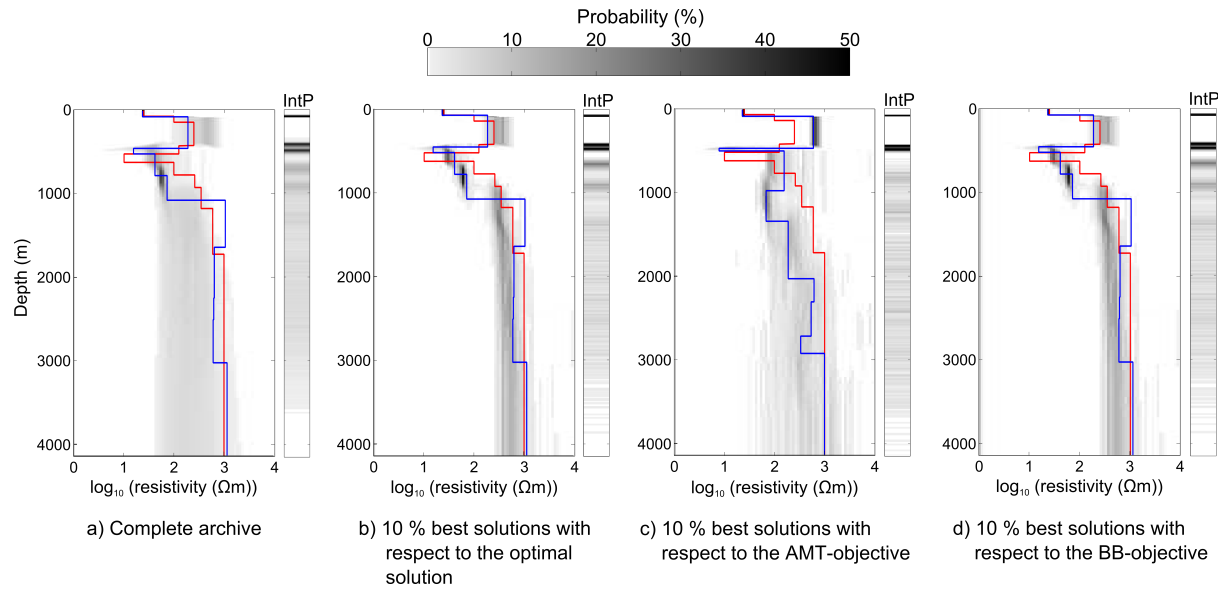


Figure 4.5: Model distributions of different subsets of the final archive of the $\varepsilon = 10^{-5}$ run of the 10/5-case (Section 4.2.3), expressed as resistivity value probabilities and interface probabilities (IntP). The solid red line marks the true model and the solid blue lines represent the respective best solutions.

best 10 % solutions with respect to the AMT-objective. This distribution shows high parameter variability below a depth of about 600 m, due to the limited penetration depth of the higher-frequency AMT data. Analysis of the archive solutions with respect to the two individual objectives illustrates that the lower part of the model is mainly constrained by the BB MT objective and would not be recovered with only the AMT data.

Analysing the distributions with respect to the individual objectives can be especially helpful in the identification of incompatible objectives. Considerable variation between the model distributions with respect to the individual objectives can indicate data incompatibility as the following extreme example with two incompatible BB MT objectives demonstrates. The data sets have the same characteristics as the BB MT data set in the 10/5-case (Section 4.2.2.1) and are based on the two incompatible models α -model and ω -model shown in Figure 4.6. Figure 4.7 shows the model distributions based on the complete archive (Figure 4.7 a), the α -objective (Figure 4.7 b), the ω -objective (Figure 4.7 c). It is apparent that the distributions with respect to the individual archives clearly differ from each other, with the distribution with respect to the α -objective tending towards lower resistivities, whereas the the ω -objective distribution tends towards higher

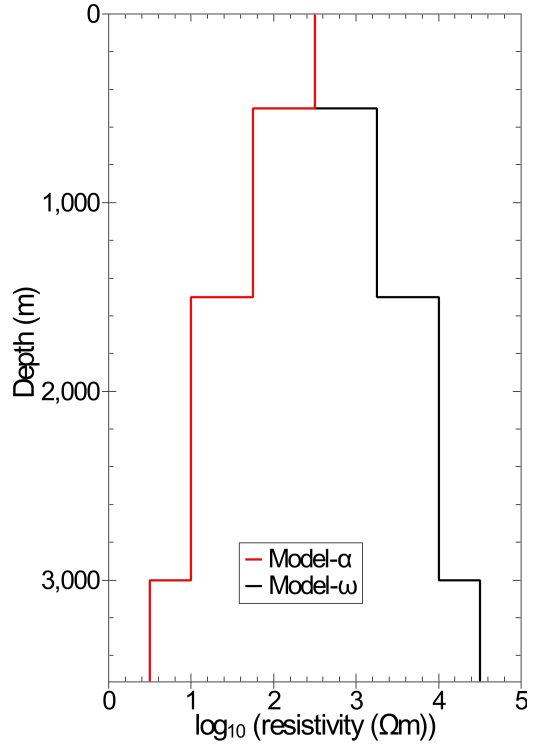


Figure 4.6: The synthetic 3-layer models Model- α (black) and Model- ω (red) used to simulate incompatible data (Section 4.2.3).

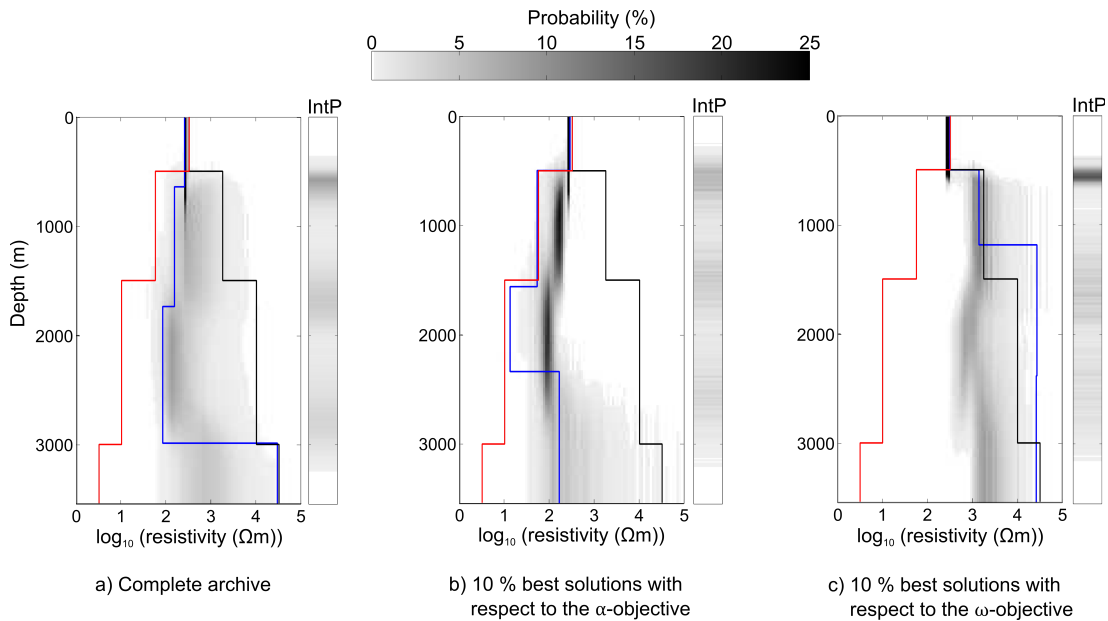


Figure 4.7: Model distributions of different subsets of the final archive of the $\varepsilon = 10^{-5}$ run of the synthetic incompatible test case (Section 4.2.3), expressed as resistivity value probabilities and interface probabilities (IntP). The solid red (α -model) and black (ω -model) lines mark the true models and the solid blue lines represent the respective best solutions.

resistivities. The individual best solutions are close to the two true models; the best solution with respect to the α -objective is close to the true model down to a depth of about 2330 m. Below this depth the model deviates from the true solution as the stronger attenuation of the EM-signal by the lower resistivity structures reduces the effective depth of investigation of the α -objective data. This information can not be recovered from the distribution of the complete archive, which is dominated by the α -objective, but does not show any multi-modality. The domination by the α -objective is caused by the fact that MT measurements are more sensitive to low resistivities than to high resistivities (Chave and Jones, 2012). This highlights the importance of analysing the model distributions with respect to the individual objectives in addition to the complete model distributions.

4.3 Application to Real Data

We present a data set from the Cooper Basin in South Australia, consisting of two BB MT data sets and a resistivity well-log; and a data set from the Eromanga Basin in Queensland, Australia, consisting of two collocated AMT and BB MT stations.

The phase tensor approach (Caldwell et al., 2004) was used to ensure that the data were consistent with a 1-D layered model approach to avoid biasing the model output by including higher-dimensional data. The ellipticity λ of the phase tensor is an indicator for the dimensionality of the data (Bibby et al., 2005). We analysed the phase tensor ellipticity for all MT data (Krieger and Peacock, 2014) and classified all data points with an ellipticity larger than 0.1 as non-1-D. These data points were omitted from the processing. In addition the effects of deviations from the 1-D assumption and noise influences can be decreased by inverting the arithmetic mean of the off-diagonal elements of the impedance tensor, the so called Berdichevskiy invariant (Berdichevskiy and Dmitriev, 1976; Moorkamp et al., 2010).

All inversions were run for 200000 solution evaluations and both sets of data were inverted twice with different ε -values. The first inversion for each set of data was performed with $\varepsilon = 10^{-1}$ to analyse the data compatibility, and the second inversion with $\varepsilon = 10^{-5}$ for the model output analysis stage.

Before the main inversion runs several test runs were performed to determine the number of model layers that are required to successfully model the data. Applying the principle of Ockhams Razor (Thorburn, 1918; Constable et al., 1987) we use the least amount of layers needed to sufficiently predict the data. Allowing for too many layers would yield unnecessarily complex models and can lead to a decoupling of the jointly inverted data sets (Moorkamp et al., 2010). Following this analysis the Cooper Basin data is inverted with a 10 layer model and the data from the Eromanga Basin is inverted with a 20 layer model.

4.3.1 Cooper Basin, South Australia

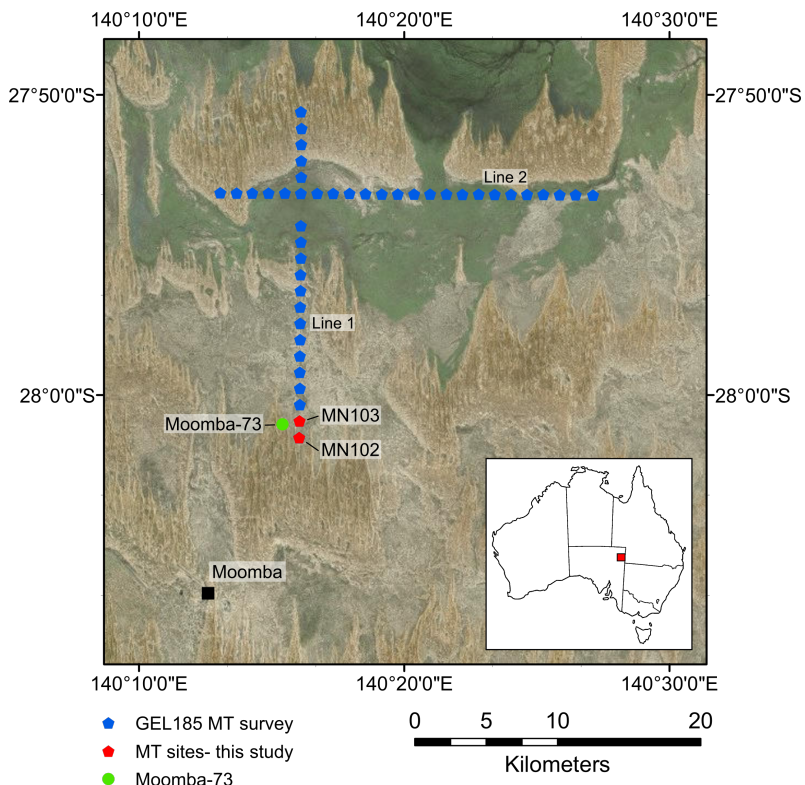


Figure 4.8: Locations of the GEL 185 MT survey lines, including the sites MN102 and MN103 used in this study, and the Moomba-73 well (Section 4.3.1).

The data is from the Cooper Basin, near Moomba in South Australia (Figure 4.8), where the top formation is comprised of the Lake Eyre Basin,

which overlays the Eromanga, Cooper, and Warburton Basin (Apak, 1994; Sun, 1997).

The Moomba data consist of two broadband MT data sets “MN102” and “MN103” of the 2008 GEL 185 grid of the Cooper MT project (Stockill, 2008) and resistivity well-logs of the Moomba-73 gas appraisal well (Santos Ltd, 1994).

These responses were chosen as a case for which the compatibility relationships between all data sets is not completely known, but various reference material exist against which the results can be compared to. Geological control is provided by the well completion report (Santos Ltd, 1994) and the resistivity models can be compared against existing 2-D resistivity models of the region (Murray, 2012).

The Moomba North Line 1 of grid GEL 185 consists of 21 sites with MN102 and MN103 being the two sites closest to Moomba-73, with distances of 1070 m and 1250 m respectively (Figure 4.8). Most MT data points of frequencies lower than 0.32 Hz violate the 1-D assumption and are omitted. The 1-D assumption is satisfied by 26 data points in a frequency range of 0.002–238 Hz for MN102, and for 24 data points in a range of 0.15–238 Hz for MN103. The MT data show very similar patterns and trends across all site (Stockill, 2008, appendix C), hence the two data sets are expected to show high compatibility.

The well-log covers a depth range of 1729–3051 m, with a sample spacing of 0.15 m. A shallow later log (LLS) as well as a deep later log (LLD) are available, which are both tested against the MT data.

MT data does not have the resolution to resolve 0.15 m samples, thus, 50 m moving boxcar averages of the two logs are used as the input for the joint inversion.

4.3.1.1 Compatibility analysis

The compatibility between the three objectives is analysed pairwise for each of the three possible unique objective combinations. We perform this analysis twice, first for the combination of MT data and the LLS, and again with the LLD.

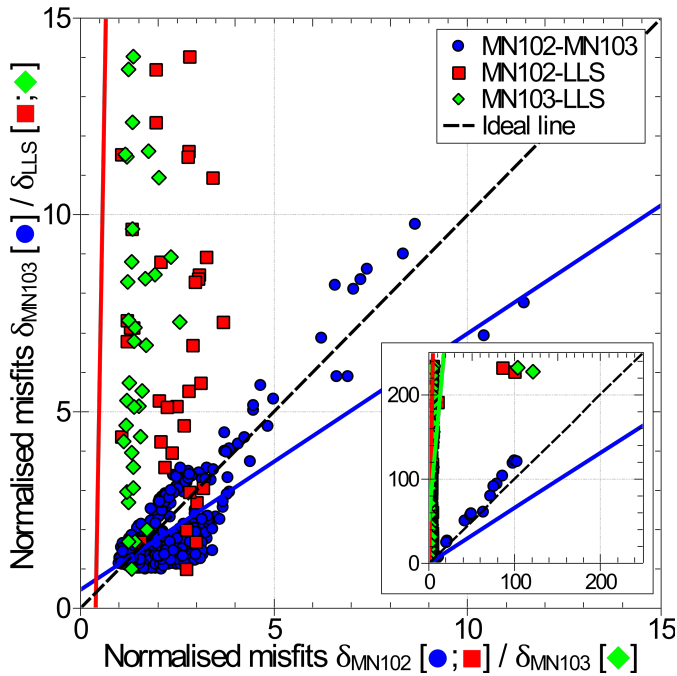


Figure 4.9: Solution distributions for the MN102-MN103-objective (blue), MN102-LLS-objective (red), and MN103-LLS-objective (green) and the corresponding Theil-Sen regressions (solid lines) (Section 4.3.1.1). The dashed line represents the ideal line.

The resulting solution distributions for the two cases show almost identical patterns. Figure 4.9 exemplarily shows the solution distribution for the combination of MN102, MN103 and LLS (Figure A.1 for the LLD-case). A high degree of compatibility between the two MT data sets is indicated in both cases, with the deviation angles for the combined archive solutions reaching values of $\gamma_{\text{MN102-MN103}} = 12^\circ$ in the LLS-case and $\gamma_{\text{MN102-MN103}} = 9^\circ$ in the LLD-case (Tables 4.2 and 4.3). These small deviation angles are to be expected as the two data sets are in good accordance to each other and have similar frequency ranges.

For all four objective combinations involving one of the two resistivity well-logs the distributions of the combined archive solutions exhibit similar deviations from the ideal line of $\gamma = 40^\circ$ to $\gamma = 44^\circ$. These values close to the compatibility threshold indicate that the MT data and the well-logs are not incompatible, but also the MT data does not require the features represented in the well-logs to reach acceptable misfits. For different models producing similar misfits for the MT data the misfits of the well-log objectives can take on vastly different misfit values (Figures 4.9 and A.1).

Table 4.2: Analysis of the deviation from the ideal line for the objective combinations MN102-MN103, MN102-LLS, and MN103-LLS (Section 4.3.1.1). The analysis is performed for archives at different stages of the inversion run, as well as for all extracted archive members combined.

Solution evaluations	Deviation angles		
	MN102-MN103	MN102-LLS50	MN103-LLS50
1000	27°	87°	90°
10000	15°	42°	42°
100000	2°	45°	45°
200000	30°	18°	37°
Combined	12°	44°	40°

Table 4.3: Analysis of the deviation from the ideal line for the objective combinations MN102-MN103, MN102-LLD, and MN103-LLD (Section 4.3.1.1). The analysis is performed for archives at different stages of the inversion run, as well as for all extracted archive members combined.

Solution evaluations	Deviation angles		
	MN102-MN103	MN102-LLD50	MN103-LLD50
1000	8°	67°	63°
10000	24°	67°	57°
100000	21°	46°	45°
200000	31°	76°	47°
Combined	9°	41°	44°

Generally, the deviation angles for objective combinations involving the LLD exhibit higher values than objective combinations including the LLS. This could indicate that the features of elevated resistivity between 2480–2780 m are not supported by the MT data, as these features are the only significant difference between the two resistivity well-logs.

4.3.1.2 Model distributions

Figure 4.10 shows the model distributions for the MOJO run involving the LLS log. The displayed model subsets correspond to the subsets that have been identified as the most useful in analysing the results of a MOJO run (Section 4.2.3). The model distributions for the runs involving the LLD log are displayed in Figure 4.11. In this case only the distributions of the full archive and the top 10% best solutions with respect to the best found model are displayed, as the distributions are very similar to the LLS case.

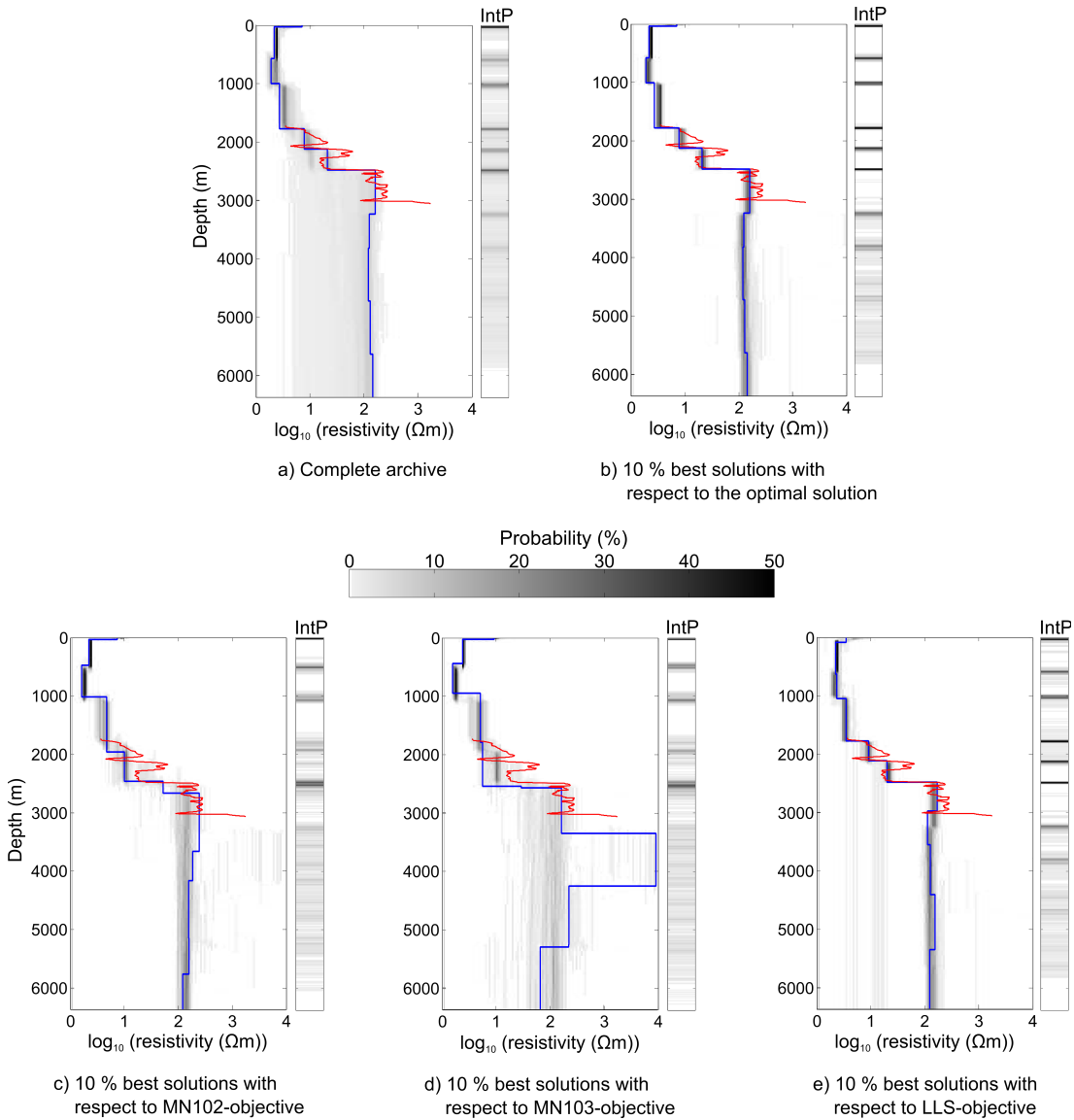


Figure 4.10: Model distributions of different subsets of the final archive generated from the joint inversion of the data sets MN102, MN103, and LLS (Section 4.3.1.2), expressed as resistivity value probabilities and interface probabilities (IntP). The solid red line shows the LLS log (50 m moving boxcar average) and the solid blue lines represent the respective best solutions.

All distributions for both cases show a similar general trend. The distributions indicate a top layer of about 50 m thickness with a resistivity of $10 \Omega\text{m}$. Down to a depth of about 1000 m the resistivity decreases reaching values around $2 \Omega\text{m}$. This is followed by a gradual increase in resistivity to a depth of 2500 m, reaching values around $200 \Omega\text{m}$, which is followed by a slight decrease in resistivity to around $150 \Omega\text{m}$. The distributions generally show little variability, indicating low uncertainty. Slightly elevated levels

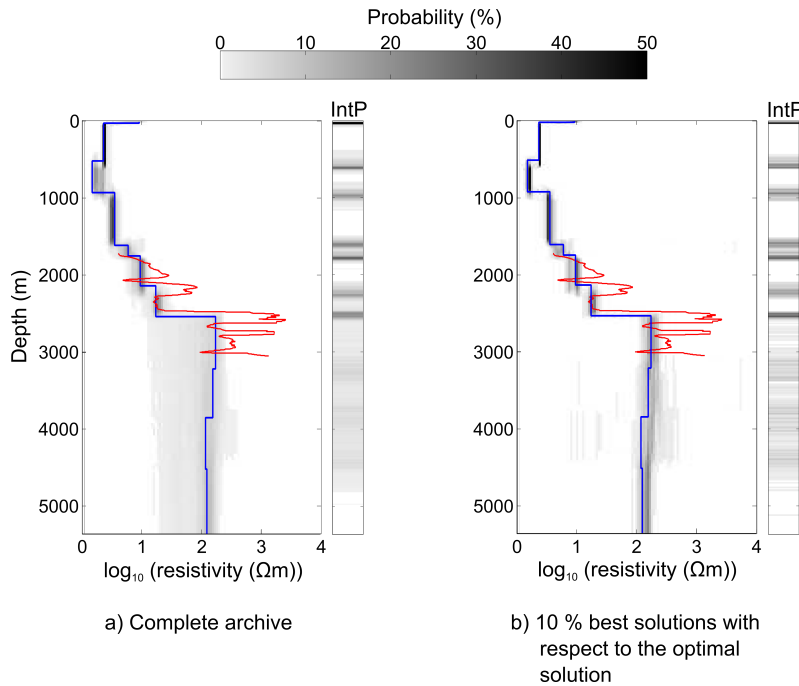


Figure 4.11: Model distributions for the complete archive and the top 10% solution with respect to the best solution generated from the joint inversion of the data sets MN102, MN103, and LLD (Section 4.3.1.2), expressed as resistivity value probabilities and interface probabilities (IntP). The solid red line shows the LLD log (50 m moving boxcar average) and the solid blue lines represent the respective best solutions.

of variability can be observed at depths greater than 2500 m for the distributions of the complete archive and the best 10% solutions with respect to the MN103-objective. This is likely caused by the fact that the MN103 data does not have data points with frequencies as low as the MN102 data, and therefore the MN103 data might lack sensitivity at depth.

The general trend of the well-log is recovered by the models, but small scale features can not be resolved by the MT data. The high resistivity features present in the LLD log are not recovered.

Comparing the apparent resistivities and phase values for the measured data with the values calculated from the best models for both resistivity logs shows that the general pattern is reproduced by the model data and the values are inside the data error estimates for most frequencies (Figure 4.12), with the modelled responses showing a flatter profile than the measured responses. The generated models are also capable of satisfactorily fitting most of the data points that have been omitted for violations of the dimensionality assumption. To check if the imperfections in the fit are an

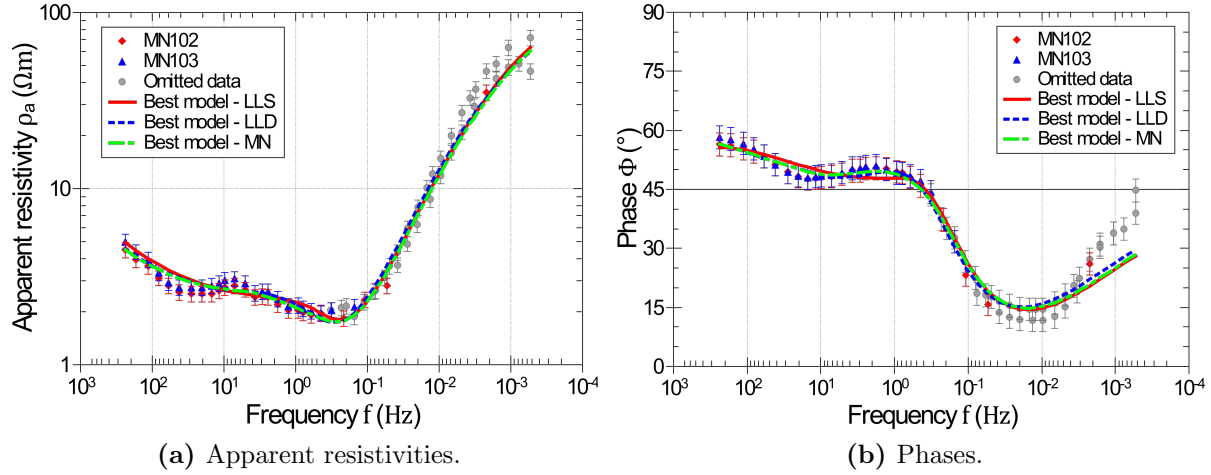


Figure 4.12: Model responses for the optimal solution generated from the joint inversion of the data sets MN102, MN103, and LLS (red line); MN102, MN103, and LLD (blue line); and MN102 and MN103 (green line) compared to the measured responses (Section 4.3.1.2). The a) apparent resistivities are presented in the left panel and the b) phase values are presented in the right panel.

effect of the inclusion of the well-log data, we perform an additional inversion run with just the two MT data (Figure A.2 for the solution distribution of the MT-only case and Table A.1 for the corresponding deviation angles).

Figure 4.12 also shows the measured responses compared against the modelled responses using just the MT data. These responses are almost identical to the runs including well-log data and no significant improvement is achieved. The model distribution of the MT-only run shows a similar trend to the previous results, with decreasing resistivities down to a depth of about 800 m and a gradual increase in resistivity with depth (Figure 4.13). The MT-only distributions generally show slightly lower resistivities than the inversions involving well-log data and the increase in resistivity with depth is slower for the MT-only inversion. The maximum resistivity of about $130 \Omega\text{m}$ is reached at a depths between 4000 m and 5000 m, as compared to 2500 m for the well-log cases.

4.3.1.3 Interpretation

The model distributions created with MOJO are consistent with the 2-D inversion result of the complete Moomba North MT line from (Murray,

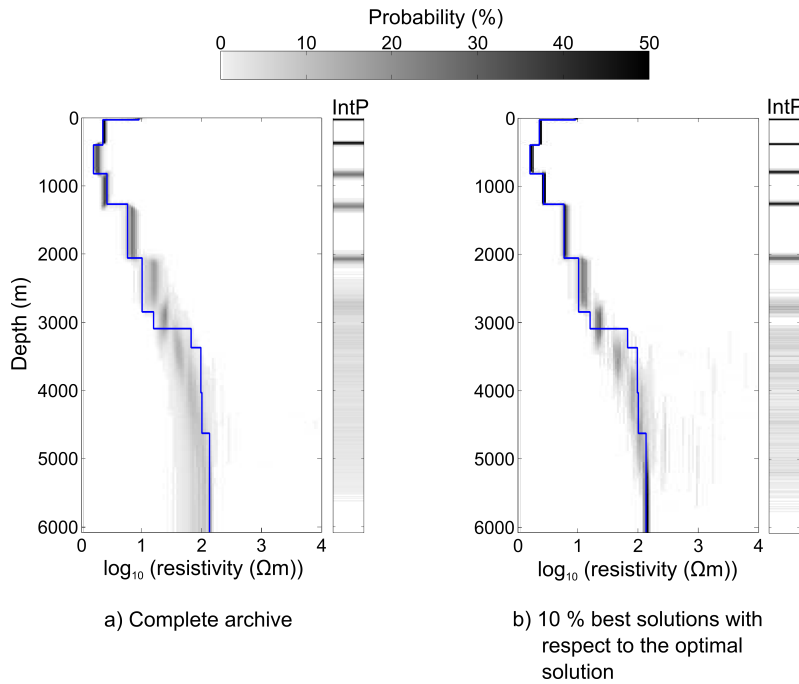


Figure 4.13: Model distributions for the complete archive and the top 10 % solution with respect to the best solution generated from the joint inversion of the data sets MN102 and MN103 (Section 4.3.1.2), expressed as resistivity value probabilities and interface probabilities (IntP). The solid blue lines represent the respective best solutions.

2012, pp. 18–20). The low resistivity zone in the top 1000 m corresponds to the recent to late Cretaceous surficial and Winton formations identified in the Moomba-73 well-log (Santos Ltd, 1994, appendix I), which consists of mostly loosely grained sand- and claystone. The high porosity of this formation equates to low resistivities.

The subsequent increase in resistivity is consistent with the reduction in porosity due to increasing rock matrix compaction and consolidation (Smith, 1971). The high resistivities in the depth range of about 2500–3050 m are consistent with the various formations containing several layers of coal as well as various gas holding layers (Santos Ltd, 1994, pp. 12–19 and appendix I). The MT data do not recover these features, especially with respect to the LLD log, which indicates that there is no information of these features present in the MT data. This is caused by the fact that MT is more sensitive to low resistivity features than to high resistivity features (Chave and Jones, 2012) and/or that the features causing the high resistivities do not extend all the way to the area of the MT sites.

The basement can be observed with a resistivity of around $150 \Omega\text{m}$ at a depth of about 4,500 m, indicated by the decrease in parameter variability (Figures 4.10, 4.11, and 4.13).

The well-log identifies a large number of small scale stratigraphic features (Santos Ltd, 1994, pp. 10–20 and appendix I), indicating that undetected violations of the dimensionality assumption are the likely cause of the deviations in the fit of the MT responses (Figure 4.12).

4.3.2 Isa Extension MT survey

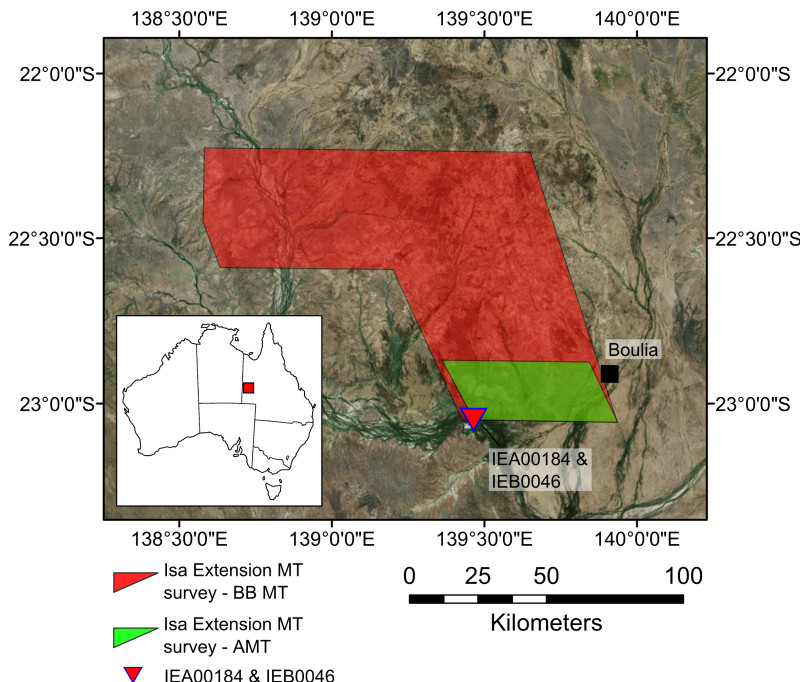


Figure 4.14: Location of the Isa Extension MT survey and the sites IEA00184 and IEB0046 used in this study (Section 4.3.2).

The two MT data sets in this example are collocated and are part of the Isa Extension MT survey¹, which consists of a total of 942 AMT sites and 812 BB MT sites (Figure 4.14).

The two sites are located about 265 km South of Mount Isa, Queensland, Australia and about 48 km west-south-west from Boulia, Queensland, Australia. The site location is in the Eromanga Basin, a sub-basin of the Great

¹supplied by the Department of Natural Resources and Mines of the Geological Survey of Queensland

Artesian Basin (Habermehl, 1980; Ransley and Smerdon, 2012), close to the edge of the Georgina Basin, which overlay the Mount Isa Province (Jell, 2013). No additional geophysical data is (freely) available in the vicinity.

These data sets were chosen as most of their data points comply with the 1-D assumption and objective compatibility is almost guaranteed due to the fact that the data were recorded at the exact same location. Hence, this test will show if MOJO can correctly identify the compatibility state for real data, even though no reference data for the region is available at this time.

Most data points with frequencies lower than 40 Hz violate the 1-D assumption. After elimination of the non-1-D data point the AMT data set (IEA00184) consists of 27 data points with a frequency range of 4–9939 Hz. The BB MT data set (IEB0046) consists of 15 data points with a frequency range of 0.013–250 Hz. The responses of the two sets match up seamlessly. Hence, we expect that the data are compatible.

4.3.2.1 Compatibility analysis

As before the first step in the analysis of the data is the compatibility assessment. Table 4.4 displays the deviation angles for archives at different stages of the inversion run. The two data sets are identified as compatible, with deviation angles ranging from $\gamma = 15^\circ$ to $\gamma = 31^\circ$ (Figure A.3 for the corresponding solution distribution).

Table 4.4: Analysis of the deviation from the ideal line and for the Isa Extension case study (Section 4.3.2.1). The analysis is performed for archives at different stages of the inversion run, as well as for all extracted archive members combined.

Solution evaluations	Deviation angles
1000	29°
10000	31°
100000	16°
200000	15°
Combined	18°

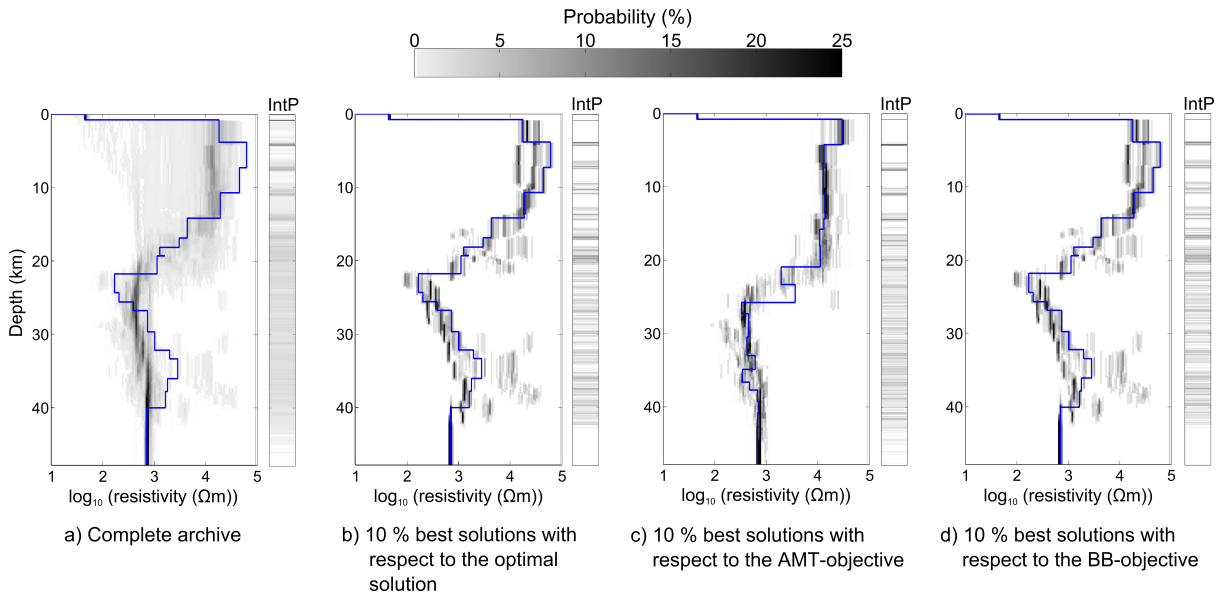


Figure 4.15: Model distributions of different subsets of the final archive generated from the joint inversion of the IEA00184 and IEB0046 (Section 4.3.2.2), expressed as resistivity value probabilities and interface probabilities (IntP). The solid blue lines represent the respective best solutions.

4.3.2.2 Model distributions

The model distribution analysis for the Isa Extension data set is based on 713 solutions of the final archive of a MOJO run with $\varepsilon = 10^{-5}$.

Figure 4.15 shows the model distributions of various subsets of the complete archive. The general model structure is relatively simple. In the first 0.8 km the distribution shows very little variability, reaching a resistivity value of $45 \Omega\text{m}$, which represents the sediment cover in the study area. Below this depth the variability in the distribution increases. The sediment cover is followed by a high resistivity zone down to a depth of about 15 km. The resistivity values reached in this zone are mostly around $12500 \Omega\text{m}$. In the depth range of 1 km to about 4 km some models reach resistivity values of up to $32000 \Omega\text{m}$. Between the depths of 15 km to 20 km the resistivities decrease to around $1000 \Omega\text{m}$. Below that depth the resistivities vary between $250 \Omega\text{m}$ and $1000 \Omega\text{m}$ before converging to about $630 \Omega\text{m}$ from a depth of about 38 km on. From that depth on the distribution exhibits very little variability, indicating low model uncertainty.

The best 10 % solutions with respect to the AMT objective (Figure 4.15 c)) show a very similar model distribution as the complete archive. The difference is that most of these solutions have resistivity values of around $30000 \Omega\text{m}$ from depths of 1 km to 4 km and the decrease in resistivity occurs at a greater depth of about 20 km.

On the other hand the overall best 10 % solutions and the best 10 % solutions with respect to the BB MT objective exhibit similar patterns to each other (Figures 4.15 b) and 4.15 d)), but differ from the complete archive and the best 10 % AMT solutions. The general trend is similar to the other subsets, but the two distributions reach values as low as $100 \Omega\text{m}$ at a depth of about 22–23 km and resistivity values of up to $32000 \Omega\text{m}$ at depths between 30 km and 40 km. The increased variability might be caused by the lower number of data point in the BB MT data set as compared to the AMT data set. The more extreme values at depths of 20–40 km could also be the sign of an oscillation effect that is common in 1-D MT modelling and can indicate that the number of free layers is too high, causing model overfitting (e.g. Constable et al., 1987). It is unsure if that is the case in this instance, as the effect is only observable for the BB-objective and not for the AMT-objective. The similarity between the model distributions of the overall best 10 % solutions and the 10 % solutions with respect to the BB MT objective indicates that the best overall solutions are dominated by the best solutions with respect to the BB MT data. Like the asymmetry in the solution distribution in objective space in the 10/5-case (Section 4.2.2.1), this is caused by the penetration depth of the BB MT data exceeding the penetration depth of the AMT data.

Figure 4.16 shows the comparison of the apparent resistivity and phase values calculated from the measured data with the values calculated from the best model. The modelled values show an almost perfect fit for all frequencies included in the modelling, with the exception of very high frequencies of 3000 Hz and above. These differences at very high frequencies might be caused by small scale anomalies near the surface. The calculated model also shows a close fit for the data points that have been omitted from the data sets for violating the 1-D assumption, down to a frequency of about 0.01 Hz.

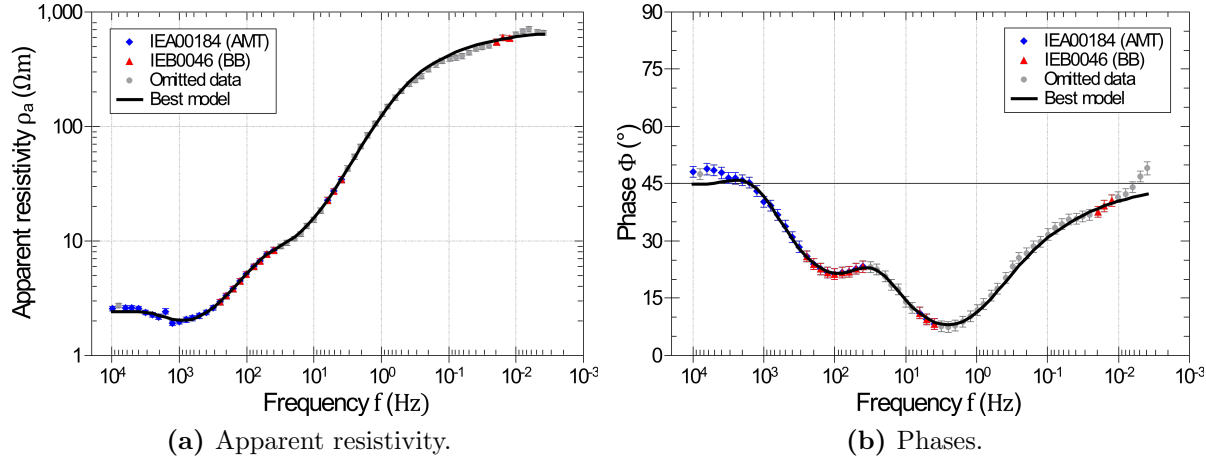


Figure 4.16: The modelled responses of the Queensland data sets compared to the measured responses (Section 4.3.2.2). The a) apparent resistivities are presented on the left and the b) phase values are presented on the right.

4.3.2.3 Interpretation

For the time being there does not exist any resistivity models for the southern part of the Isa Extension MT survey to which we could compare the model distribution generated by MOJO. At this time none of the other sites of this survey have been analysed. The best found model shows a good fit across most frequencies (Figure 4.16). The models show a basin depth of about 800 m to basement. The cover sequence has resistivities of 45 Ωm and lower. The upper crust is 14–19 km thick and shows high resistivities around 30000 Ωm (Section 4.3.2.2). Below that the resistivity decreases with depth. The minimum resistivity of around 170 Ωm is reached between depths of about 22–27 km. This coincides with the seismic Conrad discontinuity in the Eromanga basin (Finlayson, 1983; Finlayson et al., 1984). Following this resistivity decrease the resistivity increases again down to a depth of about 38 km. For deeper regions the model distribution shows very little variability around a resistivity value of 630 Ωm . The depth of 38 km is consistent with the regional Mohorovičić discontinuity depth estimated by seismics (Kennett et al., 2011; Salmon et al., 2013).

The true subsurface structure is likely more complex, especially at depth, as most of the data points with frequencies lower than 40 Hz show 2-D and 3-D dimensionality. For the maximum resistivity of about 32000 Ωm the penetration depth of an electro-magnetic signal with a frequency of 40 Hz

equates to a maximum of 14 km (Simpson and Bahr, 2005). Below this depth the models are constrained by only six data points. Nevertheless, the model distribution generated here can serve as the base for future starting models for 2-D and 3-D inversion models that will be generated from the complete set of survey sites.

4.4 Discussion

We have presented the MOJO multi-objective joint inversion algorithm as a tool for geophysical joint inversion modelling and demonstrated its capabilities in a feasibility study on synthetic data in an earlier publication (Chapter 3).

In this paper we have addressed several of the issues that had previously been identified and have improved the MOJO workflow to yield more robust results. We have tested the influences of the ε -value and investigated the model distribution analysis in more detail.

The solution distributions of compatible objectives can exhibit strange behaviour close to the optimal solution, as the influence of data noise on the objective values increases. This can lead to compatible objectives being misidentified as incompatible in situations with dense solution clustering (Chapter 3). Our tests show that the ε -values has a considerable impact on the compatibility measure as well as the model distribution by controlling the solution density in objective space. Adapting the ε -values appropriately to the modelling stage ensures robust and reliable results.

Larger ε -values limit the number of solutions and reduce the solution density, making the correct identification of compatible objectives more robust. However, incompatible objectives can be reliably identified independently of the chosen ε -values.

MOJO runs with smaller ε -values on the other hand generate ensembles with high solutions density around the optimal solution producing model distributions closer to the true model (Section 4.2.2.2).

Before the analysis relied on the assumption that the misfit of the best solution normalised with the data error would reach a value close to $\delta^j = 1$.

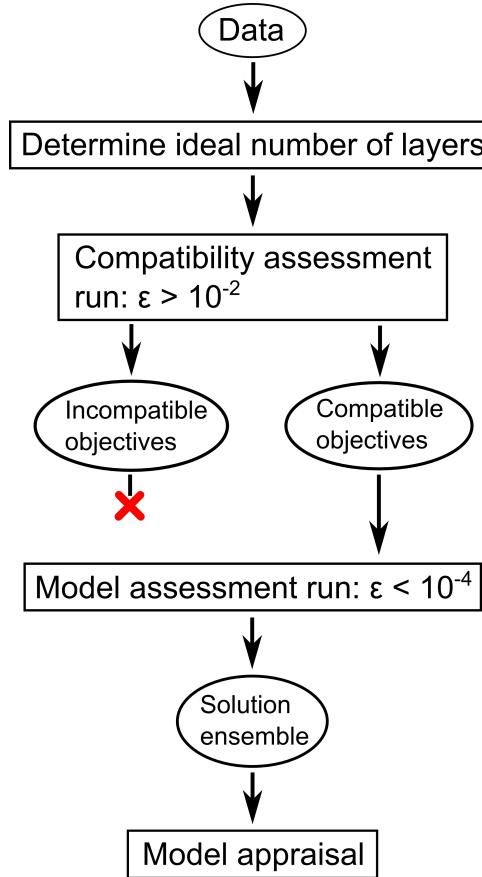


Figure 4.17: Illustration of the different stages of the MOJO workflow (Section 4.4).

Wrongly estimated data errors could mislead the data compatibility assessment (Chapter 3). To reduce the influence of differently scaled objective misfits on the compatibility assessment we normalised all objective values with the minimum reached misfit for each objective (Equation 4.1). Using the misfit normalisation in conjunction with appropriately chosen ϵ -values can greatly improve the compatibility assessment.

The joint inversion and analysis of multiple date sets with MOJO is performed in a three-stage process: the compatibility assessment stage, followed by the solution ensemble creation stage, and the ensemble appraisal stage (Figure 4.17).

In the ensemble appraisal stage it has proven important to examine the complete model distributions rather than averages of the distribution. The calculation of arithmetic mean values assumes close to normally distributed

data, which is not always the case (Section 4.2.3), especially for incompatible objectives, which renders arithmetic statistics invalid.

The display of the complete model distribution is also beneficial, as it directly visualises the model and the model uncertainty, without the need for an additional uncertainty analysis step. Furthermore, the distributions directly show the reached extremal values for the model parameters, indicating the feasible model ranges. This clear and concise presentation of the modelling results allows for an easier interpretation.

We also show that it is beneficial to assess the model distribution of subsets of the final archive containing the best solutions with respect to all objectives as well as with respect to the individual objectives. This eliminates extreme solutions that only fit some of the objectives satisfactory and has proven to yield model distributions that better represent the true models. Analysing the model distributions of just the best solutions is equivalent to analysing how the solutions closest to the optimal point in objective space map into the model parameter space. Multi-modality in the distributions or significantly different distributions for the best solutions with respect to the individual objectives can be an indicator for incompatibility between the objectives, as demonstrated in the incompatible test case in Section 4.2.3 (Figure 4.7).

4.4.1 Case studies

The models generated by the algorithm satisfactorily reproduce the measured data in both cases and are consistent with the local geological information. In case of the Isa Extension MT data the apparent resistivities and phase values calculated from the measured data are almost perfectly reproduced by the best found model, with the exception of slight deviations at very high frequencies (Figure 4.16). Even though the generated model distributions are likely an oversimplified representation of the true subsurface structures, as many low frequency data points have been omitted for violating the 1-D dimensionality assumption, the model represents a background model to the survey area and can be used as a starting model for future 2-D and 3-D inversions.

For the Moomba data the measured MT responses were reproduced to within the estimated error range and the model distributions are consistent with existing resistivity models of the region (Murray, 2012). Yet, the modelled responses showed slight deviations from the measured responses across most frequencies. This is the case for all tested combinations of data, including a test including only the MT data sets (Figure 4.12). A better fit could also not be achieved by allowing for different numbers of model layers or by adapting the error estimates. This indicates that this is caused by violations to the assumptions made, such as the dimensionality of the data or possible anisotropy.

In both cases the MT objectives have been clearly identified as compatible. This was expected, as the data sets show very good accordance with each other over the entire frequency range (Figures 4.12 and 4.16). On the other hand the Moomba objective combinations involving either the LLS or the LLD resistivity well-log exhibit deviation angles of $\gamma = 40^\circ - 44^\circ$, close to the compatibility threshold of $\gamma = 45^\circ$ (Tables 4.2 and 4.3). This means that the well-log objectives can take on very different objective values for solutions that exhibit very similar MT objective values (Figures 4.9 and A.1). This indicates that the well-log objectives are not incompatible to the MT objectives, but the information contained in the well-logs is not essential to fitting the MT data. When jointly inverting just the two MT data sets together the model distribution varies slightly from the cases that involve well-log data, with the MT-only distribution tending towards lower resistivities (Figures 4.10, 4.11, and 4.13). The well-log only covers a depth range of 1729–3051 m, hence the model is not constrained by the well-log in all other regions of the model and it can adapt to fit MT data and well-log simultaneously. It follows that the fact that the models follow the well-log's trend is not a significant indicator that the well-log also represents the ground truth at the locations of the MT measurements.

In cases like this a definitive judgement regarding the compatibility of the objectives can not be given.

4.5 Conclusion

We have investigated the dependencies of the compatibility assessment and the model results on the ε -value and have demonstrated how these dependencies can be utilised to generate more robust and improved results, compared to using a constant ε -value. Larger ε -values reduce the solution density and allow for a more robust data compatibility analysis, while smaller ε -values increase solution clustering allowing for a detailed analysis of how the models parameter vary close to the optimal solution, providing improved model uncertainty estimates.

In addition, we found that a clear and concise way to communicate the results is important to make it easier to reach a well informed decision and ensure correct interpretation of the results.

We have also demonstrated MOJO's applicability under real world conditions. The model distributions generated by MOJO reproduce the measured data in both case studies and achieve good data fits. The results are in agreement with available geological information and existing resistivity models, and the compatibility assessments are consistent with the predicted compatibility relationships.

Acknowledgments

We thank the Geological Survey of South Australia and Betina Bendall, as well as the Geological Survey of Queensland (Department of Natural Resources and Mines) and Janelle Simpson for providing us with the data used in the case studies. The work has been supported by the Deep Exploration Technologies Cooperative Research Centre whose activities are funded by the Australian Government's Cooperative Research Centre Programme. This is DET CRC Document 2015/674.

CHAPTER FIVE

SUMMARY AND CONCLUSION

The main focus of this thesis project was the advancement of uncertainty estimation techniques in geophysical (joint) inversion modelling, while keeping the implementation as simple as possible and the results easy to interpret. This was in an attempt to make the use of uncertainty analysis more common and more accessible.

This problem was approached from two different directions. The bootstrap resampling method provides model uncertainty estimation capabilities for established inversion algorithms, whereas the multi-objective joint optimisation algorithm (MOJO) presents a novel approach to joint inversion modelling, tackling the problems typically faced with common methods.

5.1 Bootstrap Resampling

Commonly used inversion algorithms, such as Occam (deGroot Hedlin and Constable, 1990) and ModEM (Kelbert et al., 2014), only provide a single misfit value in their base configuration as a rating of model quality. Bootstrap resampling can provide qualitative uncertainty estimates for the model parameter magnitudes as well as for the location of model features (Chapter 2). The capabilities of bootstrapping have been demonstrated us-

ing the example of the 2-D inversion code Occam, employing it on synthetic and real MT data.

There exists a variety of methods that can provide similar uncertainty estimates, discussed in Chapter 2, such as MCMC methods based on Bayesian statistics (Gamerman, 1997; Gelman et al., 2003; Aster et al., 2012; Rosas-Carbajal et al., 2014), the most-squares method (Jackson, 1976; Meju and Hutton, 1992; Kalscheuer et al., 2010; Rosas-Carbajal et al., 2014), the model covariance matrix analysis (Meju, 1994; Alumbaugh and Newman, 2000; Tarantola, 2005; Menke, 2012), and null-space projection methods (Deal and Nolet, 1996; Rowbotham and Pratt, 1997; Muñoz and Rath, 2006). Some of these methods, such as the Bayesian MCMC approaches, can provide quantitative uncertainty estimates, but these methods are generally complicated to implement and usually require changes to the inversion algorithm's source code to be made. Furthermore, the implementation will vary for different inversion algorithms.

In situations where the algorithm's source code is not available or there is a lack of expertise to modify the code, bootstrap resampling can be used to provide valuable model variability analysis and uncertainty estimates.

In theory the bootstrap approach can be employed without any additional code development, if the resampling of the data sets as well as the starting of the various inversion runs are performed manually. The automation and parallelisation of these processes does greatly increase the efficiency of the method, but is not essential for achieving the desired result.

Furthermore, employing the approach to a different algorithm and/or a different geophysical method does not require any changes to the approach. The only requirement to adapt the process to a new method or algorithm is to perform test runs with synthetic data to determine method and algorithm specific behaviour and effects on the bootstrap uncertainty estimates. This ensures that the uncertainty maps for real data can be interpreted accurately.

5.2 Multi-objective Joint Optimisation

MOJO was developed in an attempt to mitigate uncertainty estimation and shortcomings related to model errors of classic joint inversion approaches (Chapters 3 and 4). The three issues addressed are: firstly, the insufficiency of uncertainty assessments based on single solution optimisation to make a statement about model uncertainty introduced by solution non-uniqueness (Reading et al., 2011). Secondly, the dependency of the inversion results on the choice of data weights (Treitel and Lines, 1999; De Stefano et al., 2011), which are necessary to aggregate all misfit functionals into a joint objective function (Haber and Oldenburg, 1997). Finally, the risk of biasing the inversion results and introducing model artefacts by jointly inverting data sets that are not compatible with each other (Moorkamp et al., 2010, Chapter 3).

MOJO generates satisfactory model fits, which has been demonstrated in extensive synthetic modelling tests (Sections 3.4 and 4.2), as well as for real data (Section 4.3). The model results for the real data were shown to be consistent with previously produced models (Murray, 2012) and consistent with the known geology. This makes the approach advantageous over classic joint inversion methods as it also solves the common problems of such methods.

As MOJO is based on the multi-objective evolutionary algorithm “Borg” (Hadka and Reed, 2013) the search is conducted with a genetic algorithm (Goldberg, 1989; Davis, 1991), which performs a global optimisation (Sen and Stoffa, 2013). This solves the problem of the inadequacy of single solution optimisation by optimising a whole population of solutions. This population is analysed and the results are visualised by displaying the complete model distributions rather than just the solution with the smallest misfit. As discussed in the introduction the solution with the smallest misfit is unlikely to be the closest to the true model (Section 1.3.1). By displaying the full model distributions the variability of the found models and therefore the uncertainty of the modelling result is directly visualised. Furthermore, the range of viable models is immediately obvious. Communicating the inversion results simultaneously with the uncertainty estimates allows for

easy interpretation and decreases the likelihood that features, especially anomalous ones, are overinterpreted.

The use of a genetic algorithms to perform the problem optimisation is also advantageous as genetic algorithms are direct search methods (Lewis et al., 2000), greatly simplifying the algorithms implementation (Sections 1.2.1 and 3.1).

The ultimate goal is an inversion algorithms that is strictly data driven, and does not require any user intervention. This is not yet realised with MOJO, as parameters such as the starting population size and the ε -value have to be chosen, but the need for user interaction is kept to a minimum. The ideal population size is mostly dependent on data set complexity and the available computing resources, whereas the choice of ε -value is strongly dependent on the respective modelling stage, with our tests of the dependencies on the ε -value providing solid guidelines (Section 4.2).

Many other parameters are chosen and adapted automatically by the multi-objective algorithm “Borg”, without the need for user intervention (Section 3.2; Hadka and Reed (2013)). Examples are the adaptation of population and archive sizes during the search and the autonomous choice of the most effective recombination operator, enabling the algorithm to optimise itself for the individual search problem at hand. Furthermore, the algorithm detects search stagnation and triggers a restart to progress the search and limit the risk of the algorithm getting trapped in local minima.

The most important step towards the reduction of user bias taken with MOJO is the elimination of data weighting factors from the inversion process. Data weights are fully eliminated by treating each data set as a separate objective throughout the optimisation process. This mitigates the risk that inappropriate weights are chosen and simplifies the use of the algorithm. To enable the optimisation process to progress the search, proposed model solutions still have to be rated. Without a joint objective function at hand, optimality has to be redefined to allow for solution rating, which is done in form of Pareto-optimality (Edgeworth, 1881; Pareto, 1896; Coello Coello et al., 2007).

The combination of a solution population with the application of Pareto-optimality leads to the fact that the form of the distribution of the solutions

in objective space strongly depends on the level of compatibility between data sets. Moorkamp et al. (2007, 2010) were the first to attempt an assessment of the compatibility between data sets used in geophysical joint inversion modelling. Their approach relied mostly on a visual inspection of the solution distributions, which is fairly imprecise and prone to misinterpretation as shown in Section 3.4.3. This problem is amplified in situations with dense solution clustering, which occur particularly frequently for highly compatible data sets, bearing the risk of misclassification of such data sets as incompatible (Section 4.2). The approach introduced in Chapter 3 is the first ever presented measure to quantify objective compatibility in multi-objective optimisation in general and in geophysical joint inversion modelling in particular. The compatibility of each objective pair is rated by comparing the distribution of the model solutions, with respect to the objectives in question, against an ideal line that corresponds to the solution distribution of identical and therefore perfectly compatible data sets. The method can distinguish between compatible and incompatible data (Sections 3.4 and 4.2), and can also identify data sets that are neither mutually exclusive nor sensitive to common features (Section 4.3.1).

Like the bootstrap resampling method, MOJO and other similar multi-objective joint inversion approaches are easily adapted to work with other data or additional data from different geophysical methods. All that is required is a link between the sets of data and a forward solver for the used type of data. No other modifications are necessary. MOJO is particularly suited for working with data sets from different methods as the adaptive design of “Borg”, as mentioned before, allows MOJO to adjust to a given inversion problem.

5.3 Concluding Comments

A large part of the adaptability and ease of implementation of the two approaches presented in this thesis is bought with an increased demand for computing power and increased memory requirements compared to classic approaches.

This is the main reason why the bootstrap approach was tested for 2-D inversion modelling and MOJO was tested on 1-D data sets. To perform comprehensive tests many different test inversion runs have to be performed, which made it necessary to limit the tests to 2-D and 1-D data respectively.

While these tests are sufficient to demonstrate the feasibility of the two concepts, making the approaches viable for general use they have to be expanded towards working with higher dimensional data sets. With the computing facilities commonly available to date, the bootstrap resampling method is likely viable for 3-D inversion modelling and multi-objective joint inversion could be employed in 2-D joint inversion modelling. The extension of MOJO to 3-D inversion modelling is by my estimation not feasible to date, but if Moore's law (Moore, 1965; Brock and Moore, 2006), predicting the doubling of transistors per square inch of integrated circuit every two years, continues to be accurate it is only a matter of time before MOJO and approaches like it become viable for inverting multiple 3-D data sets on a regular basis.

Some might argue that the additional computing power required for approaches like the ones presented in this thesis can be put to better use by utilising it to invert larger models and larger sets of data, and there is no denying that larger models provide valuable information. Nevertheless, the quality of that information has to be known for it to be of use. The larger and more complicated models get the higher the risk that the sheer volume of information becomes overwhelming, increasing the chance of misinterpretations. This makes the use of advanced uncertainty estimation techniques not only beneficial, but mandatory to be able to reliably interpret model results.

Furthermore, this work demonstrates that approaches such as MOJO can not only provide model uncertainty estimates that go far beyond the validity and meaningfulness of RMS deviation values and similar misfit measures (c.f. Section 1.3.1), but also eliminate data weighting bias and ensure that the used data sets are compatible to each other. Thus, the approach avoids the introduction of model errors from incorrect assumptions made by the user. An additional benefit of the more advanced uncertainty estimates is that they are not communicated in word format, but rather via pictures. The human brain can process and remember information communicated

through pictures much more easily than through written words. This phenomenon is called the picture superiority effect (Shepard, 1967; Whitehouse et al., 2006).

Human factors have a great influence on the generation and interpretation of inversion models and this bias has to be kept in mind as long as the need for human intervention is not fully eliminated from the inversion process. The communication of the results is just one of these factors. Another important factor is how accessible a given method is. The implementation and operation of the approaches presented in this thesis were kept as simple as possible to make them accessible to a wide audience and increase their usability. Similarly, the presentation of the results, especially the visualisation, was kept as simple and concise as possible to allow for an easy and unambiguous interpretation.

This will be an important part of future research into model quality assessment. As discussed above, the extension of these types of approaches to larger data sets and higher dimensional data is straightforward, and the calculation of the relevant uncertainty measures does not pose much of a problem, but the concise communication of the results will become more challenging. For a 1-D model it is easy to display the full distribution of models, which provides all information needed to make an informed decision about the significance of the generated models, as demonstrated in Chapter 4. On the other hand, for higher dimensional models the visualisation of the uncertainty measures becomes more complicated, especially if a simple and concise presentation is sought. One thing that can help in the visualisation of models and model quality measures are virtual reality systems. Such systems are already used on a regular basis to visualise large seismic models (Polyakov, 1999; Evans et al., 2002; Ma and Rokne, 2004; Castanié et al., 2005; Li, 2014), and smaller scale, lower cost systems are coming onto the market (Choi et al., 2015).

At some point the larger and more complex models will require psychological factors to be taken into account when designing uncertainty estimation schemes. One example is the so called confirmation bias or expectation bias, which lead to an overinterpretation of results that support the experimenter's hypothesis or beliefs (Pohl, 2004; Jeng, 2006). This is related to congruence bias, the tendency to neglect indirect hypothesis testing ap-

proaches (Iverson et al., 2008). The use of multi-solution methods and the display of the complete model distributions can possibly mitigate the effects of these biases as they explore various alternate solutions, which are displayed along with all other alternatives, allowing for an easy comparison. When displaying ranges of models it is also important to ensure that it is obvious with which frequency certain model features occur to avoid the effects of clustering illusions (Iverson et al., 2008) and neglect of probability bias (Baron, 2000), which can lead to an overinterpretation of features despite their low probability. This also relates to the bizarreness effect (Schmidt, 2012), the tendency of the human mind to react stronger to bizarre features, which in case of modelling correspond to extremal models and anomalies. Even the choice of colour scale for the visualisation of models and model quality can influence the interpretation as contrast and colour influence the perception (Desimone and Duncan, 1995; Nothdurft, 2000a,b,c). Cognitive biases have to be considered especially in the design of the result visualisation and communication techniques.

This project is a first step in the advancement of uncertainty estimation and model quality analysis in geophysical inversion modelling, and will hopefully help to make the use of meaningful model uncertainty analysis more common.

APPENDIX

A

A.1 Supporting Material for Chapter 4

A.1.1 Figures

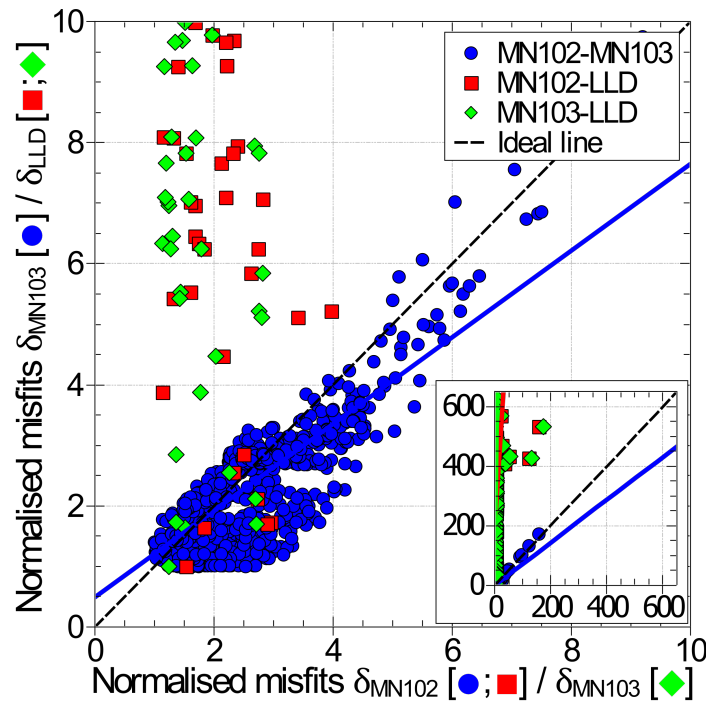


Figure A.1: Solution distributions for the MN102-MN103-objective (blue), MN102-LLD objective (red), and MN103-LLD-objective (green) and the corresponding Theil-Sen regressions (solid lines) (Section 4.3.1.1). The dashed line represents the ideal line.

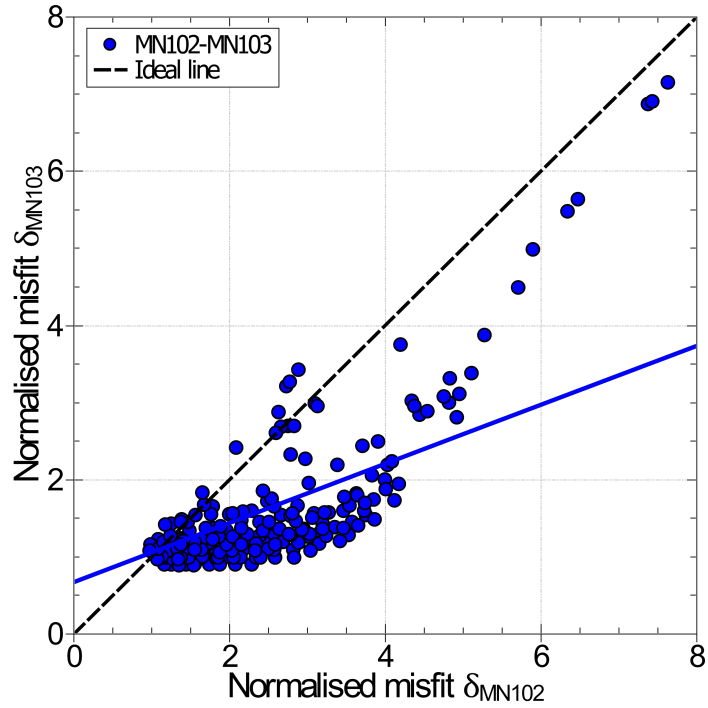


Figure A.2: Solution distribution for the MN102-MN103 MOJO run and the corresponding Theil-Sen regression (solid blue line) (Section 4.3.1.1). The dashed line represents the ideal line.

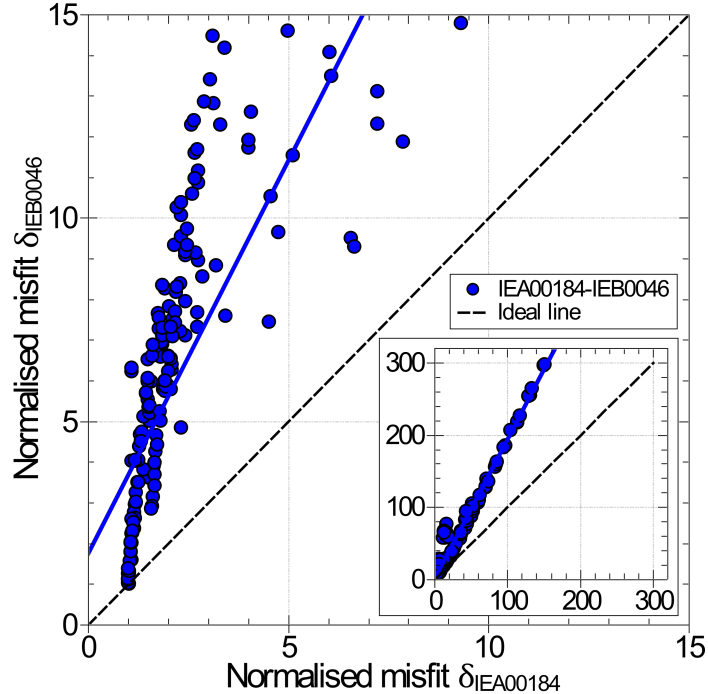


Figure A.3: Solution distribution for the Isa Extension Survey data and the corresponding Theil-Sen regression (solid blue line) (Section 4.3.2.1). The dashed line represents the ideal line.

A.1.2 Tables

Table A.1: Analysis of the deviation from the ideal line for the MN102-MN103 MOJO run (Section 4.3.1.1). The analysis is performed for archives at different stages of the inversion run, as well as for all extracted archive members combined.

Solution evaluations	Deviation angles
1,000	10°
10,000	8°
100,00	26°
200,000	33°
Combined	24°

BIBLIOGRAPHY

- Aarts, E. and Korst, J. (1989). *Simulated Annealing and Boltzmann Machines*. John Wiley & Sons, Chichester.
- Abubakar, A., Li, M., Pan, G., Liu, J., and Habashy, T. M. (2011). Joint MT and CSEM data inversion using a multiplicative cost function approach. *Geophysics*, 76(3):F203 – F214.
- Alumbaugh, D. L. and Newman, G. A. (2000). Image appraisal for 2-D and 3-D electromagnetic inversion. *Geophysics*, 65(5):1455–1467.
- Anderssen, R. S. (1970). The character of non-uniqueness in the conductivity modelling problem for the Earth. *Pageoph*, 80(III):238 – 259.
- Anderssen, R. S. and Seneta, E. (1971). A simple statistical estimation procedure for Monte Carlo inversion in geophysics. *Pageoph*, 91(VIII):5 – 13.
- Apak, S. N. (1994). *Structural development and control on stratigraphy and sedimentation in the Cooper Basin, northeastern South Australia and southwestern Queensland*. PhD thesis, National Centre for Petroleum Geology and Geophysics, Adelaide, Australia.
- Aster, R. C., Borchers, B., and Thurber, C. (2012). *Parameter Estimation and Inverse Problems*. Elsevier Academic Press, 2 edition.
- Avdeev, D. and Avdeeva, A. (2009). 3D magnetotelluric inversion using a limited-memory quasi-newton optimization. *Geophysics*, 74(3):F45–F57.
- Avdeev, D. B. (2005). Three-dimensional electromagnetic modelling and inversion from theory to application. *Surv. Geophys.*, 26(6):767–799.

BIBLIOGRAPHY

- Backus, G. E. and Gilbert, J. F. (1967). Numerical applications of a formalism for geophysical inverse problems. *Geophys. J. R. astr. Soc.*, 13(1-3):247–276.
- Backus, G. E. and Gilbert, J. F. (1968). The resolving power of gross earth data. *Geophys. J. R. astr. Soc.*, 16(2):169–205.
- Backus, G. E. and Gilbert, J. F. (1970). Uniqueness in the inversion of inaccurate gross earth data. *Phil. Trans. R. Soc. Lond.*, 266(1173):123 – 192.
- Baron, J. (2000). *Thinking and Deciding*. Cambridge Univ. Press.
- Bayes, T. (1763). An essay towards solving a problem in the doctrine of chances. *Phil. Trans. R. Soc. Lond.*, 53:370–418.
- Becken, M., Ritter, O., Park, S. K., Bedrosian, P. A., Weckmann, U., and Weber, M. (2008). A deep crustal fluid channel into the San Andreas fault system near Parkfield, California. *Geophys. J. Int.*, 173(2):718–732.
- Berdichevskiy, M. N. and Dmitriev, V. I. (1976). Basic principles of interpretation of magnetotelluric sounding curves. In Ádám, A., editor, *Geoelectric and Geothermal Studies: East-Central Europe, Soviet Asia KAPG Geophysical Monograph*. Akadémiai Kiadó, Budapest.
- Bibby, H. M., Caldwell, T. G., and Brown, C. (2005). Determinable and non-determinable parameters of galvanic distortion in magnetotellurics. *Geophys. J. Int.*, 163(3):915–930.
- Blundell, S. and Blundell, K. (2009). *Concepts in Thermal Physics*. Oxford Univ. Press, 2 edition.
- Brock, D. C. and Moore, G. E. (2006). *Understanding Moore's Law: Four Decades of Innovation*. Chemical Heritage Foundation.
- Buland, A. and Kolbjørnsen, O. (2012). Bayesian inversion of CSEM and magnetotelluric data. 77(1):E33–E42.
- Caldwell, T. G., Bibby, H. M., and Brown, C. (2004). The magnetotelluric phase tensor. *Geophys. J. Int.*, 158(2):457–469.

- Campanya, J., Ledo, J., Queralt, P., Marcuello, A., and Jones, A. G. (2014). A new methodology to estimate magnetotelluric (MT) tensor relationships: estimation of local transfer-functions by combining interstation transfer-functions (ELICIT). *Geophys. J. Int.*, 198(1):484–494.
- Carcione, J. M., Ursin, B., and Nordskag, J. I. (2007). Cross-property relations between electrical conductivity and the seismic velocity of rocks. *Geophysics*, 72(5):E193–E204.
- Castanié, L., Bosquet, F., and Levy, B. (2005). Advances in seismic interpretation using new volume visualization techniques. *First Break*, 23:69–72.
- Černý, V. (1985). Thermodynamical approach to the travelling salesman problem: An efficient simulation algorithm. *Journal of Optimization Theory and Applications*, 45(1):41–51.
- Chave, A. D. (2014a). Magnetotelluric data, stable distribution and impropriety: an existential combination. *Geophys. J. Int.*, 198(1):622–636.
- Chave, A. D. (2014b). On the statistics of magnetotelluric rotational invariants. *Geophys. J. Int.*, 196(1):111–130.
- Chave, A. D. and Jones, A. G. (2012). *The Magnetotelluric Method: Theory and Practice*. Cambridge Univ. Press.
- Chen, J., Hoversten, G. M., Key, K., Nordquist, G., and Cumming, W. (2012). Stochastic inversion of magnetotelluric data using a sharp boundary parameterization and application to a geothermal site. *Geophysics*, 77(4):E265–E279.
- Choi, H., Byun, J., and Seol, S. J. (2010). Automatic velocity analysis using bootstrapped differential semblance and global search methods. *Explor. Geophys.*, 41(1):31–39.
- Choi, S., Jung, K., and Noh, S. D. (2015). Virtual reality applications in manufacturing industries: Past research, present findings, and future directions. *Concurrent Engineering*, 23(1).
- Coello Coello, C. A., Lamont, G. B., and Van Veldhuizen, D. A. (2007). *Evolutionary Algorithms for Solving Multi-Objective Problems*. Springer, second edition.

BIBLIOGRAPHY

- Colombo, D. and De Stefano, M. (2007). Geophysical modeling via simultaneous joint inversion of seismic, gravity, and electromagnetic data: Application to prestack depth imaging. *The Leading Edge*, 26(3):326–331.
- Commer, M. and Newman, G. A. (2009). Three-dimensional controlled-source electromagnetic and magnetotelluric joint inversion. *Geophys. J. Int.*, 178(3):1305 – 1316.
- Constable, S. C., Parker, R. L., and Constable, C. G. (1987). Occam’s inversion: A practical algorithm for generating smooth models from electromagnetic sounding data. *Geophysics*, 52(3):289–300.
- Coxeter, H. (1973). *Regular Polytopes*. Dover Books on Mathematics Series. Dover Publications.
- Davis, L. D. (1991). *Handbook of Genetic Algorithms*. VNR computer library. Van Nostrand Reinhold.
- De Jong, K. A. (1975). *An Analysis of the Behavior of a Class of Genetic Adaptive Systems*. PhD thesis, Ann Arbor, MI, USA. AAI7609381.
- De Nardis, R., Cardarelli, E., and Dobróka, M. (2005). Quasi-2D hybrid joint inversion of seismic and geoelectric data. *Geophys. Prospect.*, 53(5):705 – 716.
- De Stefano, M., Andreasi, F. G., Re, S., Virgilio, M., and Snyder, F. F. (2011). Multiple-domain, simultaneous joint inversion of geophysical data with application to subsalt imaging. *Geophysics*, 76(3):R69–R80.
- Deal, M. M. and Nolet, G. (1996). Nullspace shuttles. *Geophys. J. Int.*, 124(2):372–380.
- Deb, K. and Agarwal, R. B. (1994). Simulated binary crossover for continuous search space. Technical Report ITK/ME/SMD-94027, Indian Institute of Technology, Kanpur, UP, India.
- Deb, K. and Goyal, M. (1996). A combined genetic adaptive search (GeneAS) for engineering design. *Computer Science and Informatics*, 26(4):30–45.

- Deb, K., Joshi, D., and Anand, A. (2002a). Real-coded evolutionary algorithms with parent-centric recombination. In *Proc. of the World Congress on Computational Intelligence*, pages 61–66.
- Deb, K., Mohan, M., and Mishra, S. (2003). A fast multi-objective evolutionary algorithm for finding well-spread Pareto-optimal solutions. Technical Report 2003002, Kanpur Genetic Algorithms Laboratory (Kan-GAL).
- Deb, K., Pratap, A., Agarwal, S., and Meyarivan, T. (2002b). A fast and elitist multiobjective genetic algorithm: NSGA-II. *Evolutionary Computation, IEEE Trans. on*, 6(2):182–197.
- deGroot Hedlin, C. and Constable, S. (1990). Occam’s inversion to generate smooth, two-dimensional models from magnetotelluric data. *Geophysics*, 55(12):1613–1624.
- Desimone, R. and Duncan, J. (1995). Neural mechanisms of selective visual attention. *Annual Review of Neuroscience*, 18:193–222.
- Dobróka, M., Gyulai, Á., Ormos, T., Csókás, J., and Dresen, L. (1991). Joint inversion of seismic and geoelectric data recorded in an underground coal mine. *Geophys. Prospect.*, 39(5):643–665.
- Dosso, S. E. and Oldenburg, D. W. (1991). Magnetotelluric appraisal using simulated annealing. *Geophys. J. Int.*, 106(2):379–385.
- Edgeworth, F. Y. (1881). *Mathematical Physics: An Essay on the Application of Mathematics to the Moral Sciences*. Reprints of economic classics. C. K. Paul.
- Efron, B. (1979). Bootstrap methods: Another look at the jackknife. *The Annals of Statistics*, 7(1):1–26.
- Efron, B. (1982). *The Jackknife, the Bootstrap and Other Resampling Plans*. SIAM.
- Efron, B. and Tibshirani, R. (1986). Bootstrap methods for standard errors, confidence intervals, and other measures of statistical accuracy. *Statist. Sci.*, 1(1):54–77.

BIBLIOGRAPHY

- Evans, F., Volz, W., Dorn, G., Fröhlich, B., and Roberts, D. M. (2002). Future trends in oil and gas visualization. In *Proc. of the Conference on Visualization '02*, VIS '02, pages 567–570, Washington, DC, USA. IEEE Computer Society.
- Everett, M. E. and Schultz, A. (1993). Two-dimensional nonlinear magnetotelluric inversion using a genetic algorithm. *Journal of Geomagnetism and Geoelectricity*, 45(9):1013–1026.
- Everitt, B. S. and Skrondal, A. (2011). *The Cambridge Dictionary of Statistics*. Cambridge Univ. Press, 4 edition.
- Finlayson, D. M. (1983). The mid-crustal horizon under the Eromanga Basin, eastern Australia. *Tectonophysics*, 100(1–3):199–214. Continental Tectonics: Structure, Kinematics and Dynamics.
- Finlayson, D. M., Collins, C. D. N., and Lock, J. (1984). P-wave velocity features of the lithosphere under the Eromanga Basin, eastern Australia, including a prominent MID-crustal (Conrad?) discontinuity. *Tectonophysics*, 101(3–4):267 – 291.
- Fischer, G. and Le Quang, B. V. (1982). Parameter trade-off in one-dimensional magnetotelluric modelling. *J. Geophys.*, 51(3):206–215.
- Fischer, G., Schnegg, P. A., Peguiron, M., and Le Quang, B. V. (1981). An analytic one-dimensional magnetotelluric inversion scheme. *Geophys. J. R. astr. Soc.*, 67(2):257–278.
- Flanagan, M. P. and Shearer, P. M. (1998). Global mapping of topography on transition zone velocity discontinuities by stacking SS precursors. *J. geophys. Res.*, 103(B2):2673–2692.
- Gallagher, K. and Sambridge, M. (1994). Genetic algorithms: A powerful tool for large-scale nonlinear optimization problems. *Computers & Geosciences*, 20(7/8):1229–1236.
- Gallardo, L. A. and Meju, M. A. (2003). Characterization of heterogeneous near-surface materials by joint 2D inversion of dc resistivity and seismic data. *Geophys. Res. Lett.*, 30(13):1658.

- Gallardo, L. A. and Meju, M. A. (2007). Joint two-dimensional cross-gradient imaging of magnetotelluric and seismic traveltimes for structural and lithological classification. *Geophys. J. Int.*, 169(3):1261–1272.
- Gamerman, D. (1997). *Markov chain Monte Carlo: Stochastic simulation for Bayesian inference*. Chapman and Hall/CRC.
- Garth, L. M. and Poor, H. V. (1994). Detection of non-Gaussian signals: a paradigm for modern statistical signal processing [and prolog]. *Proc. of the IEEE*, 82(7):1061–1095.
- Gelman, A., Carlin, J. B., Stern, H. S., and Rubin, D. B. (2003). *Bayesian Data Analysis, Second Edition*. Chapman & Hall/CRC Texts in Statistical Science. Taylor & Francis.
- Goh, C. K. and Tan, K. C. (2007). An investigation on noisy environments in evolutionary multiobjective optimization. *Evolutionary Computation, IEEE Trans. on*, 11(3):354–381.
- Goldberg, D. E. (1989). *Genetic Algorithms in Search, Optimization and Machine Learning*. Addison-Wesley Longman Publishing Co., Inc., Boston, MA, USA, 1st edition.
- Grandis, H., Menvielle, M., and Roussignol, M. (2002). Thin-sheet electromagnetic inversion modeling using Monte Carlo Markov chain (MCMC) algorithm. *Earth, Planets Space*, 54(5):511–521.
- Guo, R., Dosso, S. E., Liu, J., Dettmer, J., and Tong, X. (2011). Non-linearity in Bayesian 1-D magnetotelluric inversion. *Geophys. J. Int.*, 185(2):663–675.
- Gurrola, H. and Minster, J. B. (1998). Thickness estimates of the upper-mantle transition zone from bootstrapped velocity spectrum stacks of receiver functions. *Geophys. J. Int.*, 133(1):31–43.
- Gurrola, H., Minster, J. B., and Owens, T. (1994). The use of velocity spectrum for stacking receiver functions and imaging upper mantle discontinuities. *Geophys. J. Int.*, 117(2):427–440.
- Guyodo, Y. and Valet, J.-P. (1996). Relative variations in geomagnetic intensity from sedimentary records: the past 200,000 years. *Earth Planet. Sci. Lett.*, 143(1–4):23–36.

BIBLIOGRAPHY

- Haber, E. (2014). *Computational Methods in Geophysical Electromagnetics*, volume 1 of *Mathematics in Industry*. SIAM.
- Haber, E., Ascher, U. M., and Oldenburg, D. W. (2004). Inversion of 3D electromagnetic data in frequency and time domain using an inexact all-at-once approach. *Geophysics*, 69(5):1216–1228.
- Haber, E. and Holtzman Gazit, M. (2013). Model fusion and joint inversion. *Surv. Geophys.*, 34(5):675–695.
- Haber, E. and Oldenburg, D. (1997). Joint inversion: a structural approach. *Inverse Prob.*, 13(1):63.
- Habermehl, M. A. (1980). The Great Artesian Basin, Australia. *BMR J. Aust. Geol. Geophys.*, 5(1):9–38.
- Hadka, D. and Reed, P. (2012). Diagnostic assessment of search controls and failure modes in many-objective evolutionary optimization. *Evolutionary Computation*, 20(3):423–452.
- Hadka, D. and Reed, P. (2013). Borg: An auto-adaptive many-objective evolutionary computing framework. *Evolutionary Computation*, 21(2):231–259.
- Halton, J. H. (1970). A retrospective and prospective survey of the Monte Carlo method. *SIAM Review*, 12(1):1 – 63.
- Hammersley, J. M. and Handscomb, D. C. (1964). *Monte Carlo Methods*. Methuen, London and New York.
- Hanne, T. (1999). On the convergence of multiobjective evolutionary algorithms. *European Journal of Operational Research*, 117(3):553–564.
- Hanne, T. (2001). Global multiobjective optimization with evolutionary algorithms: Selection mechanisms and mutation control. In Zitzler, E., Thiele, L., Deb, K., Coello Coello, C. A., and Corne, D., editors, *Evolutionary Multi-Criterion Optimization*, volume 1993 of *Lecture Notes in Computer Science*, pages 197–212. Springer Berlin Heidelberg.
- Hansen, P. C., Jacobsen, B. H., and Mosegaard, K., editors (2000). *Methods and Applications of Inversion*, volume 92 of *Lecture Notes in Earth Sciences*. Springer-Verlag Berlin Heidelberg, 1 edition.

- Heincke, B., Jegen, M., and Hobbs, R. (2006). *Joint inversion of MT, gravity and seismic data applied to sub-basalt imaging*, chapter 157, pages 784–789.
- Higuchi, T., Tsutsui, S., and Yamamura, M. (2000). Theoretical analysis of simplex crossover for real-coded genetic algorithms. In *Parallel Problem Solving from Nature PPSN VI*, volume 1917 of *Lecture Notes in Computer Science*, pages 365–374. Springer Berlin Heidelberg.
- Holland, J. H. (1975). *Adaptation in natural and artificial systems: an introductory analysis with applications to biology, control, and artificial intelligence*. University of Michigan Press.
- Ikeda, K., Kita, H., and Kobayashi, S. (2001). Failure of Pareto-based MOEAs: does non-dominated really mean near to optimal? In *Proc. of the 2001 Congress on Evolutionary Computation*, volume 2, pages 957–962.
- Ishibuchi, H., Tsukamoto, N., Hitotsuyanagi, Y., and Nojima, Y. (2008). Effectiveness of scalability improvement attempts on the performance of NSGA-II for many-objective problems. In Keijzer, M., Antoniol, G., Congdon, C. B., Deb, K., Doerr, B., Hansen, N., Holmes, J. H., Hornby, G. S., Howard, D., Kennedy, J., Kumar, S., Lobo, F. G., Miller, J. F., Moore, J., Neumann, F., Pelikan, M., Pollack, J., Sastry, K., Stanley, K., Stoica, A., Talbi, E.-G., and Wegener, I., editors, *GECCO '08: Proc. of the 10th annual conference on Genetic and evolutionary computation*, pages 649 – 656, Atlanta, GA, USA. ACM.
- Iverson, G. L., Brooks, B. L., and Holdnack, J. A. (2008). Misdiagnosis of cognitive impairment in forensic neuropsychology. In Heilbronner, R. L., editor, *Neuropsychology in the Courtroom: Expert Analysis of Reports and Testimony*, Forensic neuropsychology casebook, pages 243–266. Guilford Press, New York, NY, US.
- Jackson, D. D. (1972). Interpretation of inaccurate, insufficient and inconsistent data. *Geophys. J. R. astr. Soc.*, 28(2):97–109.
- Jackson, D. D. (1976). Most squares inversion. *J. geophys. Res.*, 81(5):1027–1030.

BIBLIOGRAPHY

- Jegen, M. D., Hobbs, R. W., Tarits, P., and Chave, A. (2009). Joint inversion of marine magnetotelluric and gravity data incorporating seismic constraints - preliminary results of sub-basalt imaging off the Faroe Shelf. *Earth Planet. Sci. Lett.*, 282(1–4):47–55.
- Jell, P. A., editor (2013). *Geology of Queensland*. Geological Survey of Queensland, Brisbane, Queensland, Australia.
- Jeng, M. (2006). A selected history of expectation bias in physics. *Am. J. Phys.*, 74(7):578–583.
- Jonkers, A. R. T. (2007). Bootstrapped discrete scale invariance analysis of geomagnetic dipole intensity. *Geophys. J. Int.*, 169(2):646–658.
- Julià, J., Ammon, C. J., Herrmann, R. B., and Correig, A. M. (2000). Joint inversion of receiver function and surface wave dispersion observations. *Geophys. J. Int.*, 143(1):99–112.
- Kalscheuer, T., de los Ángeles García Juanatey, M., Meqbel, N., and Pedersen, L. B. (2010). Non-linear model error and resolution properties from two-dimensional single and joint inversions of direct current resistivity and radiomagnetotelluric data. *Geophys. J. Int.*, 182(3):1174–1188.
- Keilis-Borok, V. I. and Yanovskaja, T. B. (1967). Inverse problems of seismology (structural review). *Geophys. J. R. astr. Soc.*, 13(1–3):223–234.
- Kelbert, A., Meqbel, N., Egbert, G. D., and Tandon, K. (2014). ModEM: A modular system for inversion of electromagnetic geophysical data. *Computers & Geosciences*, 66:40–53.
- Kennett, B. and Nolet, G. (1978). Resolution analysis for discrete systems. *Geophys. J. R. astr. Soc.*, 53(2):413–425.
- Kennett, B. L. N., Salmon, M., and Saygin, E. (2011). AusMoho: the variation of Moho depth in Australia. *Geophys. J. Int.*, 187(2):946–958.
- Kirkpatrick, S., Gelatt, C. D., and Vecchi, M. P. (1983). Optimization by simulated annealing. *Science*, 220(4598):671–680.

- Kita, H., Ono, I., and Kobayashi, S. (1999). Multi-parental extension of the unimodal normal distribution crossover for real-coded genetic algorithms. In *Proc. of the 1999 Congress on Evolutionary Computation*, pages 1581–1588.
- Koch, M. (1992). Bootstrap inversion for vertical and lateral variations of the S-wave structure and the VP/VS-ratio from shallow earthquakes in the Rhinegraben seismic zone, Germany. *Tectonophysics*, 210(1-2):91–115.
- Kollat, J. B. and Reed, P. M. (2007). A computational scaling analysis of multiobjective evolutionary algorithms in long-term groundwater monitoring applications. *Advances in Water Resources*, 30(3):408–419.
- Korenaga, J. (2013). Stacking with dual bootstrap resampling. *Geophys. J. Int.*, 195(3):2023–2036.
- Korenaga, J. (2014). Teleseismic migration with dual bootstrap stack. *Geophys. J. Int.*, 196(3):1706–1723.
- Kozlovskaya, E., Vecsey, L., Plomerová, J., and Raita, T. (2007). Joint inversion of multiple data types with the use of multiobjective optimization: Problem formulation and application to the seismic anisotropy investigations. *Geophys. J. Int.*, 171(2):761–779.
- Krieger, L. and Peacock, J. R. (2014). MTpy: A Python toolbox for magnetotellurics. *Computers & Geosciences*, 72:167 – 175.
- Laloy, E., Linde, N., and Vrugt, J. A. (2012). Mass conservative three-dimensional water tracer distribution from MCMC inversion of timelapse GPR data. *Water Resour. Res.*, 48(7):W07510.
- Laumanns, M., Thiele, L., Deb, K., and Zitzler, E. (2002). Combining convergence and diversity in evolutionary multi-objective optimization. *Evolutionary Computation*, 10(3):263–282.
- Laumanns, M., Thiele, L., and Zitzler, E. (2004). Running time analysis of multiobjective evolutionary algorithms on pseudo-boolean functions. *Evolutionary Computation, IEEE Transactions on*, 8(2):170–182.

BIBLIOGRAPHY

- Lawson, C. L. and Hanson, R. J. (1974). *Solving Least Squares Problems*. Classics in Applied Mathematics. SIAM.
- Lewis, R. M., Torczon, V., and Trosset, M. W. (2000). Direct search methods: then and now. *J. Comput. Appl. Math.*, 124(1-2):191 – 207. Numerical Analysis 2000. Vol. IV: Optimization and Nonlinear Equations.
- Li, M. (2014). *Geophysical Exploration Technology: Applications in Lithological and Stratigraphic Reservoirs*. Elsevier Science.
- Li, Y. and Oldenburg, D. W. (2000). Joint inversion of surface and three-component borehole magnetic data. *Geophysics*, 65(2):540 – 552.
- Linde, N. and Vrugt, J. (2013). Distributed soil moisture from crosshole ground-penetrating radar travel times using stochastic inversion. *Vadose Zone Journal*, 12(1):0101.
- Lomax, A. and Snieder, R. (1995). Identifying sets of acceptable solutions to non-linear, geophysical inverse problems which have complicated mist functions. *Nonlin. Processes Geophys.*, 2(3/4):222–227.
- Ma, C. and Rokne, J. (2004). 3D Seismic Volume Visualization. In Zhang, D. D., Kamel, M., and Baciu, G., editors, *Integrated Image and Graphics Technologies*, volume 762 of *The International Series in Engineering and Computer Science*, pages 241–262. Springer US.
- Mackie, R., Rieven, S., and Rodi, W. (1997). Users manual and software documentation for two-dimensional inversion of magnetotelluric data. *San Francisco, GSY-USA, 14pp*.
- Manoj, C. and Nagarajan, N. (2003). The application of artificial neural networks to magnetotelluric time-series analysis. *Geophys. J. Int.*, 153(2):409–423.
- Marescot, L., Loke, M. H., D.Chapellier, Delaloye, R., Lambiel, C., and Reynard, E. (2003). Assessing reliability of 2D resistivity imaging in mountain permafrost studies using the depth of investigation method. *Near Surface Geophysics*, 1(2):57–67.
- Martí, A., Queralt, P., and Roca, E. (2004). Geoelectric dimensionality in complex geological areas: application to the Spanish Betic Chain. *Geophys. J. Int.*, 157(3):961–974.

- McKean, J. W. (2004). Robust analysis of linear models. *Statist. Sci.*, 19(4):562–570.
- McLaughlin, K. L. (1988). Maximum-likelihood event magnitude estimation with bootstrapping for uncertainty estimation. *Bull. seism. Soc. Am.*, 78(2):855–862.
- Meju, M. A. (1994). *Geophysical Data Analysis: Understanding Inverse Problem Theory and Practice*. Society of Exploration Geophysicists.
- Meju, M. A. and Hutton, V. R. S. (1992). Iterative most-squares inversion: application to magnetotelluric data. *Geophys. J. Int.*, 108(3):758–766.
- Menke, W. (2012). *Geophysical Data Analysis: Discrete Inverse Theory*. Academic Press.
- Metropolis, N. and Ulam, S. (1949). The Monte Carlo method. *JASA*, 44(247):335–341.
- Miecznik, J., a, M. W., and Danek, T. (2003). Application of nonlinear methods to inversion of 1D magnetotelluric sounding data based on very fast simulated annealing. *Acta Geophysica Polonica*, 51(3):307–322.
- Miller, B. L. and Goldberg, D. E. (1995). Genetic algorithms, tournament selection, and the effects of noise. *Complex Systems*, 9(3):193–212.
- Moore, G. E. (1965). Cramming more components onto integrated circuits. *Electronics*, 38(8):114–117.
- Moorkamp, M., Heincke, B., Jegen, M., Roberts, A. W., and Hobbs, R. W. (2011). A framework for 3-D joint inversion of MT, gravity and seismic refraction data. *Geophys. J. Int.*, 184(1):477–493.
- Moorkamp, M., Jones, A. G., and Eaton, D. W. (2007). Joint inversion of teleseismic receiver functions and magnetotelluric data using a genetic algorithm: Are seismic velocities and electrical conductivities compatible? *Geophys. Res. Lett.*, 34(16).
- Moorkamp, M., Jones, A. G., and Fishwick, S. (2010). Joint inversion of receiver functions, surface wave dispersion, and magnetotelluric data. *J. geophys. Res.*, 115(B4).

BIBLIOGRAPHY

- Mosegaard, K. and Tarantola, A. (1995). Monte Carlo sampling of solutions to inverse problems. *J. Geophys. Res.: Solid Earth*, 100(B7):12431–12447.
- Mota, R. and Monteiro dos Santos, F. (2006). 2D sections of porosity and water saturation percent from combined resistivity and seismic surveys for hydrogeologic studies. *The Leading Edge*, 25(6):735–737.
- Muñoz, G. and Rath, V. (2006). Beyond smooth inversion: the use of nullspace projection for the exploration of non-uniqueness in MT. *Geophys. J. Int.*, 164(2):301–311.
- Murray, P. (2012). A comparison of porosity values inferred from magnetotelluric and bore-hole density data; case studies from two geothermal regions in South Australia. Honours thesis, University of Adelaide.
- Neukirch, M. and Garcia, X. (2014). Nonstationary magnetotelluric data processing with instantaneous parameter. *J. geophys. Res.*, 119(3):1634–1654.
- Newman, G. A. and Alumbaugh, D. L. (1997). Three-dimensional massively parallel electromagnetic inversion – I. Theory. *Geophys. J. Int.*, 128(2):345–354.
- Newman, G. A. and Alumbaugh, D. L. (2000). Three-dimensional magnetotelluric inversion using non-linear conjugate gradients. *Geophys. J. Int.*, 140(2):410 – 424.
- Newman, G. A. and Boggs, P. T. (2014). Solution accelerators for large-scale three-dimensional electromagnetic inverse problems. *Inverse Prob.*, 20(6):151–170.
- Nolte, B. and Frazer, L. N. (1994). Vertical seismic profile inversion with genetic algorithms. *Geophys. J. Int.*, 117(1):162–178.
- Nothdurft, H.-C. (2000a). Salience from feature contrast: additivity across dimensions. *Vision Research*, 40(10–12):1183–1201.
- Nothdurft, H.-C. (2000b). Salience from feature contrast: temporal properties of saliency mechanisms. *Vision Research*, 40(18):2421–2435.
- Nothdurft, H.-C. (2000c). Salience from feature contrast: variations with texture density. *Vision Research*, 40(23):3181–3200.

- Oldenburg, D. W. and Li, Y. (1999). Estimating depth of investigation in DC resistivity and IP surveys. *Geophysics*, 64(2):403–416.
- Pareto, V. (1896). *Cours d'Économie Politique*, volume I and II. F. Rouge, Lausanne.
- Parker, R. L. (1980). The inverse problem of electromagnetic induction: Existence and construction of solutions based on incomplete data. *J. Geophys. Res.: Solid Earth*, 85(B8):4421–4428.
- Parker, R. L. (1994). *Geophysical Inverse Theory*. Princeton Univ. Press, Princeton.
- Parker, R. L. and Whaler, K. A. (1981). Numerical methods for establishing solutions to the inverse problem of electromagnetic induction. *J. Geophys. Res.: Solid Earth*, 86(B10):9574–9584.
- Pek, J. and Santos, F. A. (2006). Magnetotelluric inversion for anisotropic conductivities in layered media. *Phys. Earth Planet. Inter.*, 158(2–4):139 – 158.
- Pek, J. and Verner, T. (1997). Finite-difference modelling of magnetotelluric fields in two-dimensional anisotropic media. *Geophys. J. Int.*, 128(3):505–521.
- Pérez-Flores, M. A. and Schultz, A. (2002). Application of 2-D inversion with genetic algorithms to magnetotelluric data from geothermal areas. *Earth, Planets Space*, 54(5):607–616.
- Podinovsky, V. V. and Nogin, V. D. (1982). *Pareto-Optimal Solutions of Multicriteria Problems*. Nauka, Moscow. in Russian.
- Pohl, R. (2004). *Cognitive Illusions: A Handbook on Fallacies and Biases in Thinking, Judgement and Memory*. Psychology Press.
- Polyakov, V. (1999). Virtual reality in oil and gas industry. *ECRIM News*, (37).
- Press, F. (1968). Earth models obtained by Monte Carlo inversion. *J. geophys. Res.*, 73(16):5223 – 5234.

BIBLIOGRAPHY

- Press, F. and Biehler, S. (1964). Inferences on crustal velocities and densities from P wave delays and gravity anomalies. *J. geophys. Res.*, 69(14):2979 – 2995.
- Purshouse, R. C. and Fleming, P. J. (2007). On the evolutionary optimization of many conflicting objectives. *Evolutionary Computation, IEEE Trans. on*, 11(6):239–245.
- Ramirez, A. L., Daily, W. D., and Newmark, R. L. (1995). Electrical resistance tomography for steam injection monitoring and control. *Journal of Environmental and Engineering Geophysics*, 1(A):39–52.
- Ransley, T. R. and Smerdon, B. (2012). Hydrostratigraphy, hydrogeology and system conceptualisation of the Great Artesian Basin. Technical Report EP132693, CSIRO Great Artesian Basin Water Resource Assessment, Australia: CSIRO Water for a Healthy Country Flagship.
- Ray, A. and Key, K. (2012). Bayesian inversion of marine CSEM data with a trans-dimensional self parametrizing algorithm. *Geophys. J. Int.*, 191(3):1135–1151.
- Reading, A. M., Cracknell, M. J., Sambridge, M., and Foster, J. G. (2011). Turning geophysical data into geological information or why a broader range of mathematical strategies is needed to better enable discovery. *Preview*, 151:24–29.
- Robertson, K. E., Taylor, D. H., Thiel, S., and Heinson, G. S. (2014). Magnetotelluric evidence for serpentinisation in a Cambrian subduction zone beneath the Delamerian Orogen, southeast Australia. *Gondwana Research*, 28(2):601–611.
- Rosas-Carballo, M., Linde, N., Kalscheuer, T., and Vrugt, J. A. (2014). Two-dimensional probabilistic inversion of plane-wave electromagnetic data: methodology, model constraints and joint inversion with electrical resistivity data. *Geophys. J. Int.*, 196(3):1508–1524.
- Rothman, D. H. (1985). Nonlinear inversion, statistical mechanics, and residual statics estimation. *Geophysics*, 50(12):2784–2796.
- Rothman, D. H. (1986). Automatic estimation of large residual statics corrections. *Geophysics*, 51(2):332–346.

- Rowbotham, P. S. and Pratt, R. G. (1997). Improved inversion through use of the null space. *Geophys. Prospect.*, 62(3):869–883.
- Rudin, L. I., Osher, S., and Fatemi, E. (1992). Nonlinear total variation based noise removal algorithms. *Physica D*, 60(1–4):259–268.
- Sacchi, M. D. (1998). A bootstrap procedure for high-resolution velocity analysis. *Geophysics*, 63(5):1716–1725.
- Salmon, M., Kennett, B. L. N., Stern, T., and Aitken, A. R. A. (2013). The Moho in Australia and New Zealand. *Tectonophysics*, 609:288–298.
- Sambridge, M. (1999a). Geophysical inversion with a neighbourhood algorithm – I. Searching a parameter space. *Geophys. J. Int.*, 138(2):479–494.
- Sambridge, M. (1999b). Geophysical inversion with a neighbourhood algorithm – II. Appraising the ensemble. *Geophys. J. Int.*, 138(3):727–746.
- Sambridge, M. and Drijkoningen, G. (1992). Genetic algorithms in seismic waveform inversion. *Geophys. J. Int.*, 109:323–342.
- Sandvol, E. and Hearn, T. (1994). Bootstrapping shear-wave splitting errors. *Bull. seism. Soc. Am.*, 84(6):1971–1977.
- Santos Ltd (1994). Moomba 73: Well completion report. Technical Report 7464/6.
- Schmidt, S. R. (2012). *Extraordinary Memories for Exceptional Events. Essays in Cognitive Psychology*. Taylor & Francis.
- Sen, M. K. and Stoffa, P. L. (2013). *Global Optimization Methods in Geophysical Inversion*. Cambridge Univ. Press, Amsterdam, 2 edition.
- Sen, P. K. (1968). Estimates of the regression coefficient based on Kendall's tau. *JASA*, 63(324):1379–1389.
- Shaar, R., Ron, N., Tauxe, L., Kessel, R., and Agnon, A. (2011). Paleomagnetic field intensity derived from non-SD: Testing the Thellier IZZI technique on MD slag and a new bootstrap procedure. *Earth Planet. Sci. Lett.*, 310(3–4):213–224.

BIBLIOGRAPHY

- Shearer, P. M. (1997). Improving local earthquake locations using the L1 norm and waveform cross correlation: application to the Whittier Narrows, California, aftershock sequence. *J. geophys. Res.*, 102(B4):8269–8283.
- Shepard, R. N. (1967). Recognition memory for words, sentences, and pictures. *Journal of Verbal Learning and Verbal Behavior*, 6(1):156–163.
- Simpson, F. and Bahr, K. (2005). *Practical Magnetotellurics*. Cambridge Univ. Press.
- Siripunvaraporn, W. (2012). Three-dimensional magnetotelluric inversion: An introductory guide for developers and users. *Surv. Geophys.*, 33(1):5–27.
- Siripunvaraporn, W. and Egbert, G. (2007). Data space conjugate gradient inversion for 2-D magnetotelluric data. 170(3):986–994.
- Siripunvaraporn, W. and Egbert, G. (2009). WSINV3DMT: Vertical magnetic field transfer function inversion and parallel implementation. *Phys. Earth Planet. Inter.*, 173(3-4):317 – 329.
- Smith, J. (1971). The dynamics of shale compaction and evolution of pore-fluid pressures. *Math. Geol.*, 3(3):239–263.
- Smith, T. and Booker, J. (1991). Rapid inversion of two- and three-dimensional magnetotelluric data. *J. Geophys. Res.*, 96(B6):3905–3922.
- Stockill, J. (2008). Geophysical survey logistics report: Regarding the Quantec Spartan tensor magnetotelluric survey over the Cooper MT project, South Australia, Australia, on behalf of Eden Energy Ltd, Adelaide, SA, Australia. Logistics Report AU00039L, Quantec Geoscience Pty Ltd.
- Stoffa, P. L. and Sen, M. K. (1991). Nonlinear multiparameter optimization using genetic algorithms: Inversion of plane-wave seismograms. *Geophysics*, 56(11):1794–1810.
- Storn, R. and Price, K. (1997). Differential evolution - a simple and efficient heuristic for global optimization over continuous spaces. *Geophys. J. Int.*, 11(4):341–359.

- Sun, X. (1997). Structural style of the Warburton Basin and control in the Cooper and Eromanga Basins, South Australia. *Explor. Geophys.*, 28(3):333–339.
- Syswerda, G. (1989). Uniform crossover in genetic algorithms. In Schaffer, D. J., editor, *Proc. of the Third International Conference on Genetic Algorithms*, pages 2–9.
- Tang, Y., Reed, P., and Wagener, T. (2006). How effective and efficient are multiobjective evolutionary algorithms at hydrologic model calibration? *Hydrology and Earth System Sciences*, 10(2):289–307.
- Tarantola, A. (2005). *Inverse Problem Theory and Methods for Model Parameter Estimation*. SIAM.
- Tarits, P., Jouanne, V., Menvielle, M., and Roussignol, M. (1994). Bayesian statistics of non-linear inverse problems: example of the magnetotelluric 1-D inverse problem. *Geophys. J. Int.*, 119(2):353–368.
- Tauxe, L., Gee, J. S., and Staudigel, H. (1998). Flow directions in dikes from anisotropy of magnetic susceptibility data: The bootstrap way. *J. geophys. Res.*, 103:17775–17790.
- Tauxe, L., Kylstra, N., and Constable, C. (1991). Bootstrap statistics for paleomagnetic data. *J. geophys. Res.*, 96(B2):11723–11740.
- Telford, W. M., Geldart, L. P., and Sheriff, R. E. (1990). *Applied Geophysics*. Monograph series. Cambridge Univ. Press.
- Theil, H. (1950). A rank-invariant method of linear and polynomial regression analysis. I. *Nederl. Akad. Wetensch., Proc.*, 53:386–392 = Indagationes Math. 12, 85–91 (1950).
- Thiel, S. and Heinson, G. (2010). Crustal imaging of a mobile belt using magnetotellurics: An example of the Fowler Domain in South Australia. *J. geophys. Res.*, 115(B6):B06102.
- Thorburn, W. M. (1918). The myth of Occam’s razor. *Mind*, 27(107):345–353.

BIBLIOGRAPHY

- Tichelaar, B. W. and Ruff, L. J. (1989). How good are our best models? Jackknifing, bootstrapping, and earthquake depth. *Eos Trans. AGU*, 70(20):593–606.
- Tikhonov, A. N. and Arsenin, V. Y. (1977). *Solutions of Ill-posed Problems*. John Wiley and Sons.
- Treitel, S. and Lines, L. R. (1999). Past, present and future of geophysical inversion - a Y2K analysis. Crewes research report, Indian Institute of Technology.
- Tsutsui, S., Yamamura, M., and Higuchi, T. (1999). Multi-parent recombination with simplex crossover in real coded genetic algorithms. In *Proc. of the Genetic and Evolutionary Computation Conference (GECCO 1999)*, pages 657–664.
- Vozoff, K. and Jupp, D. L. B. (1975). Joint inversion of geophysical data. *Geophys. J. R. astr. Soc.*, 42(3):977 – 991.
- Vrugt, J. A. and Robinson, B. A. (2007). Improved evolutionary optimization from genetically adaptive multimethod search. *Proc. Nat. Acad. Sci. U.S.A.*, 104(3):708–711.
- Vrugt, J. A., Robinson, B. A., and Hyman, J. M. (2009). Self-adaptive multimethod search for global optimization in real-parameter spaces. *Evolutionary Computation, IEEE Trans. on*, 13(2):243–259.
- Wait, J. R. (1954). On the relation between telluric currents and the Earth’s magnetic field. *Geophysics*, 19(2):281–289.
- Wang, J. and Tan, Y. (2005). 2-D MT inversion using genetic algorithm. *J. Phys. Conf. Ser.*, 12(1):165–170.
- Wannamaker, P. E., Stodt, J. A., and Rijo, L. (1987). A stable finite-element solution for two-dimensional magnetotelluric modeling. *Geophys. J. R. astr. Soc.*, 88(1):277–296.
- Weidelt, P. (1972). The inverse problem of geomagnetic induction. *J. Geophys. (Z. Geophysik)*, 38:257–289.

- Whitehouse, A. J. O., Maybery, M. T., and Durkin, K. (2006). The development of the picture-superiority effect. *British Journal of Developmental Psychology*, 24(4):767–773.
- Wiggins, R. A. (1969). Monte Carlo inversion of body-wave observations. *J. geophys. Res.*, 74(12):3171–3181.
- Yang, C.-H. and Tong, L.-T. (1988). Joint inversion of DC, TEM, and MT data. In *58th Annual International Meeting*, pages 408–410. National Central University, Taiwan, Society of Exploration Geophysicists.
- Zhdanov, M. and Hursan, G. (2000). 3D electromagnetic inversion based on quasi-analytical approximation. *Inverse Prob.*, 16(5):1297–1322.
- Zhdanov, M. S. (2015). *Inverse Theory and Applications in Geophysics*. Methods in Geochemistry and Geophysics. Elsevier Science.
- Zhou, A., Qu, B.-Y., Li, H., Zhao, S.-Z., Suganthan, P. N., and Zhang, Q. (2011). Multiobjective evolutionary algorithms: A survey of the state of the art. *Swarm and Evolutionary Computation*, 1(1):32–49.
- Zitzler, E. (1999). *Evolutionary Algorithms for Multiobjective Optimization: Methods and Applications*. PhD thesis, ETH Zurich, Switzerland.
- Zitzler, E., Deb, K., and Thiele, L. (2000). Comparison of multiobjective evolutionary algorithms: Empirical results. *Evolutionary Computation*, 8(2):173–195.